

AD A127477

AFOSR-TR- 83-0275

(4)

DTIC FILE COPY

DTIC
APR 29 1983
HA

Approved for public release
distribution unlimited.

83 04 28 054

ARPA Order 3291-32
Program Code OD80
Name of Contractor: University of Colorado
Effective Date of Contract: 1 October 1980
Contract Expiration Date: 30 September 1982
Amount of Contract: \$323,000
Contract Number: F49620-80-C-0018
Principal Investigator: C. B. Archambeau (303)-492-8028
Program Manager: William J. Best (202)-767-5011
Title of Work: Deterministic Methods of Seismic Source Identification

Annual Technical Report No. 4

October 1, 1981-September 30, 1982

Sponsored by
Advanced Research Projects Agency (DOD)
ARPA Order No. 3291-32
Monitored by AFOSR Under Contract No. F49620-80-C-0018

The views and conclusions contained in this document are those of the authors and should not be interpreted as necessarily representing the official policies, either expressed or implied, of the Defense Advanced Research Projects Agency or the U.S. Government.

DTIC

APR 29 1983

H

AIR FORCE OFFICE OF SCIENTIFIC RESEARCH (AFSC)
NOTICE OF REVISION TO DTIC
This technical report has been reviewed and is approved for release under AFR 190-12.
Distribution is unlimited.
MATTHEW J. KEEPER
Chief, Technical Information Division

UNCLASSIFIED

SECURITY CLASSIFICATION OF THIS PAGE (When Data Entered)

REPORT DOCUMENTATION PAGE		READ INSTRUCTIONS BEFORE COMPLETING FORM
1. REPORT NUMBER AFOSR-TR- 83 - 0275	2. GOVT ACCESSION NO. <i>AD A12 7477</i>	3. RECIPIENT'S CATALOG NUMBER
4. TITLE (and Subtitle) Deterministic Methods of Seismic Source Identification		5. TYPE OF REPORT & PERIOD COVERED <i>Final</i> 9/30/81 to 10/1/82
7. AUTHOR(s) Charles B. Archambeau		6. PERFORMING ORG. REPORT NUMBER
9. PERFORMING ORGANIZATION NAME AND ADDRESS CIRES University of Colorado Boulder, CO 80309		8. CONTRACT OR GRANT NUMBER(s) F49620-80-C-0018,
11. CONTROLLING OFFICE NAME AND ADDRESS Defense Advanced Research Projects Agency 1400 Wilson Blvd. Arlington, VA 22209		10. PROGRAM ELEMENT, PROJECT, TASK AREA & WORK UNIT NUMBERS <i>61247E 2309/A1</i>
14. MONITORING AGENCY NAME & ADDRESS (if different from Controlling Office) Air Force Office of Scientific Research Bolling Air Force Base Washington, D. C. 20332		12. REPORT DATE February 1983
		13. NUMBER OF PAGES <i>181</i>
		15. SECURITY CLASS. (of this report) unclassified
		15a. DECLASSIFICATION/DOWNGRADING SCHEDULE
16. DISTRIBUTION STATEMENT (of this Report) Approved for public release; distribution unlimited.		
17. DISTRIBUTION STATEMENT (of the abstract entered in Block 20, if different from Report)		
18. SUPPLEMENTARY NOTES		
19. KEY WORDS (Continue on reverse side if necessary and identify by block number) Discrimination, Anelasticity, signal analysis, elastodynamics, wave propagation, explosion yield estimation		
20. ABSTRACT (Continue on reverse side if necessary and identify by block number) See attached		

DD FORM 1473

EDITION OF 1 NOV 65 IS OBSOLETE

UNCLASSIFIED

SECURITY CLASSIFICATION OF THIS PAGE (When Data Entered)

UNCLASSIFIED

This report emphasizes results from completed research in seismic wave attenuation. We also describe and illustrate current signal analysis methods using a variety of seismic time series data.

The results reported include relative amplitudes, at a large number of standardized seismic stations in the U.S. and Southern Canada, for a large number of explosions and earthquakes observed at three fixed azimuths for many stations. The average Q_a at 1 Hz, for the upper 300 km of the crust-mantle beneath the study area varies from about 65 at Golden, Colorado to about 2000 at Red Lake, Ontario. The mean Q_a is 140 for the continental U. S. These absolute Q_a values are obtained from the relative amplitude data by requiring that the largest positive amplitude anomalies for the U.S./Canada correspond to an upper mantle Q_a with a value greater than 1000. The Q_a values obtained correspond to t_a^* values ranging from .02 up to .5, with $t_a^* = .3$ the mean value for the continental U. S. The results are sufficiently dense spatially to allow a contour map for Q_a to be constructed which incorporates the azimuthal variations observed at many of the stations. This representation shows general correlation of low Q_a with high heat flow and low P_n velocity for example, although on a fine spatial scale there appears to be numerous exceptions which may be related to unaccounted for focusing and scattering effects rather than anelastic effects.

Other work completed has provided new, high resolution, Q determinations from low order free oscillation excitation, and these results provide strong constraints on lower mantle attenuation.)

We describe new signal analysis methods devised for use in automatic discrimination and yield estimation in a multivariant approach. In this context we have the current ability to rapidly and automatically obtain spectral magnitudes for a large number of seismic phases, which can be used in both teleseismic and regional discrimination and for yield estimation.

Accession For	
NTIS GRA&I	<input checked="checked" type="checkbox"/>
DTIC TAB	<input type="checkbox"/>
Unannounced	<input type="checkbox"/>
Justification	
By	
Distribution/	
Availability Codes	
Dist	Avail and/or Special
A	



UNCLASSIFIED

Table of Contents

	Page
Summary	
I. Introduction	4
II. Attenuation of Seismic P Waves and Amplitude Variations in the Continental U. S.	6
III. Anelasticity of the Lower Mantle and Source Excitation Inferred from Low Frequency Free Oscillations	83
IV. Signal Detection and Analysis Using Quasi-Harmonic Decomposition (QHD) Methods	111
Appendix - P wave Amplitude Variations at WWSSN Stations in the U. S. and Canada	

**Research on Deterministic Methods of
Seismic Source Identification**

Report No. 4 - Summary

The objectives of this research program are to: (1) Develop and perfect methods of synthesis of theoretical seismic radiation fields at regional and teleseismic distance ranges in order to provide a basis for developing, testing and understanding seismic source discrimination methods; (2) Develop formal inversion procedures to be used to obtain quantitative estimates of physical parameters of seismic sources and the medium and to use these estimates to determine underground explosion yield, and as a basis for source identification and discrimination; (3) Develop the means and methods to analyze seismic data for source identification and propagational medium characteristics for event discrimination and yield estimation purposes; and finally to (4) Develop, test and evaluate microprocessor systems, incorporating software and hardware components designed to provide advanced interactive seismic time series analysis for RST (Remote Seismic Terminal) applications.

In the first year annual report of this two year contract, we described research results in the areas of discrimination using inferred physical parameters of seismic sources; the synthesis of complete seismic wave fields in the near and regional distance ranges from the seismic source and the utilization of this capability in source and path of propagation studies; basic theoretical developments in seismic source representations and wave propagation studies and the implementation and application of advanced signal processing methods.

In the present report we emphasize results relating to completed research in seismic wave attenuation studies. We also describe and illustrate current signal analysis methods using a variety of seismic time series.

Our attention to studies of seismic attenuation is motivated by the strong spatial variability of observed body wave amplitudes and the corresponding variability and uncertainties when seismic body wave data is used. Thus in investigating and quantifying the magnitude and spatial dependence of the adsorption of seismic energy in the earth, we expect to be able to infer the mechanisms responsible for the energy losses and their relationships to other geophysical variables, such as heat flow, seismic velocities, seismicity and tectonic/geologic setting, and thereby be able to infer attenuation properties of particular regions on the earth based on other, more easily measured and/or currently known seismic/geophysical variables. More directly, however, we wish to quantify the magnitude and variability of attenuation losses in the context of explosive yield estimation and also for discrimination, particularly for applications of spectral discriminants.

The results reported here describe the analysis of body wave amplitude data, from a large number of explosions and earthquakes, observed at WWSSN, LRSM and other standardized seismic stations throughout the continental U. S. and Southern Canada. The average Q_a (dissipation function for P waves) in the upper 300 km of the mantle beneath the U.S. is 140 at 1 Hz. This mean value is obtained from the relative amplitude values at the stations in the U.S. and So. Canada, under the condition that the largest relative amplitudes observed (at the station at Red lake Ontario) correspond to an upper mantle Q_a of about 2000. In this case the variation in the upper mantle Q_a ranges from above 1000 to about 65, the latter at Golden, Colorado and the former at Red Lake Ontario. These values of Q_a correspond to an average $t_a^* = .3$, for one way transit of a P wave through the upper mantle, and variations from approximately $t_a^* = .5$ to $t_a^* = .02$. The station sampled variations of the mean upper mantle and crust Q_a throughout the U. S. are used to construct a contour map which shows the

variation of the mean Q_a in the U.S., and its correlation with geophysical provinces and independent geophysical observations, such as heat flow, gravity and P_n velocities. There is broad correlation of low Q_a with high seismicity and high heat flow and with low P_n velocity and gravity, although on a fine spatial scale there appear to be numerous exceptions. (i.e. local anomalous Q_a values, of small dimension, not correlating with *known* average values of seismicity, heat flow, etc. These may be due to focusing and/or scattering effects in the upper mantle or crust, rather than anelastic effects.)

In other reported work on anelasticity and associated seismic wave attenuation we have used the free oscillations of the earth to investigate the Q for the lower mantle. In this work we show that the Q for ${}_0S_2$ and ${}_0S_3$ are 399 and 358, respectively. The accurate Q estimates for low order free oscillations provide us with the means of determining the proper attenuation corrections for P wave propagation in the lower mantle, to be used to obtain accurate yield estimates from teleseismic data. While the lower mantle absorption is relatively small, the knowledge of the lower mantle Q allows us to more accurately assess the large and variable upper mantle effects.

We describe new signal analysis methods devised for use in automatic discrimination and yield estimation in a multivariant approach. In this context, we have the current ability to rapidly and 'automatically' obtain spectral magnitudes for a large number of seismic phases, which can be used in both teleseismic and regional discrimination, such as frequency dependent body and surface wave magnitudes. We expect to implement some of these methods at the Center for Seismic Studies and on a remote seismic terminal (RST system) for extensive and systematic testing in the near future.

I. Introduction

The objectives of the research being conducted under the current 2 year contract are to: (1) Develop and apply methods of seismogram synthesis using mode superposition and similar methods as aids in discrimination/yield estimation studies; (2) Develop and apply source inversion methods, to infer physical properties of seismic sources for discrimination purposes; (3) Develop regional discrimination techniques based on the physical properties of seismic sources; (4) Develop/apply methods of determining anelastic, frequency dependent, absorption characteristics of the medium; (5) Pursue studies designed to provide a physical basis for seismic discriminants; (6) Apply and evaluate automated methods of signal analysis for event detection and discrimination in the regional and teleseismic distance ranges; (7) Pursue studies of wave propagation along oceanic paths with the objectives of understanding the propagation out to large distances and developing discrimination and yield estimation methods utilizing the broad band nature of the signals observed; and (8) Implement advanced time series analysis software on, both, large main-frame and the RST (Regional Seismic Terminal) microprocessor. Test and evaluate the main frame operation and the RST system, and recommend final hardware/software systems for general and specialized use.

In the previous annual report, for the period October 1, 1981 to September 30, 1982, we summarized results relating to: (1) the use of inferred physical parameters of seismic sources (stress changes and rupture zone dimensions) as a means of event discrimination; (2) modal synthesis of the complete seismic wave field in the near and regional distance ranges for source and path studies; (3) theoretical developments in seismic source representations and wave propagation studies; (4) applications of advanced signal processing methods to high frequency near field data for inferences of source properties; and (5) imple-

mentation of signal processing/analysis software on an RST microprocessor and on a CRAY-1 main frame computer.

In the present report we emphasize research results relating to completed research in seismic wave attenuation studies (Sections II and III). We also include a summary of the signal processing capability that has been developed, along with examples of its application in Section IV.

The importance of the attenuation studies relates to the strong dependence of yield estimates on the attenuation characteristics of the upper mantle and crust, particularly at the source and receiver sites. In addition, spectral discriminants, such as the VFM (Variable Frequency Magnitude or $m_b(f)$) discriminant, are strongly influenced by local variations in attenuation. For applications of this discriminant then, it is important to be able to isolate the zones of high attenuation in terms of the magnitude of the attenuation, the lateral extent of such zones and, as importantly, the depth distribution of the high attenuation zones (upper mantle versus crust in particular). Specifically, if high attenuation zones are confined to the upper mantle, world-wide, then regional discrimination using VFM methods should be extremely effective when (only) crustal phases are used. Finally, the frequency dependence of the attenuating mechanism, as well as its depth distribution, is of considerable importance for both yield estimation and discrimination since high frequency spectral magnitudes may be much less affected by attenuation processes in the earth and therefore more reliable for both yield estimation and discrimination.

The emphasis placed on the advanced signal analysis methods is based on the requirement that fast and systematic methods of considerable sophistication are needed to implement yield estimation as well as discrimination procedures in practice. Our results in this area are particularly encouraging and we hope to implement the methods developed on the new RST system, as well as

at the Center for Seismic Studies, in the near future.

II. Attenuation of Seismic P waves and Amplitude Variations in the Continental U. S.

This study (Butler, 1983), is largely concerned with amplitude effects that may be ascribed to the locale of the seismic station. Naturally to obtain this end, a great deal of care must be taken to minimize amplitude effects which are attributable to the seismic source or the propagation path. The source term for each event used should be nearly the same at all stations of the network - this constraint is relatively easy for explosions, but can be quite difficult for earthquakes. A consistent amplitude measure from the P waveform must be made at all stations, and it is favorable to have one seismologist make all the measurements. The distance range between sources and receivers should be such that the seismic waves bottom in the relative smooth lower mantle of the earth, avoiding upper mantle triplications and core-mantle boundary diffraction. This corresponds to a distance range of 30° to 95° , $\Delta \sim 3300$ to 10500 km. For S waves, interference with SKS and ScS beyond 85° must be avoided. The amplitude data are corrected for the seismometer gain and corrected for geometric spreading to a reference distance - the mean distance of the data set is reasonable. The amplitude data should be processed separately for different azimuths, as azimuthally dependent station amplitudes have been observed for WWSSN stations in the United States (Butler and Ruff, 1980) and at the large seismic arrays LASA (Chang and von Seggern, 1980) and NORSAR (Berteussen, 1975).

A map of the United States in Figure 1 shows the location of WWSSN stations in relation to physiographic provinces. Table 1 lists the names and locations of the WWSSN stations. The locations of three digital SDCS (Special Data Collection System) stations are also noted - RKON, Red Lake, Ontario, HNME, Houlton, Maine; and OB2NV, Oak Springs Butte, Nevada. These digital SDCS

Table 1
Seismic Stations

Station Code	Name and Location
AAM	Ann Arbor, Michigan
ALQ	Albuquerque, New Mexico
ATL	Atlanta, Georgia
BEC	Bermuda
BKS	Berkeley, California
BLA	Blacksburg, Virginia
BOZ	Bozemann, Montana
COR	Corvallis, Oregon
DAL	Dallas, Texas
DUG	Dugway, Utah
FLO	Florissant, Missouri
GEO	Georgetown, Washington, D. C.
GOL	Golden, Colorado
GSC	Goldstone, California
HNME	Houlton, Maine
JCT	Junction City, Texas
LON	Longmire, Washington
LUB	Lubbock, Texas
MDS	Madison, Wisconsin
MSO	Missoula, Montana
OB2NV	Oak Springs Butte, Nevada
OGD	Ogdensburg, New Jersey
OXF	Oxford, Mississippi
RCD	Rapid City, South Dakota
RKON	Red Lake, Ontario
SCP	State College, Pennsylvania
SHA	Spring Hill, Alabama
TUC	Tucson, Arizona
WES	Weston, Massachusetts

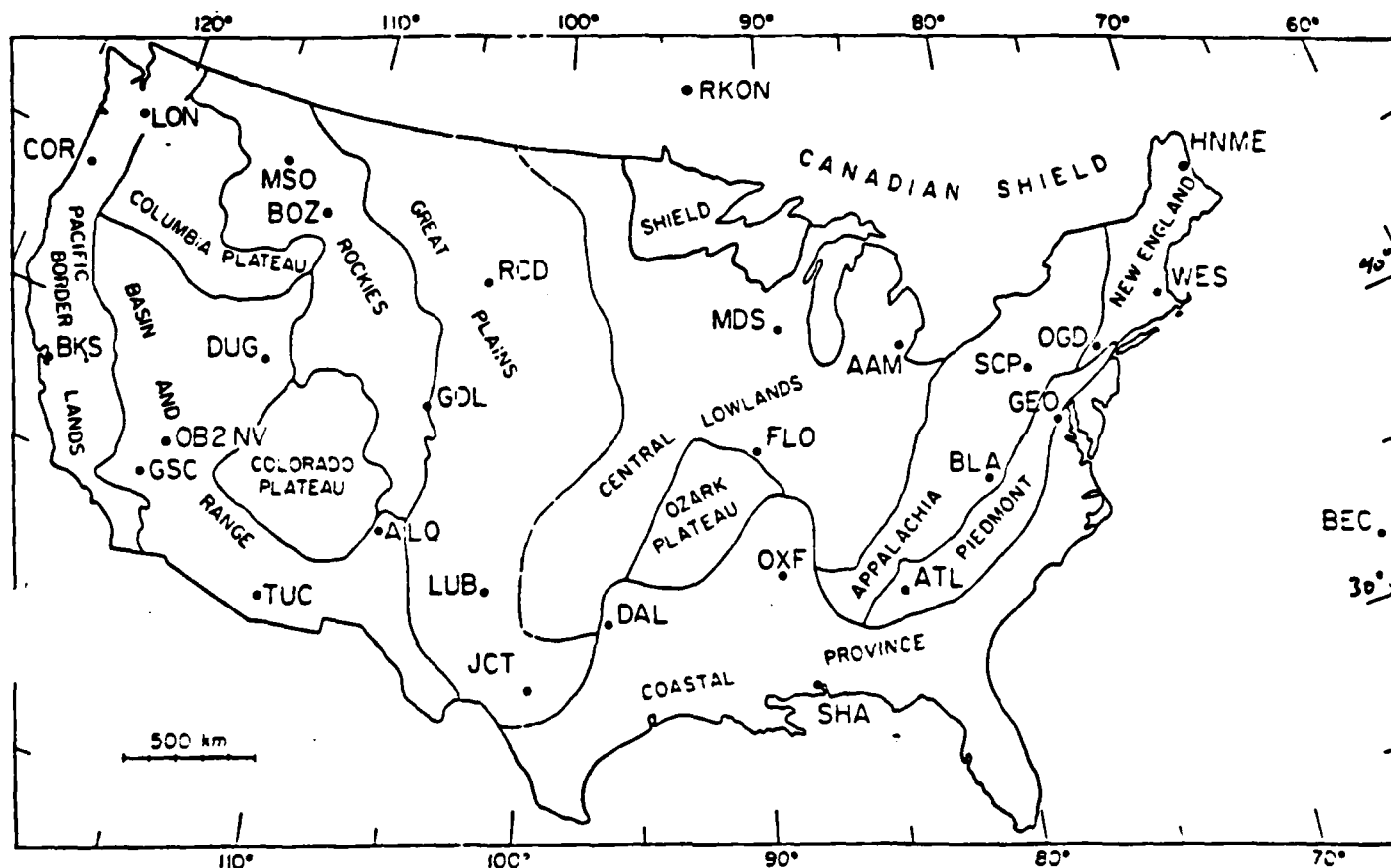


Figure 1. A map of approximate physiographic provinces of the United States and southern Canada is shown with seismometer locations noted with station code names.

stations are filtered to match the WWSSN short period instrument response and may be used to tie LRSM studies to the WWSSN. The WWSSN stations consist of six seismometers - a vertical and two horizontal instruments with matched responses, recording short period (1 sec) and long period (20 sec) ground motion. The SDCS sites are also equipped with three component short period and long period seismometers. In this study all amplitudes are measured from the short period vertical instrument. Most of these stations are located on hard rock sites. Stations located on sediments on the west coast and in the central United States - BKS, RCD, LUB, JCT, DAL, OXF, SHA, AAM, FLO - are reviewed in a following section for signal amplification effects due to the sediments.

The amplitude measure used in this study is the peak to peak amplitude of the first cycle of P wave motion. This measure was found to be more stable in the presence of seismic noise than a peak amplitude measurement of the P wave first motion. *Crustal reverberations, near source surface reflections, and P to S conversions near the receiver may contaminate the amplitude through constructive or destructive interference, but the first cycle of P motion is most free of these difficulties.*

Earthquake and underground nuclear explosion sources are used in this amplitude study. Underground nuclear explosions have nearly the same waveform at all stations with an impulsive, distinct shape allowing an unambiguous measurement of amplitude. The earthquake data is not so simple and considerable care was used in event selection for this study.

Specifically, amplitude data from earthquake sources was selected by the set of criteria of Butler (1979a,b), Butler and Ruff (1980), and Lay and Helmburger (1981). The following procedure is used: Earthquakes in South America and the Asian-Pacific-Aleutian arc were viewed on seismograms from three widely spaced stations in the United States. Events whose waveforms passed the set of criteria at the three stations were examined at all stations. Out of the set of events which fulfilled the selection criteria at all stations, a quality subset of events were measured for amplitude. Even under these stringent selection procedures, some P waveform vagaries remained in the data set. In some instances, one station would have a slightly different frequency content than other stations. In other instances the waveform at a station might have an additional inflection, or the relationship between peak amplitudes might be slightly different, or the signal to noise ratio at a station would be borderline. These vagaries were handled in the following manner. An amplitude was measured, but a note of the questionable behavior was made. After all events had been measured, reduced, processed, and preliminary station amplitude effects determined, then the amplitude data were reviewed. Amplitudes which were greater than two standard errors away from the mean were checked to see if a note of questionable behavior had been made. If a note had been made, the amplitude measure was deleted from the data set. If a no questionable behavior had been noted, the amplitude measure was retained in the data set. Following this method, four P wave amplitude measurements from waveforms with questionable behavior were deleted.

Three azimuths of approach were examined in determining the station amplitude effects for the WWSSN stations in the United States. For a northern azimuth, nuclear explosion sources in the U.S.S.R. were analyzed. Most of these data were discussed in Butler and Ruff (1980). The explosion data set were distributed among five test sites: northern and southern Novaya Zemlya, eastern and western Semipalatinsk, and western Kazakh. Three additional explosions in the eastern Semipalatinsk site in the period 1976-1977 were measured at the WWSSN stations and at the three SDCS Stations, RKON, HNME, and OB2NV to tie the SDCS stations to the WWSSN network. A pattern of relative amplitudes in the United States was determined for each test site, and the results from the five test sites were averaged to yield a relative amplitude pattern for a northern azimuth from the United States. The apparent period of the first cycle of P wave motion for the explosion sources measured on the WWSSN short period instrument was usually about 1 second, with little variation from one event to another (a range of 1.2 to 0.8 sec). A special exception was the SDCS station - filtered to have a WWSSN response - RKON, which had an apparent period of 0.5 seconds for the first cycle of P wave motion from three Semipalatinsk explosions. This anomalous observation will be discussed later. Aside from the strange behavior of RKON, the amplitude data from explosions is quite stable, and for a single test site the relative amplitude pattern shows little variation from event to event (Butler and Ruff, 1980). Amplitude pattern variation between the test sites indicating near source heterogeneity is discussed in Butler and Ruff (1980). Core-mantle boundary diffraction effects at distances greater than $95.5^\circ\Delta$ are discussed in Ruff and Helmberger (1981). Amplitude data which suffered diffraction at the core-mantle boundary were excluded in

this present study of receiver amplitude effects.

The location and origin times of the 36 nuclear explosions analyzed are listed in Table 2 and grouped by their respective test sites. The amplitude data measured from the first cycle of P wave motion are listed in the Appendix in Tables A1-A6. The data have been corrected for seismometer gain and are expressed in nanometers of ground displacement. No geometric spreading corrections were made as the effect is $\pm 10\%$ for this geometry of sources and receivers. However, in transforming the amplitude variations into apparent variations of the dissipation parameter Q or attenuation, geometric spreading corrections are included.

While the relative amplitude for a northern azimuth from the United States comes exclusively from explosions, the relative amplitude patterns of the WWSSN stations in the United States for both a northwest azimuth and a south-southeast azimuth come exclusively from earthquakes. Events at a northwest azimuth include earthquakes in the Bonin Islands, Japan, Kurile Islands, and the Aleutians. Events at a south-southeast azimuth are comprised by earthquakes in South America where most of the events lie along the north and central Chile-Argentina border. Amplitude data from some of these events were presented in a preliminary form by Butler and Ruff (1980), who were largely concerned with establishing to what extent were azimuthal variations of station amplitude effects important. Finding that azimuthal variation is relatively important, this present study follows to consider these effects in more detail. The earthquakes were not sufficiently localized to be divided into subgroups in the fashion that the explosions were divided among test sites. However, though the earthquakes were subdivided among broad source regions to look for systematic source region effects such as focusing/defocusing by subduction zone structure, in the final analysis the amplitude data from the earthquakes are

Table 2
Explosion Data Set*

Northern Novaya Zemlya

27 Oct 66	5:57:58	73.44N	54.75E
21 Oct 67	4:59:58	73.37N	54.81E
7 Nov 68	10:02:05	73.40N	54.86E
14 Oct 69	7:00:08	73.40N	54.81E
14 Oct 70	6:02:57	73.31N	55.15E
27 Sept 71	5:59:55	73.39N	55.10E
28 Aug 72	5:59:57	73.34N	55.09E
12 Sept 73	6:59:54	73.30N	55.16E
29 Aug 74	9:59:56	73.37N	55.09E
23 Aug 75	8:59:58	73.37N	54.64E
21 Oct 75	11:59:57	73.35N	55.09E

Southern Novaya Zemlya

27 Oct 73	6:59:58	70.76N	53.97E
2 Nov 74	4:59:57	70.82N	54.06E
18 Oct 75	8:59:56	70.84N	53.69E

Semipalatinsk East

15 Jan 65	5:59:59	49.89N	78.97E
30 Nov 69	3:32:57	49.92N	79.00E
2 Nov 72	1:26:58	49.91N	78.84E
23 Jul 73	1:22:58	49.99N	78.85E
14 Dec 73	7:46:57	50.04N	79.01E
31 May 74	3:26:57	49.95N	78.84E
4 Jul 76	2:56:58	49.91N	78.95E

Semipalatinsk East-Additional Data

23 Nov 76	5:03:00	50.00N	79.00E
7 Dec 76	4:57:00	49.90N	78.90E
29 May 77	2:59:00	49.90N	78.90E

Table 2
Explosion Data Set*

Semipalatinsk West

19 Oct 66	3:57:58	49.75N	78.03E
20 Apr 67	4:07:58	49.74N	78.12E
17 Oct 67	5:03:58	49.82N	78.10E
29 Sept 68	3:42:58	49.77N	78.19E
28 Jun 70	1:57:58	49.83N	78.25E
22 Mar 71	4:32:58	49.74N	78.18E
25 Apr 71	3:32:58	49.82N	78.09E
30 Dec 71	6:20:58	49.75N	78.13E
20 Feb 75	5:32:58	49.82N	72.08E

Kazakh

6 Dec 69	7:02:57	43.83N	54.78E
12 Dec 70	7:00:57	43.85N	54.77E
23 Dec 70	7:00:57	43.83N	54.85E

*Locations and origin times (1966-1976) from Dahlman and Israelson (1977).
after July, 1976 from Seismic Data Analysis Center

APRIL 25, 1967 SOUTH AMERICAN EARTHQUAKE

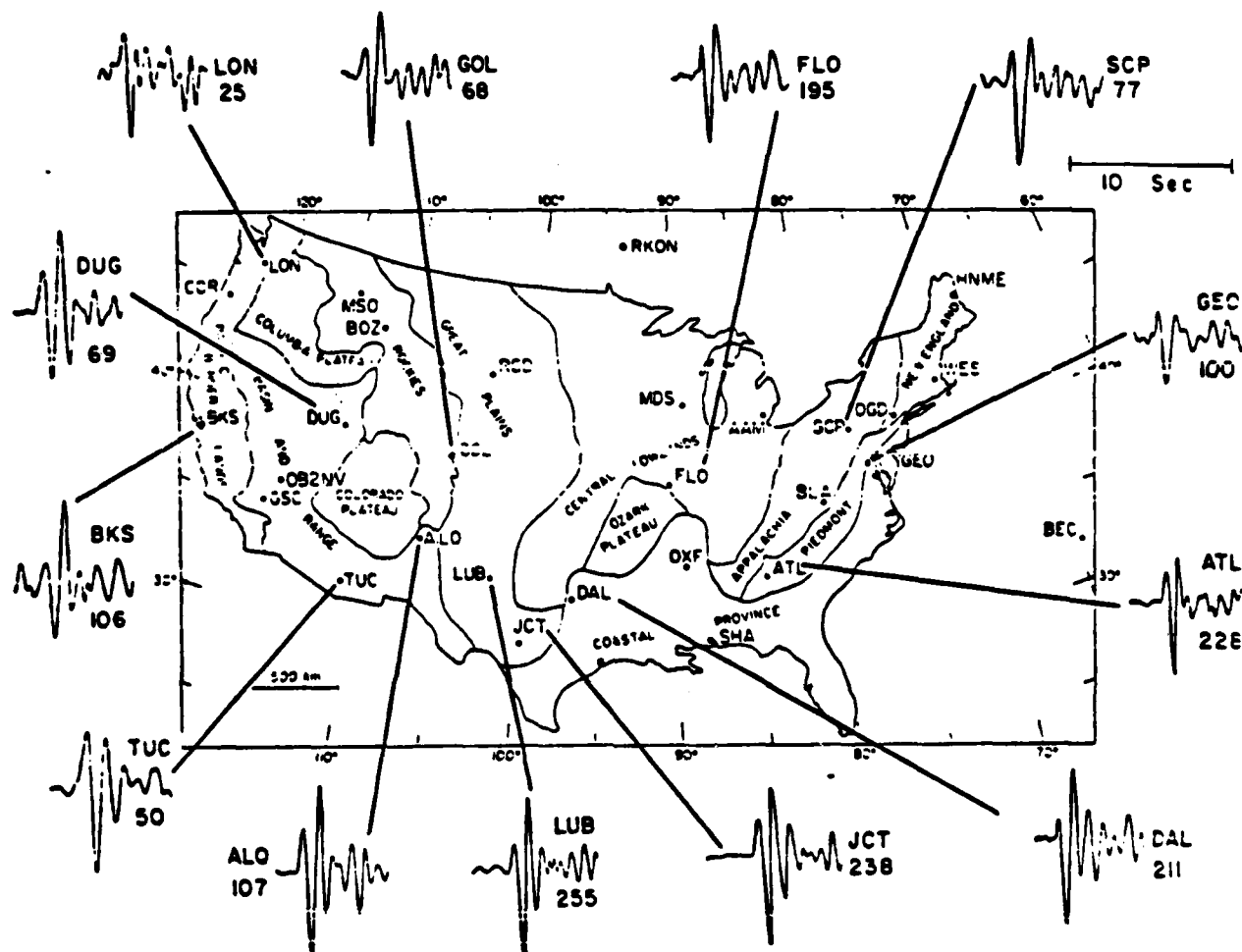


Figure 2. P waves recorded on short period vertical seismometers of WSSN stations in the United States are shown for an earthquake in South America on April 25, 1967. The amplitude of the first cycle of P wave motion is given in nanometers, corrected for geometric spreading to a distance $\Delta = 60^\circ$.

Table 3
Earthquakes in a Northwest Azimuth

Date	Origin Time	Location*	Depth (km)	
Kurile Islands Earthquakes				
11/22/66	6:29:52.4	49.0 N 146.8E	441	
3/20/67	12:31:34.0	45.6N 151.4E	51	
8/10/67	11:21:22.3	45.4N 150.3E	37	
2/10/68	10:00:05.8	46.0N 152.3E	87	
4/28/68	4:18:15.7	44.8N 174.5E	39	
7/25/68	10:50:31.5	45.7N 146.7E	16	
10/26/76	5:58:56	46.1N 159.7W	130	
3/19/77	10:56:08	43.0N 149.0E	0	
Japanese Earthquakes				
12/31/76	9:16:37	40.0N 145.0E	0	
1/1/77	11:33:42	30.6N 137.2E	483	
2/18/77	20:51:26	34.0N 143.0E	0	
6/12/77	8:48:05	43.0N 142.3E	241	
Bonin Islands Earthquakes				
9/22/76	8:20:28	23.3N 142.1E	110	
12/5/76	22:01:22	23.0N 140.0E	393	
12/22/76	1:01:42	24.0N 145.0E	0	
1/5/77	22:44:57	23.3N 143.8E	0	
Date	Origin Time	Location*	Depth (km)	Region
Other Events				
10/22/76	18:35:24	56.1N 153.3W	0	Kodiak Islands
4/22/77	5:58:56	52.5N 138.8E	408	Kamchatka
4/23/77	0:52:05	75.0N 134.9E	0	New Siberian Is.
7/20/77	14:49:06	50.6N 161.9W	0	Alaska Pen.
8/7/77	23:26:55	52.2N 176.2W	125	Andreanof Is.

*Locations before 1975 from International Seismological Center, after 1975 from Seismic Data Analysis Center

Table 4

South American Earthquakes*

Date	Origin Time	Location	Depth (km)
4/25/67	10:26:14.3	32.6S 69.0W	39
11/15/67	21:35:51.5	28.7S 71.2W	15
2/6/67	11:19:23.1	28.5S 71.0W	23
4/21/68	9:24:35.5	23.4S 70.5W	41
4/30/68	23:51:17.9	38.4S 71.1W	40
9/30/76	8:04:11	24.2S 68.2W	0
12/3/76	5:27:34	21.0S 69.0W	79
12/4/76	12:32:35	20.0S 69.0W	103
3/8/77	22:46:44	8.0S 63.0W	0
3/13/77	4:55:55	2.0S 58.0W	0
4/15/77	23:35:38	22.9S 68.8W	109
6/ 2/77	16:50:36	29.9S 68.6W	94
6/ 5/77	2:46:07	24.0S 70.5W	30
6/ 8/77	13:25:16	22.1S 67.3W	135
6/18/77	16:49:42	21.0S 68.7W	125

*Locations before 1975 from International
Seismological Centre, after 1975 from Seismic
Data Analysis Center

divided only between northwest and south-southeast azimuths. The earthquake sources had slightly longer apparent periods of the first cycle of P wave motion than were observed for the explosion sources. The apparent period of the first P wave cycle for individual events ranged between 1.6 and 1.0 seconds, with a mode of 1.2 seconds. The individual stations exhibited a range of variation of apparent period of ± 0.2 seconds about the average apparent period for the whole network. Stations exhibiting a greater frequency variation were either noted as such, or else the event itself was discarded. While the individual stations occasionally exhibited slightly longer or shorter apparent periods than the network average, no station other than RKON showed a consistent, systematic deviation of frequency content. RKON at Red Lake, Ontario, in the Canadian shield often but not always was shorter period than other stations.

The origin times and locations of the earthquakes analyzed are presented in Tables 3 and 4. Twenty-one earthquakes to a northwest azimuth from the United States are listed in Table 3, and are subdivided among four groups: Kurile Islands, Japan, Bonin Islands, and other events. Fifteen earthquakes in South America are listed in Table 4 and are not subdivided. The amplitude data obtained from these events are presented in the Appendix in Tables A7 through A11. The amplitude data have been corrected for seismometer gain and corrected for geometric spreading to a common distance of $60d\Delta$, and are expressed as nanometers of ground displacement. The P waveforms of 4/25/67 South American earthquake are plotted in Figure 2. While the wave shape of the P wave maintains a relative simplicity and constancy over the whole WWSSN array in the United States, the absolute amplitudes vary by nearly a factor of twenty between LON, Longmire, Washington, and OXF, Oxford, Mississippi. Low amplitudes are seen at DUG, Dugway, Utah; TUC, Tucson, Arizona; and GOL, Golden, Colorado. High amplitudes are observed at LUB, Lubbock, Texas; DAL, Dal-

las, Texas; JCT, Junction City, Texas; and ATL, Atlanta, Georgia. Even though the data shown for the 4/15/67 event in Figure 2 represent a paradigm of amplitude variation for a simple earthquake, these amplitude data must be averaged with many other events to properly yield amplitude effects which may be attributable to the region of the receiving stations. Waveforms for many of the events in Tables 3 and 4 are plotted in a report by Butler and Hart (1979).

Amplitude Data Reduction

The absolute amplitudes of the events in Appendix Tables A1 through A11 measured at the WWSSN and filtered SDCS stations in the United States range in size from tens of nanometers to thousands of nanometers. While the explosions and earthquakes in Tables 2, 3, and 4 may have minimal amplitude variations across our network of seismic stations which are due to source effects, the events have different scale sizes; i.e., some events are bigger or smaller than others. Let us presume that the scale size of an event may be characterized by a constant α . The body wave magnitude, m_b , is such a constant and is determined from averaging m_b measurements made at stations all over the world. In our case we would like to determine the scale size constants α_i for i events directly from our own amplitude data set. If we divide our absolute amplitude measurements for event i by the scale size constant α_i , we have then effectively removed the size of the source and are left with a residual variation from station to station which is dimensionless and expresses the relative amplitudes of the stations. The relative amplitudes at a single station over many events is a distribution which may be characterized by the mean and the variance. The mean relative station amplitude characterizes the amplitude variation which may be attributable to the locale of the station. If the event scale size constants α_i are larger or smaller than necessary, the total variance of the relative

amplitudes summed over all stations will increase. A simple method of obtaining event scale size constants α_i is to let α_i be the average amplitude measured for event i . However, each station does not yield an amplitude measurement on every occasion - reason: poor signal to noise, no record, station down, amplitude off scale, etc - and thus the stations used in the network average would

vary from one event to another. A more efficient method is to determine the α_i while simultaneously assuring minimum total variance of the remaining relative amplitudes. An iterative procedure was adopted to obtain this end.

Let A_{ij} be amplitude measurements from the i events at the j stations for a given azimuth for the earthquake sources or for a given test site for the explosion sources. The A_{ij} have already been corrected for seismometer gain and geometric spreading. From the i events choose a master event k and divide the A_{kj} by the master event average value, β_k

$$\beta_k = \frac{1}{n_k} \sum_j A_{kj} \quad (2)$$

where n_k is the number of stations reporting the A_{kj} amplitude observations, $n_k \leq j$, for event k . Now for events $i \neq k$ determine scale factors α_i such that for each i

$$\min \sum_j \left[\alpha_i^k A_{ij} - \frac{1}{\beta_k} A_{kj} \right]^2 \quad (3)$$

is minimum. Using these scale factors α_i^k (where superscript k simply denotes reference to master event k) the squared variation of i events are minimized relative to the master event k . The total amount of squared variation is

$$U_k = \sum_{i \neq k} \sum_j \left[\alpha_i^k A_{ij} - \frac{1}{\beta_k} A_{kj} \right]^2 \quad (4)$$

As not all stations record amplitude data from each event, the total squared variation U_k for master event k is scaled by the number of elements m_k in the sum expression in (4)

$$V_k = \frac{1}{m_k} U_k \quad (5)$$

If the unscaled variation U_k were not rescaled to V_k , then the master event k which had the fewest observations would tend to produce the minimum total

variation; since if event k has no observation for station \hat{j} , observations at station \hat{j} for events i cannot be used in the sums in (3) and (4). Next iterate the master event k over the events i and choose the master event M which minimizes V_k

$$V_M = \min(V_k)_{k \neq k \text{ over all } i} \quad (6)$$

We now form scaled observations O_{kj}^M

$$O_{kj}^M = \frac{1}{\beta_k} A_{kj} \quad , k = M \quad (7)$$

$$O_{ij}^M = \alpha_i A_{ij} \quad , i \neq M \quad (8)$$

β_k is defined in (2), α_i is determined from condition (3), the superscript M on O_{ij}^M denotes an observation rescaled with the master event $k = M$. Each station j now has P_j observations from the i events, $P_j \leq i$. The mean relative amplitude for each station may be calculated

$$\mu_j^M = \frac{1}{P_j} \sum_i O_{ij}^M \quad (9)$$

Note that the O_{ij}^M were calculated relative to the master event M which produced a minimum average variance V_k . The estimate of mean relative station amplitude μ_j can be improved by substituting our preliminary estimate of μ_j - i.e., μ_j^M - into (3) for $\frac{1}{\beta_k} A_{kj}$

$$\min \sum_j \left[\alpha_i^* A_{ij} - \mu_j^M \right]^2 \quad (10)$$

and solving for α_i^* which minimizes (10). New scaled amplitude observations are formed

$$O_{ij}^* = \alpha_i^* A_{ij} \quad , \text{for all } i, j \quad (11)$$

The improved estimate of the mean relative station amplitude is

$$\mu_j = \frac{1}{P_j} \sum_i o_{ij} \quad (12)$$

where P_j is the number of events i for which the amplitude is measured for station j , $P_j \leq i$.

For this amplitude data set, it was found that the estimator μ_j is stable; such that further iterations are unnecessary. The sample standard deviation of the relative station amplitudes is then

$$S_j = \left\{ \frac{P_j \sum_i (o_{ij})^2 - \left[\sum_i o_{ij} \right]^2}{P_j(P_j - 1)} \right\}^{1/2} \quad (13)$$

and is defined when there is more than one observation, P_j .

For each event we now have a scale size, α_i , and for each station there is a mean relative amplitude, μ_j , and its standard deviation, S_j . A measure of the uncertainty of the mean, μ , is the standard error of the mean

$$SEM = S / \sqrt{n} \quad (14)$$

where n is the number of measurements at the station, and S the standard deviation of the distribution of relative amplitudes at the station. The 95% confidence limits on the mean is roughly twice the standard error of the mean

$$95\% \text{ confidence limits} = 1.96 \text{ SEM} \quad (15)$$

The variance of the distribution of relative amplitudes at a station is the square of the standard deviation

$$Var = S^2 \quad (16)$$

In compiling the results from the amplitude reduction, the station mean, standard error of the mean, and number are listed. From these quantities, the others may be easily calculated. For the explosion data the mean relative station amplitudes are determined for each test site. To obtain the mean relative

station amplitudes for a northern azimuth, the results of the five test sites are averaged. This process is accomplished by the same reduction as discussed above; where now, instead of averaging amplitudes from events, we are averaging relative amplitudes characteristic of each test site. We could have obtained relative station amplitudes for a northern azimuth by averaging the amplitude measurements without regard to test site. Averaging by test site first and then averaging the test sites was chosen for two reasons. (1) Some test sites had more events than others. If the amplitudes were averaged without regard to test site, some test sites would be weighted more heavily in the average. (2) For the east and west Semipalatinsk and western Kazakh sites, stations in the southern United States lie within the region of diffraction at the core mantle boundary. One of the spinoffs of this amplitude study is a more precise determination of the core-mantle shadow zone boundary at $95.5^\circ\Delta$ (Butler and Ruff, 1980; Ruff and Helmberger, 1981). For these reasons the Russian test sites were averaged separately.

The scale sizes α_i of the events are not actually used in this study. Though the α_i are potentially good estimators of the relative sizes of events, they measure only a small solid angle about the sources and are therefore of restricted utility.

The mean relative station amplitudes for a given test site or azimuth are determined relative to the group and not to a fixed baseline. We may then choose a baseline. The baseline chosen is that the geometric mean value of the mean relative amplitudes over all stations shall be equal to one. The geometric mean γ of the mean relative station amplitudes is

$$\gamma = \left[\prod_j \mu_j \right]^{1/n} \quad (17)$$

where $\prod \mu_j$ is the product of the means and j goes from 1 to n , the number of

stations. The mean relative amplitude is then defined

$$m_j = \mu_j / \gamma \quad (18)$$

With the mean relative station amplitudes in this format, we may then speak of station amplitude as being a factor of two greater than the mean (twice the amplitude) or a factor of two less than the mean (one-half the amplitude), where the mean refers to the geometric mean amplitude over all stations.

Amplitude Results for Three Azimuths

For each seismic station there are many relative amplitude determinations, each determination from a particular source event. The individual vagaries of the sources will contribute scatter to relative amplitude determinations even though we have minimized visible waveform variations. Unknown scattering bodies within the earth and lateral heterogeneity will cause the relative amplitudes determinations to scatter. Whatever the cause of the scatter, we have a distribution of relative amplitude determinations at each seismic station for the many events with respect to three azimuths. This distribution of relative amplitude determinations at each station may be characterized by the mean and the standard deviation of distribution. The mean of the distribution is an unbiased estimator of the relative amplitude of the station with respect to the network. The standard deviation measures the scatter of the relative amplitude determinations about the mean. The variance is the square of the standard deviation: the sum of the variances over all stations was minimized in the amplitude reduction procedure. Thus the scatter in the relative amplitude determinations is real, and minimum in a least squares sense with respect to all stations.

The relative amplitude patterns for three azimuths for twenty-five WSSN and SDCS stations in the United States are graphed in Figures 6, 7 and 8.

P WAVE AMPLITUDE DATA FOR U.S.A.

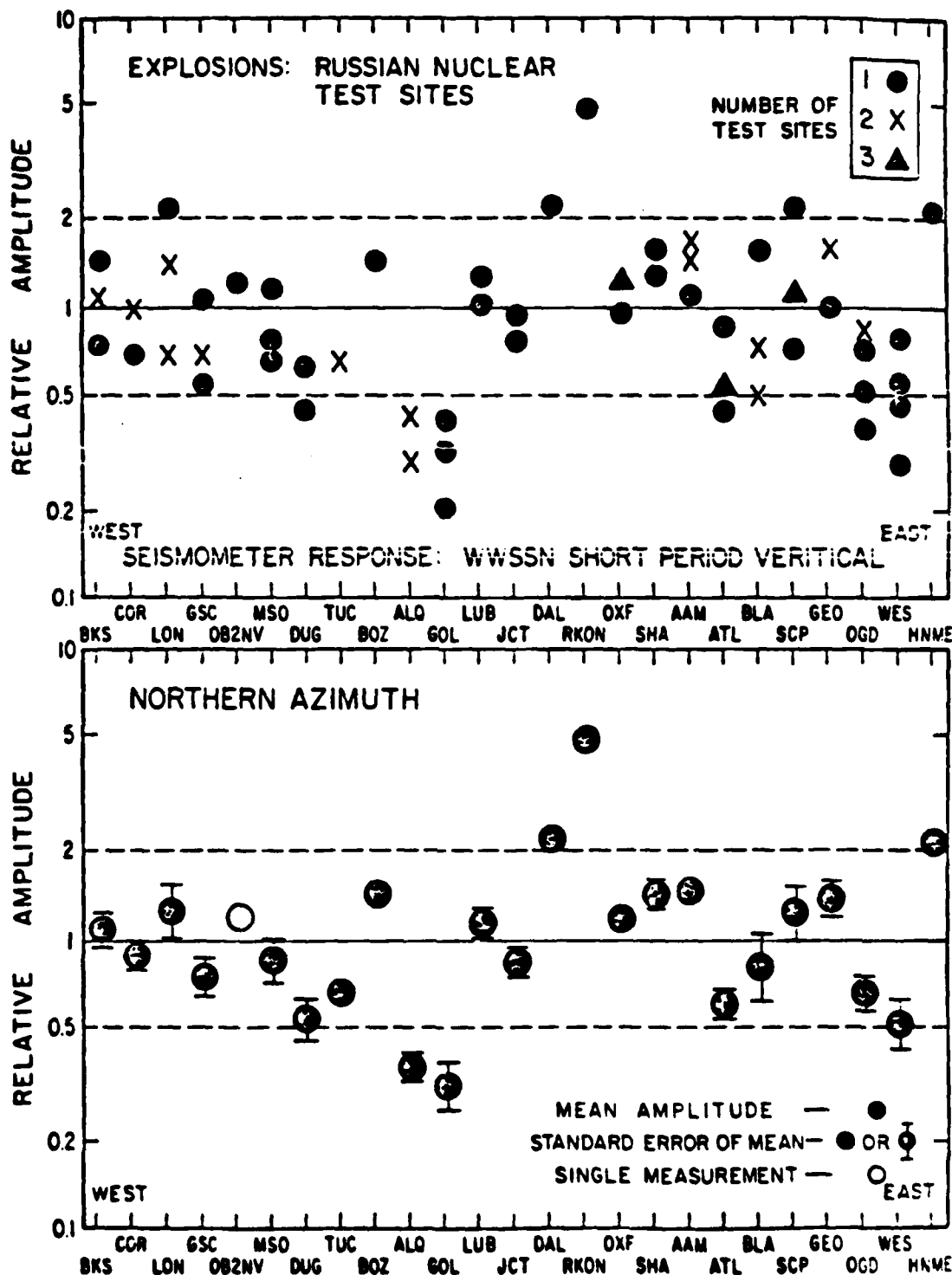


Figure 6. Relative amplitudes of short period P waves from Russian nuclear test sites are graphed above for WWSSN stations in the United States. The seismic stations are arranged by location in a west to east direction. The corresponding mean and standard error of the mean are graphed beneath. The vertical amplitude scale is logarithmic with unity equal to the geometric mean over all stations.

P WAVE AMPLITUDE DATA FOR U.S.A.

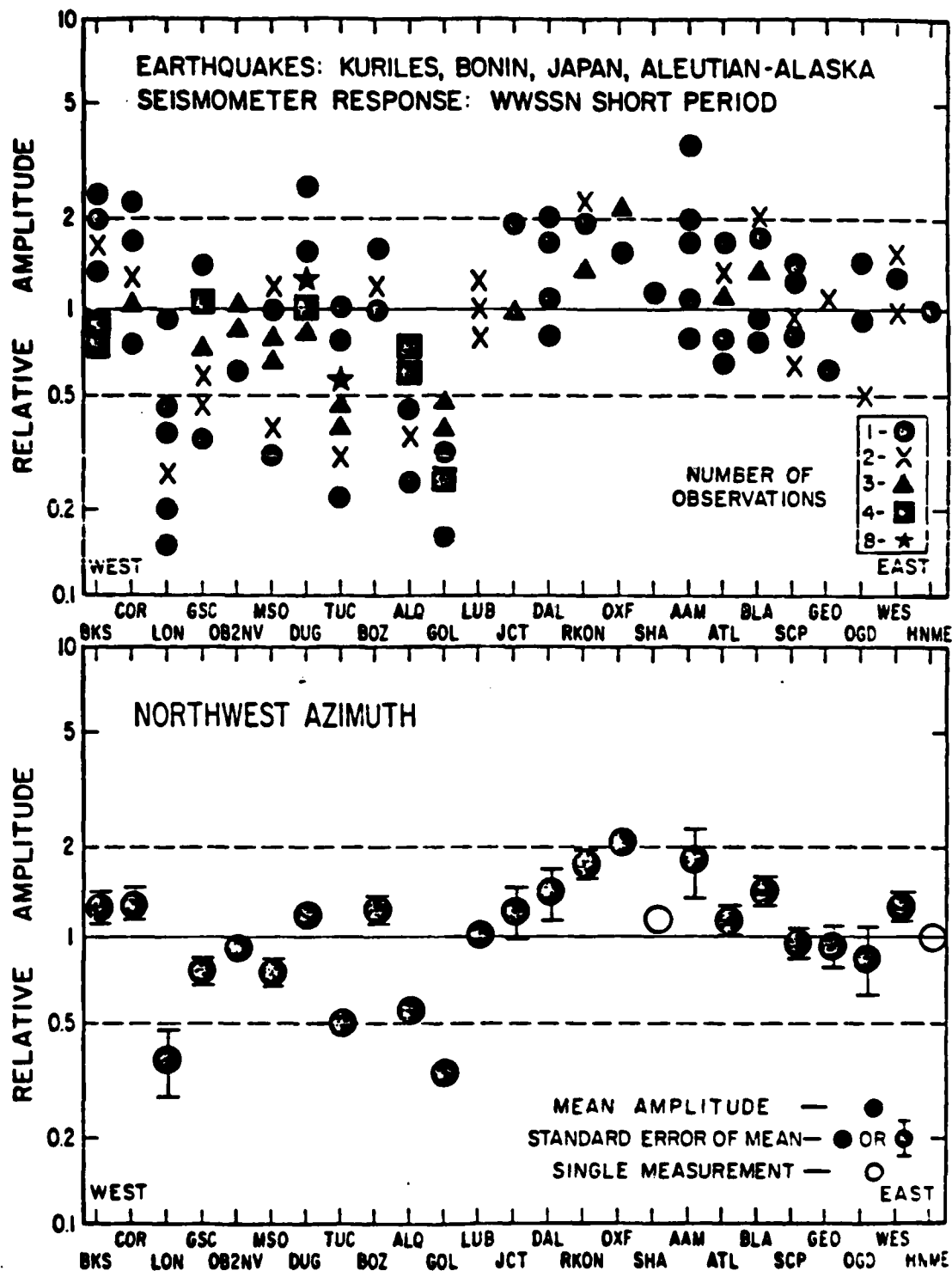


Figure 7. Relative amplitudes of short period P waves from earthquakes to a northwest azimuth from the United States are graphed above for WWSSN stations. The seismic stations are arranged by location in a west to east direction. The corresponding mean and standard error of the mean are graphed beneath. The vertical amplitude scale is logarithmic with unity equal to the geometric mean over all stations.

P WAVE AMPLITUDE DATA FOR U.S.A.

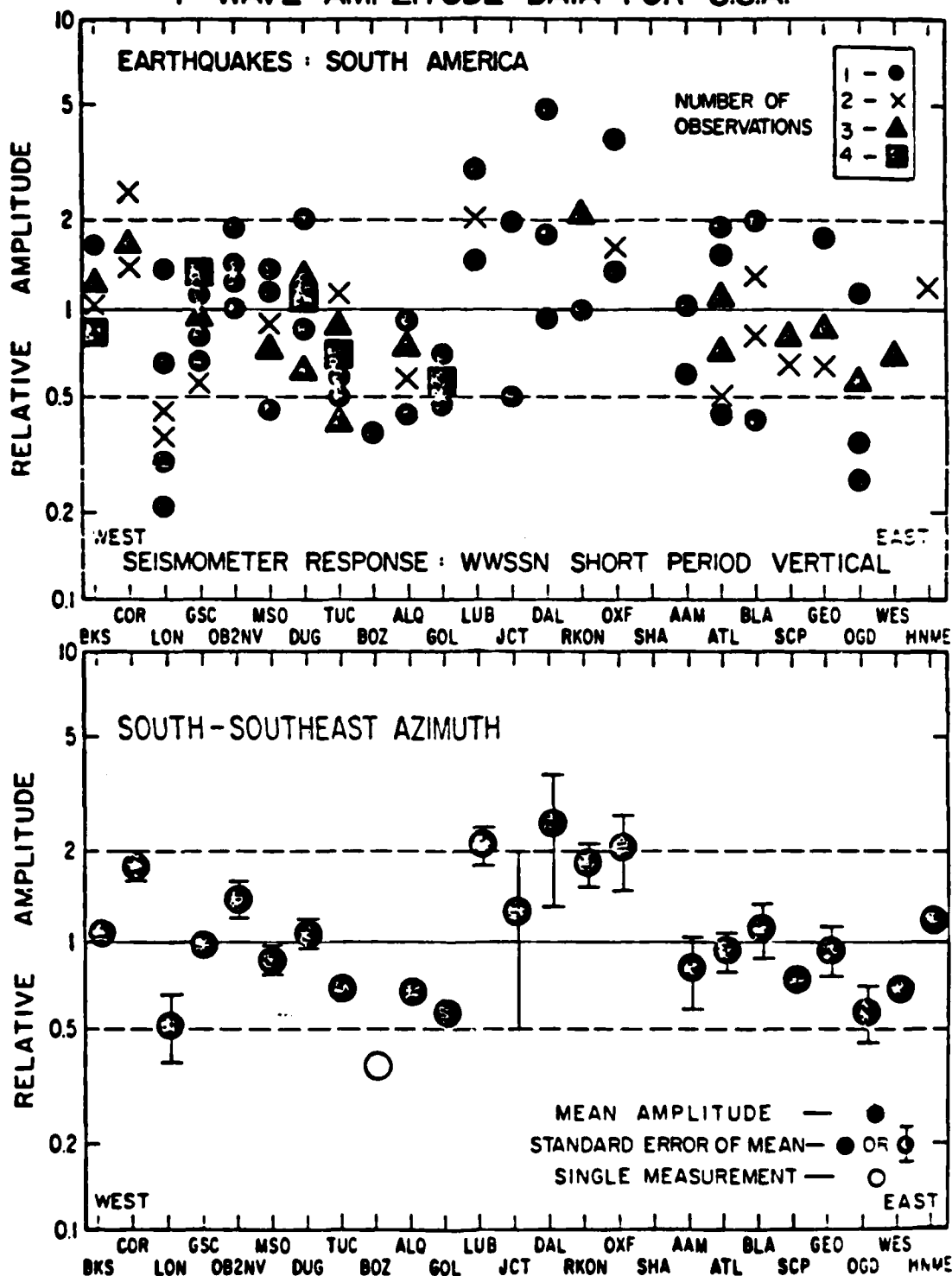


Figure 8. Relative amplitudes of short period P waves from earthquakes in South America are graphed above for WWSSN stations in the United States. The seismic stations are arranged by location in a west to east direction. The corresponding mean and standard error of the mean are graphed beneath. The vertical amplitude scale is logarithmic with unity equal to the geometric mean over all stations.

Amplitude data from a northern azimuth come from mean relative station amplitudes determined for five Russian nuclear test sites and are graphed in the upper part of Figure 6. The mean relative amplitudes were obtained using the amplitude measurements from Butler and Ruff (1980). To include the stations RKON, HNME, and OB2NV, three additional explosions from the Semipalatinsk east test site were integrated into the Butler and Ruff (1980) amplitude data set. Even though this presents RKON, HNME, and OB2NV with one to three measurements, the overall stability of relative amplitudes from individual nuclear test sites suggests that the individual amplitude variations will be close to the mean relative amplitude patterns determined from many events. The mean relative amplitudes for the twenty-five stations are listed left to right in a west to east fashion as they are located in the United States for a northern azimuth. The vertical scale is logarithmic and the axis of unity is the geometric mean of the distribution of data. The dashed parallel lines indicate the factor of two variation about the mean, or relative amplitudes of 2 and 0.5. To make clear the number of test sites when the data overlap, the X's and Δ's indicate two and three, respectively, test sites share a relative amplitude (to within the size of the symbol). Some stations have five determinations, some less due to distance range or variations of reporting (Butler and Ruff, 1980). Figure 6 also graphs the mean and the standard error of the mean for the data for the northern azimuth. If the standard error of the mean was smaller than the symbol size, it was not graphed. Individual measurements do not have a standard error defined and are shown as open circles.

This graphical representation of the data was chosen to best illustrate the interrelationship of the data, its mean and its standard error among the many stations. The west to east arrangement of the stations was chosen to provide geographical context to the data and to make visible possible west to east

amplitude variations. The three letter seismograph code names refer to the locations on the map of Figure 1; Table 1 lists the station names.

Two stations are a factor of two less than the mean for all test sites: ALQ, Albuquerque, New Mexico, and GOL, Golden, Colorado. Three stations have mean amplitudes consistently a factor of two greater than the mean: DAL, Dallas, Texas; RKON, Red Lake, Ontario; and HNME, Houlton, Maine. The stations OB2NV, Oak Springs Butte, Nevada, BOZ, Bozeman, Montana, LUB, Lubbock, Texas, SHA, Spring Hill, Alabama and AAM, Ann Arbor, Michigan, measure above the mean. Stations consistently measuring below the mean are DUG, Dugway, Utah, TUC, Tucson, Arizona, JCT, Junction City, Texas, ATL, Atlanta, Georgia, OGD, Ogdensburg, New Jersey, and WES, Weston, Massachusetts. The rest of the stations have relative amplitudes falling on both sides of the mean: BKS, Berkeley, California, COR, Corvallis, Oregon, LON, Longmire, Washington, GSC, Goldstone, California, MSO, Missoula, Montana, OXF, Oxford, Mississippi, BLA, Blacksburg, Virginia, SCP, State College, Pennsylvania, and GEO, Georgetown, District of Columbia. The stations which show the greatest scatter and consequently have the largest standard errors of the mean are LON, BLA, and SCP. The maximum amplitude ratio in the amplitude pattern for a northern azimuth is between RKON and GOL, where the mean amplitude of RKON is 15 times greater than GOL. The amplitudes at DAL and HNME are 6 to 7 times greater than the mean amplitude at GOL.

Amplitude data for a northwest azimuth from the United States are graphed in Figure 7. The formats of all of the amplitude figures in this paper are all the same to allow relative ease in comparing one set of data to another. The data in Figure 7 are from 21 earthquakes in Kurile-Japan-Bonin arc, Kamchatka, Eastern Siberia, Aleutian arc, and Alaska. The data in Figure 7 have similarities and differences with the amplitude pattern for a northern azimuth

in Figure 6. LON, TUC, and ALQ consistently report amplitudes less than the mean, while GOL observes amplitudes consistently a factor of two less than the mean. The amplitude observations at RKON and OXF are consistently greater than the mean. High amplitudes are noted at AAM, but also with relatively large scatter. Other stations with large scatter are LON and TUC. In contrast to LON and AAM, most of the amplitudes at TUC are centered near the mean relative amplitude and consequently the standard error of the mean at TUC is small.

Several stations show significant azimuth amplitude variation between north and northwest. DUG, Dugway, Utah and WES, Weston, Massachusetts have mean relative amplitudes that are a factor of two less than the network mean for Russian explosions to a northern azimuth, and shift to amplitudes greater than the network mean for the earthquakes to a northwest azimuth. For LON, Longmire, Washington, the situation is the reverse; where greater than average amplitudes are observed for nuclear explosions to the northern azimuth, an amplitude a factor of two less than the network mean is observed for earthquakes to a northwest azimuth. The stations ATL and BLA show azimuthal variations, but to a lesser extent than do LON, DUG, and WES. The range of amplitudes is slightly less for the northwest azimuth than for the northern azimuth. The amplitude ratio between RKON and GOL is 5.2 and is exceeded by the amplitude ratio of 6.1 between OXF and GOL. While ALQ is nearly as low as GOL for the explosion data, the relative amplitude of ALQ increases for earthquakes to a northwest azimuth.

The earthquakes to a northwest azimuth cover a broad region. These regions were subdivided in Table 3 and in Appendix Tables A7 through A10 to see if systematic source region effects could be resolved. Four figures are shown in the Appendix - Figures A1 through A4 - which jointly graph the mean relative amplitude pattern from all data to the northwest versus the amplitude

patterns from the four regional groupings in Table 3. No systematic source region effects were apparent.

The amplitude pattern for a south to southeast azimuth from the United States is graphed in Figure 8. Data from fifteen South American earthquakes are plotted in the upper part of Figure 8. The seismic stations COR, OB2NV, LUB, and RKON consistently have amplitudes greater than or equal to the network mean. The two measurements at HNME are greater than the network mean. Lower than average amplitudes are consistently observed at BOZ, ALQ, GOL, SCP, and WES. The single measurement at BOZ is less than half the network mean, and was the only measurement available from the earthquake data set in Table 4. Lay and Helmberger (1981) obtained three amplitude measurements at BOZ from four deep focus earthquakes in Peru; low relative amplitudes were determined at BOZ. However, TUC, ALQ, and GOL recorded smaller amplitudes than BOZ in the Lay and Helmberger (1981) data set. The amplitude determinations for LON in Figure 7 are again generally low, with large scatter. Other stations exhibiting relative large scatter of amplitude observation from the data set of South American earthquakes are DAL, OXF, ATL, BLA, and OGD. It appears that more stations of the WSSN in the United States exhibit large scatter for a south-southeast azimuth than for a northwest azimuth.

A number of azimuthal amplitude variations are seen at single stations. COR observes its highest amplitudes to a southeast azimuth. LON shows low amplitudes for the South American earthquakes, in agreement with a northwest azimuth and in contradistinction to high amplitudes observed from Russian nuclear events. DUC observed amplitudes near the network mean for a southeast azimuth. BOZ shows low amplitudes to the south, high amplitudes to north and northwest. GOL shows low amplitudes to the southeast, but not to the extent a factor of two less than the network mean - as was the case for GOL

to the north and northwest. LUB shows high amplitudes for a southern azimuth. WES has low amplitudes to the south and north, while higher amplitudes are observed to the northwest.

The lower amplitudes seen at BOZ, Bozeman, Montana from South American earthquakes are more than likely associated with the Yellowstone hot spot. High temperatures beneath Yellowstone will lead to greater attenuation of seismic waves passing through the region. The large regional geoid high in the western United States is centered on Yellowstone. However, though a straightforward cause may be noted for the low amplitudes at BOZ for a southern azimuth, equally low amplitudes are observed at GOL, ALQ, and TUC. In interpreting the amplitude patterns for the network, consideration must be given to individual station effects, but effects noted in common at many or several stations must be considered together.

The relative amplitude pattern for a south-southeast azimuth in the lower part of Figure 8 shows a smaller range of amplitude variation between the high and low stations than was seen for the northern azimuth. The relative amplitude ratio between DAL and BOZ for the South American data is 6.7, while the ratio of RKON to GOL is 3.2. This range of amplitudes is comparable to the range for northwest azimuth.

The amplitude data for a northwest azimuth were subdivided into four regions to see if near source regional effects might be detected in the data. No systematic relationships were apparent. While there were no obvious regional subgroups into which to divide the South American amplitude data, the individual events were plotted in relation to the mean relative amplitude pattern from all the data to see if any of the events showed systematic trends. None of the individual South American events evinced an apparent biasing trend with respect to the mean relative amplitude pattern for the south-southeastern azimuth.

Station Mean Relative Amplitude Summary

A summary table of the station mean relative amplitudes is presented in Table 5 for the three azimuths in this study. The standard error of the mean and the number of observations is given. For the northwest and south-southeast azimuths the number of observations refers to the number of earthquakes. For the northern azimuth the number of observations refers to the number of Russian nuclear test sites. The earthquake data have been corrected for geometric spreading to a common distance of $60d\Delta$. The explosion data have not been corrected for geometric spreading, and thus the northerly stations are about 10% too large and the southerly stations 10% too small. Individual summary lists for Russian test sites are found in Tables A12 through A17 in the Appendix and were discussed in Butler and Ruff (1980). Individual summary lists for the four regional subgroups of earthquake data to a northwest azimuth are found in the Appendix as Tables A18 through A21.

Mean Amplitude Pattern for the United States and Southern Canada

To obtain a mean amplitude pattern for the United States and southern Canada, the mean relative amplitudes for the three azimuths - N, NW, and SSE - were weighted equally and averaged together. The averaging process was accomplished in the same way that the data were reduced - by minimization of total variance. The mean relative amplitudes for the United States are graphed in Figure 9. The error bars in Figure 9 contain the standard error of the mean over all azimuths. The pattern from left to right is one of mean amplitudes decreasing from the west coast eastwards, reaching a low at GOL on the Rocky Mountain Front Range, jumping to greater than the mean in Texas, reaching its height at RKON on the Canadian shield, and decreasing toward the mean toward the east coast stations. The striking feature of Figure 9 is the amplitude

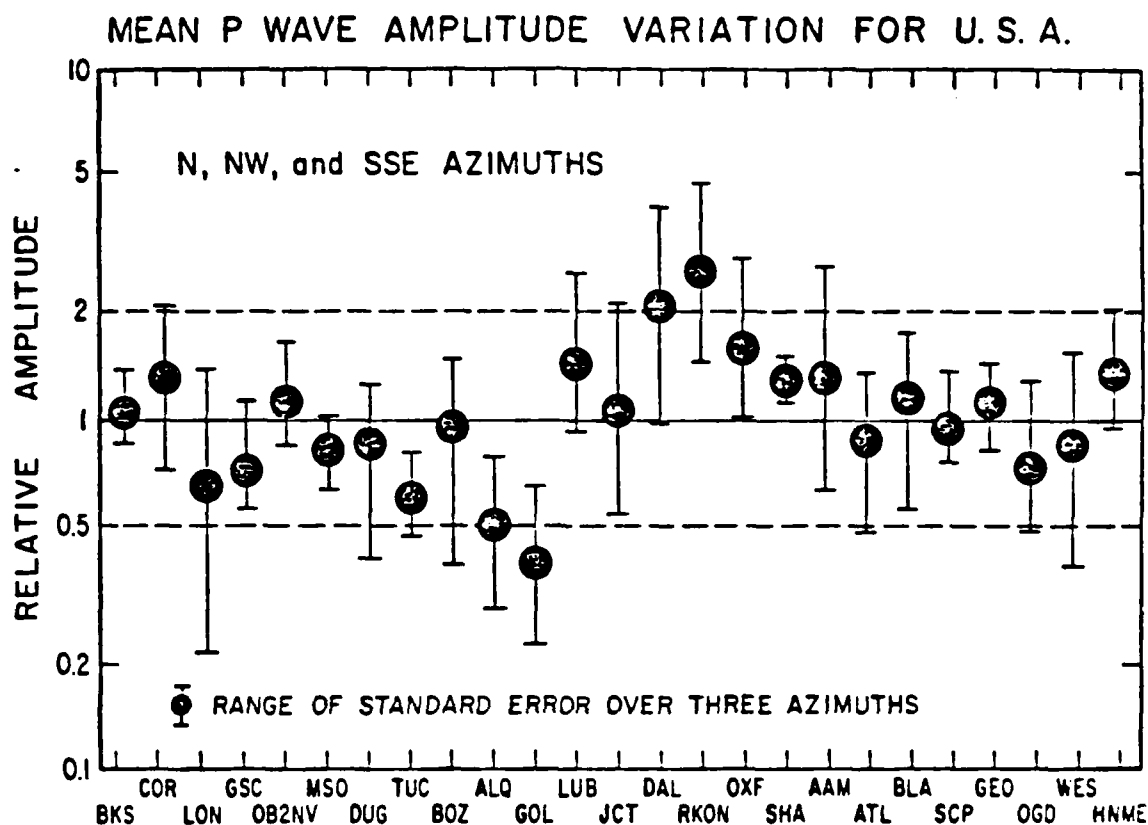


Figure 9. The relative amplitude variation for the N, NW, and SSE azimuths are averaged to obtain a mean P wave amplitude variation for the United States and southern Canada. The error bars represent the total range of the standard errors of the means for the three azimuths.

Table 5
Mean P Wave Amplitudes and Standard Error of the Mean

Station	Russian Explosions to North			All Earthquakes to Northwest			South American Earthquakes		
	Mean	S.E.M.	N	Mean	S.E.M.	N	Mean	S.E.M.	N
(west)									
BKS	1.10	0.14	4	1.26	0.16	13	1.09	0.08	10
COR	0.89	0.10	3	1.30	0.17	8	1.83	0.18	7
LON	1.27	0.28	5	0.38	0.10	7	0.52	0.13	8
GSC	0.75	0.11	4	0.76	0.08	13	0.99	0.09	12
OB2NV	1.22	[0.10] [*]	1	0.91	0.06	7	1.39	0.18	4
MSO	0.87	0.16	3	0.75	0.09	12	0.87	0.10	8
DUG	0.54	0.09	2	1.18	0.10	17	1.07	0.12	12
TUC	0.66	0.02	2	0.51	0.04	19	0.69	0.07	14
BOZ	1.44	[0.10] [*]	1	1.24	0.13	4	0.38	[0.14] [*]	1
ALQ	0.37	0.04	4	0.57	0.05	12	0.68	0.06	7
GOL	0.32	0.06	3	0.34	0.03	12	0.58	0.03	6
LUB	1.15	0.12	2	1.02	0.09	6	2.15	0.31	4
JCT	0.85	0.08	2	1.22	0.24	4	1.26	0.76	2
DAL	2.23	[0.10] [*]	1	1.42	0.28	4	2.53	1.20	3
RKON	4.89	[0.10] [*]	1	1.77	0.20	6	1.85	0.30	4
OXF	1.19	0.08	4	2.09	0.18	4	2.10	0.59	4
SHA	1.14	0.15	2	1.14	[0.12] [*]	1	-	-	-
AAM	1.48	0.10	5	1.84	0.49	5	0.61	0.22	2
ATL	0.60	0.07	5	1.14	0.11	8	0.94	0.14	11
BLA	0.81	0.20	5	1.44	0.18	8	1.11	0.23	6
SCP	1.26	0.25	5	0.95	0.11	7	0.75	0.04	5
GEO	1.40	0.20	3	0.92	0.15	3	0.94	0.17	6
OGD	0.65	0.09	5	0.85	0.22	4	0.58	0.12	6
WES	0.52	0.10	4	1.27	0.13	5	0.69	0.02	3
HNME	2.14	[0.10] [*]	1	1.00	[0.12] [*]	1	1.18	0.00	2
(east)									

^{*} Estimated from geometric mean S.E.M. over other stations

variation between the Rocky Mountain Front Range station GOL and the Superior Province Canadian shield station RKON. The change between low amplitudes at GOL and at ALQ in the Rio Grande rift and the moderate to high amplitudes in Texas is sudden. This is the boundary between the late Cretaceous and Cenozoic orogeny of the Rocky Mountains and the Great Plains - a craton stable since Phanerozoic times. The amplitude jump also marks a change of seismometer siting from hard rock sites in the west to sedimentary siting in the central United States. The highest amplitude in Figure 9 lies on a section of the Canadian shield with a 2.5 billion year age (Stockwell, 1964). This amplitude pattern is similar to previous LRSM amplitude studies, where low amplitudes are found in the west and high amplitudes in the east (Cleary, 1967; Evernden and Clark, 1970; Booth et al., 1974). As in the previous studies there is variability. In Figure 9 the only consistently low amplitude stations are MSO, TUC, ALQ, and GOL. The consistently high amplitude stations are DAL, RKON, OXF, and SHA. Three of the four high amplitude stations - DAL, OXF, and SHA - lie along the Gulf Coast and are situated on low velocity sediments which effectively amplify the ground signal. Four high stations not situated on sediments are COR, OB2NV, RKON, and HNME. The high amplitudes at OB2NV lie within the Great Basin province of Nevada in an area of low observed heat flow (Sass et al., 1971, 1976).

The mean relative amplitudes from Figures 6, 7, and 8 are presented in Figure 10 in relation to simplified physiographic provinces of the United States. In general three symbols are plotted at each station representing the mean relative amplitudes for the three azimuths. The symbols are located N, NW, and SSE of the station location to indicate direction of azimuth. Upward pointing triangles represent mean relative amplitudes which are factors greater than the network geometric mean amplitude. Downward pointing triangles represent mean relative amplitudes which are factors less than the network geometric

SHORT PERIOD P WAVE RELATIVE AMPLITUDES

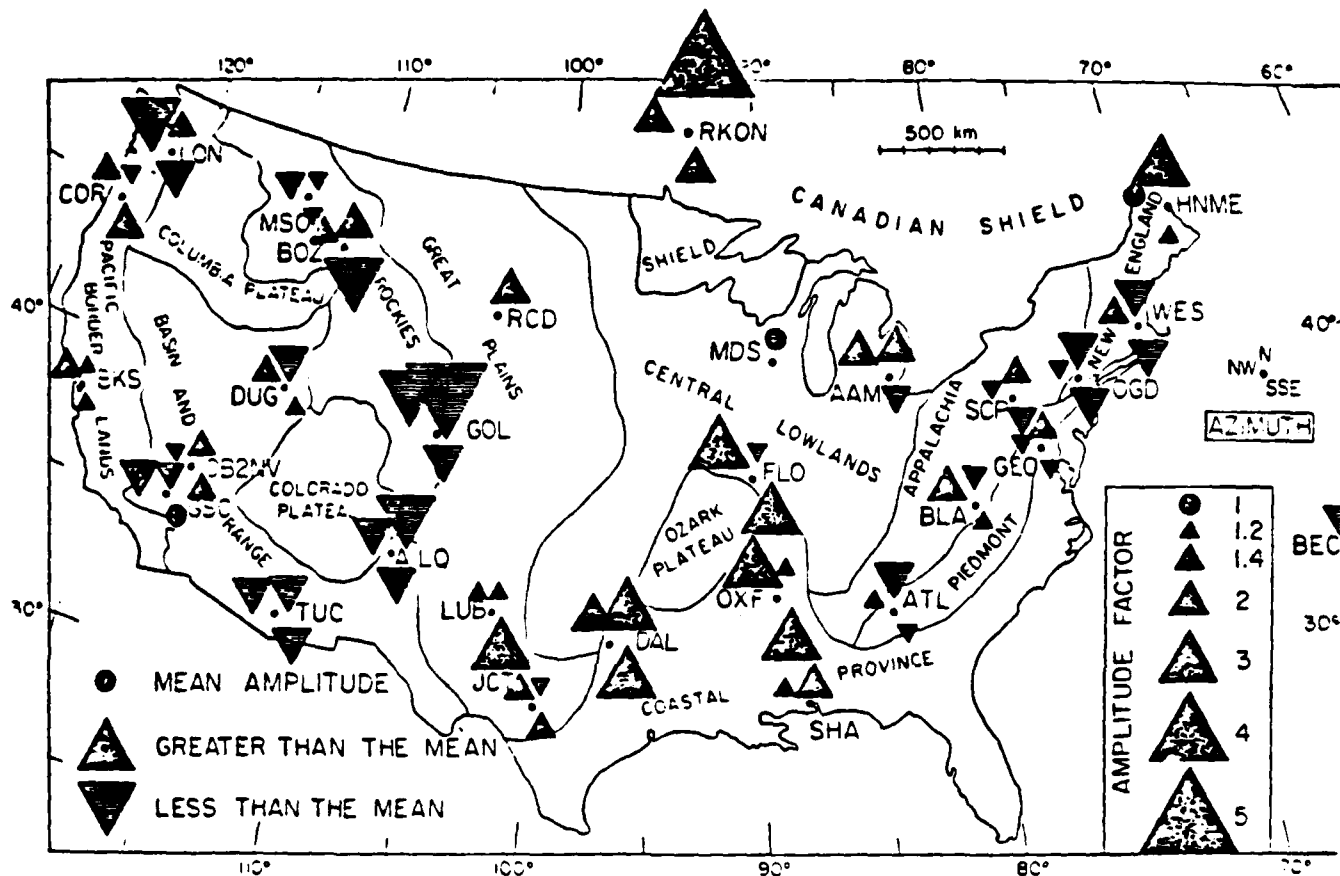


Figure 10. Short period P-wave amplitude anomalies are plotted relative to station location and approximate physiographic province within the United States. Upward pointing triangles are values greater than the mean, downward pointing are values less than the mean. A circle indicates a mean amplitude. The amplitude factor relative to the mean is noted at the lower right. The position of the triangle relative to each station indicates azimuth: north, northwest, southeast. The data to the north are from explosions in Russia. The data to the northwest and southeast azimuths are from earthquakes in Asia and South America with simple sources.

mean. The circles represent mean relative amplitudes which are at the network geometric mean. The size of the symbol is scaled to the deviation from the network geometric mean. For example, to a NW azimuth, HNME in Maine records an amplitude at the network geometric mean, TUC in Arizona records an amplitude of 0.5 or a factor of two less than the geometric mean, while RKON in Ontario records an amplitude a factor of two greater than the network mean. Supplemental data for RCD, Rapid City, South Dakota; MDS, Madison, Wisconsin; FLO, Florissant, Missouri; and BEC, Bermuda were taken from Butler and Ruff (1980). Many of the features of this figure have been discussed in previous sections: lowest amplitudes in the Rockies at GOL and south of BOZ, and in the southeastern Basin and Range at TUC and ALQ; lower amplitudes to the northwest of GSC and OB2NV, north DUG, and between COR and LON; scattered high amplitudes in the west; high amplitudes in the center of the continent; and moderate high and low amplitude variation in the Appalachias and at the east coast. Note, however, that the amplitudes reported have not been corrected for any site amplification effects for the seismometers situated on low velocity sediments.

Amplification Effects of Shallow Sediments

The amplification of seismic waves recorded at seismometers situated on soft sediments relative to seismometers situated on hard bedrock has been known for some time. Literature references include Gutenberg (1956, 1957), Carpenter et al. (1967), Borchardt (1970), Booth et al. (1974), and Butler and Ruff (1980). The effect may be understood fairly easily by comparing two elastic springs with different spring constants - one relatively stiff and one relatively flexible. Let us suppose that the springs are free at one end, as an analog to the free surface of the earth where the seismometer is placed. Now consider

elastic waves with the same energy propagating through both springs. As the elastic waves reach the free ends of the springs, the relatively flexible spring has more "give" and stretches further than the stiff spring. The greater stretch in the flexible spring relative to the stiff spring is equivalent to the larger amplitudes seismic waves produced in sediments versus hard rock. For the P

waves measured in this amplitude study the apparent period is about 1 second and the phase velocity (at a representative distance of $80^\circ\Delta$) is about 17 km/sec, such that the wavelength of the P waves is on the order of 17 km. The question then is: given the relatively long wavelengths, how much effect will shallow sediments have upon the P wave amplitudes? Butler and Ruff (1980) performed numerical experiments using Thomson-Haskell propagator matrices and a synthetic explosion waveform to derive the receiver effect of a variety of different sediment structures overlying bedrock relative to a simple bedrock site. For shallow sediments having an average velocity of 2 km/sec, a 200 meter thick surface layer amplified the P waves by a factor of 1.1 while thicknesses 300 meters and more amplified the P waves by a factor of 1.4 to 1.8. Shallow sediments with higher velocities produced less amplification. The relative amplification of sediment sites versus bedrock seismometer sites is a function of the sediment thickness and sediment velocity. Table 11 lists the results of the numerical experiments of Butler and Ruff (1980) for sediment layers of constant velocity and velocity gradients for various velocities and thicknesses. The average velocity in the top 1/2 kilometer essentially determines the relative amplification of the P waves in this study. As most of the central and southeastern portions of the United States are covered by sediments, the effect of sediment amplification is important in understanding the variation of P wave amplitudes.

To provide a standard bias of comparison of P wave relative amplitudes, those seismic stations situated on sediments must be corrected for the sediment amplification effect relative to the stations situated on hard bedrock. Seismic velocity well logs provide accurate velocity control of surface sediment layers, but this type of information was obtainable only at SHA, Spring Hill, Alabama. Short (<10 km) seismic survey lines are sensitive to uppermost crustal

Table 11
Sediment Amplification Effects for P Waves*

Sediment amplification**	Sediment description*** P wave velocity, thickness
1.8	unconsolidated sediments, 2.0 km/sec at surface and thicknesses of 2+ km with increasing velocity w/depth
1.6	2.0 km/sec at surface and thickness of 400-500 meters 2.5 km/sec at surface and thicknesses of 1-2 km with increasing velocity w/depth
1.5	3.0 km/sec, 2 km thick
1.4	2 km/sec, 300 meters thick 3 km/sec, 3 km thick with increasing velocity w/depth
1.3	3.5 km/sec, 2+ km thick with increasing velocity w/depth
1.2	3.0 km/sec, 500 meters
1.1	2 km/sec, ≤ 200 meters thick

- * at a period $T \sim 1$ sec.
- ** relative to a bedrock site.
- *** sediment layers overlay $V_p = 6.0$ km/sec bedrock.

layers; however, only at BKS, Berkeley, California was such a survey carried out and made available (T. McEvilly, personal communication, 1982). Long seismic refraction survey lines provide only general control as sediments are grouped in a single layer characterized by the highest velocity arrival. To estimate shallow sediment velocities and hence from Table 11 the relative sediment amplification where seismic refraction lines or well log control is not available - this is most often the case - recourse must be taken from geologic site information and systematics between velocity, and lithologic type and age of the sediments. Limestone velocities are sensitive to the extent of crystallization and range between 1.7 and 6.1 km/sec (Press, 1966). Faust (1951) developed empirical systematics of shale and sandstone seismic velocities as a function of depth and geologic time from velocity data from over 500 wells in the United States and Canada. Marrying the shale and sandstone velocity-depth-age systematics of Faust (1951) to the qualitative sediment velocity-amplification relationship in Table 11, an approximate geologic age versus relative amplification relationship was derived for sandstone and shale sediments with thicknesses of 300 meters or greater. Table 12 lists this relationship of shale and sandstone geologic age and amplification of P waves relative to hard bedrock sites. Naturally, the relationships in Table 12 must be regarded as only approximate, and were developed only from the necessity to apply corrections for sediment (shale and sandstone) amplification in a systematic fashion. Velocity information on other sedimentary materials - chalk, gypsum, mud, etc. - were obtained from Press (1966) and appropriate amplification corrections were deduced from Table 11. In interpreting the P wave amplitude variations in the upcoming section, corrections for the amplification effects of surface sediment cover at the seismometer sites will be adopted from Tables 11 and 12.

Table 12

Seismic Amplification for Seismometer
Site on Sandstone and Shale Relative to
Hard Bedrock*

Geologic Age of Sandstone and Shale	Relative P Wave Amplification** (Approximate)
Precambrian	1.0
Lower Paleozoic Cambrian Ordovician Silurian Devonian	1.3
Upper Paleozoic Mississippian Pennsylvanian Permian	1.4
Mesozoic	1.6
Cenozoic	1.8

* $V_p = 6.0$ km/sec

** Stratigraphic thicknesses ≥ 10 meters or greater.

Focussing/Defocussing and Scatter Effects at Seismometer Sites

Fluctuations of P wave amplitudes due to local elastic focussing/defocussing and scattering effects are obviously likely contributors to observed P wave amplitude variations in the United States. In the amplitude stability section of this paper the variability of P wave relative amplitudes among seismic stations in a region was examined. This section focusses on more site specific effects.

Dipping planar structures beneath a seismometer site tend to diminish the amplitude of a P wave recorded on the vertical component of a seismometer by transferring elastic energy to the horizontal components of P wave motion. The existence of transverse or tangential components of P wave move is diagnostic of dipping structure beneath a particular site (Burdick and Langston, 1977; Langston, 1977). Model studies of dipping planar structure by Langston (1977) show that a 10° dip on the Moho beneath a seismic station can reduce the P wave amplitude on the vertical component of motion of the long period seismometer by 10%. Anomalous tangential components of P wave motion have been noted at COR, Corvallis, Oregon (Burdick and Langston, 1977; Langston, 1977; Langston, 1981) and at LON, Longmire, Washington (Langston, 1979). This suggests that the mean amplitudes of P waves at COR and LON - which were measured from the vertical components of motion of the short period WWSSN seismographs - are slightly underestimated relative to other WWSSN stations in the United States.

Seismic stations situated on sedimentary basins can experience elastic focussing/defocussing effects. Calibrated nuclear explosions at Yucca Flats in Nevada - a long, trough-like sedimentary basin offset by several large block faults in its basement - show a systematic trend in their global average magnitudes, m_b , from one side of the basin to the other (Hart et al., 1979). The distribu-

bution of magnitudes has a standard deviation of (0.13) which is equivalent to an amplitude variation of about a factor of 1.3 about the mean for the basin. By reciprocity arguments (see, for example, the appendix of Chang and von Seggern, 1980) mean relative amplitudes of seismometers located at different places in Yucca Flats will also vary. This variability has been observed and quantified using minimum entropy deconvolution techniques and modeled by Hart et al. (1979) using the glorified optics method of Hong and Helmberger (1979). Hart et al. (1979) demonstrated that changes of seismic station locations, at Yucca Flats by several kilometers can change apparent magnitudes by (0.1), equivalent to a factor of 1.25 in amplitude. Note that while the apparent source strengths of the underground explosions exhibited a factor of 1.3 average variation about the mean (i.e., greater than and less than the mean), the receiver studies of seismic stations at the surface of the basin showed a total variation of about a factor of 1.25 between the largest and smallest amplitude. The receiver function studies at the Yucca Flats sedimentary basin indicate that seismic stations situated on complex sedimentary structures may exhibit amplitude variations of a factor of 1.1 to 1.2 about the mean amplitude value for the basin.

Haddon and Husebye (1978) have modeled a smoothed version of the NORSAR amplitude anomalies with a two dimensional heterogeneous layer at depths around 150 to 200 km or the bottom of the lithosphere. The velocity perturbations required to account for the NORSAR amplitude observations were of the order of a few per cent. Haddon and Husebye (1978) indicate that the thin lens model does a good job matching P wave travel time anomalies at NORSAR. This result was said to demonstrate that travel-time and amplitude anomalies observed across the large-aperture array NORSAR are intimately correlated and consequently have the same origin (Haddon and Husebye, 1978). In their

azimuthal study of LASA amplitude variations Chang and von Seggern (1980) state that the LASA amplitude anomalies are linearly related to travel time anomalies, with large amplitudes being related to late travel times. These amplitude and travel time variations at LASA were discussed in relation to crust-mantle models of Greenfield and Sheppard (1969) and Iyer (1971) which involve a varying, dipping Moho beneath LASA. As the Haddon and Husebye (1978) study also showed a positive correlation between amplitudes and travel time for P waves at both LASA and NORSAR, then large amplitudes relate to slow travel times and small amplitudes relate to fast times.

The success of Haddon and Husebye (1978) in mapping NORSAR P wave amplitude and travel time anomalies into varying elastic structure beneath NORSAR suggests that some part of the amplitude variations in the United States found in this present study and in others are due to elastic focussing/defocussing effects of laterally varying uppermost mantle structure. Using the three-dimensional block velocity model of the upper mantle beneath the United States of Romanowicz (1979), one might expect to be able to estimate areas of focussing or defocussing. Interestingly, one can easily show that, statistically, P wave amplitude and travel-time variations do *not* correlate well for either the WWSSN station or the LRSM stations in the United States. In comparing WWSSN amplitudes presented here with P wave travel time anomalies from Romanowicz (1979) and the LRSM amplitudes of Cleary (1967) with the LRSM travel time anomalies of Cleary and Hales (1966), both comparisons yield a correlation coefficient of less than 0.1 where a perfect correlation is 1.0. The correlation between Sengupta (1975) P travel time station anomalies from deep earthquakes and the WWSSN mean relative amplitudes presented here has less than a 0.5 correlation coefficient. This result indicates that while P wave amplitudes and travel times may correlate over an area of $\sim 10^4$ km², for an area the

size of the United States - nearly 800 times greater - P wave amplitudes do not correlate statistically with travel times. This in turn suggests that local variations of amplitude may be influenced by elastic focussing/defocussing effects which will also influence local travel time variations. For areas of 10^6 to 10^7 km² in size observed P wave amplitude variations cannot be ascribed wholly and simply to elastic focussing/defocussing effects. To explain the amplitude variations across the United States we shall have recourse in energy loss mechanisms such as anelastic attenuation or Q.

Random scattering will induce variations in the P wavefront as it propagates. The seismic station LON, Longmire, Washington situated on the flank of the volcano Mt. Ranier exhibits a large standard deviation in measured P wave amplitudes, extreme azimuthal amplitude variability, and noticeable waveform complexity of P waves relative to other stations in the United States. These characteristics may be attributed to some scattering effect, but little is gained in doing so. The question is how such an appellation will increase our knowledge as to what is actually happening. The appellation scattering begs a whole series of further questions: where is it occurring? What are the velocity perturbations? What are the size of the scatterers? Is part of the effect anelastic? How does it affect mean travel times or amplitudes? How is it related to the standard deviation? What does it imply in regards to earth processes? What is its frequency dependence? How important are scattering losses in relation to anelastic attenuation or in relation to elastic focussing/defocussing effects from deterministic structure? None of these are easy questions. Some researchers (e.g., Aki, 1973; Capon, 1974; Berteussen et al., 1975) have used the Chernov (1960) approach to random media. Butler and Ruff (1980) compared amplitudes of P wave secondary arrivals to the amplitude of the first cycle of P wave motion of Russian nuclear explosions. If scattering was the predominant

mechanism underlying the P wave amplitude variations, then the testable hypothesis was whether low amplitude P waves showed large secondary (scattered) arrivals while high amplitude P waves exhibited minor secondary arrivals. The results Butler and Ruff (1980) found were that the secondary P wave arrivals followed in relation to the primary P wave amplitude and that the simple test of the scattering hypothesis did not fit the data.

Scatter in the amplitude data does exist in Figures 6, 7, and 8 - yet it is unclear where along the path between source and seismometer it is most important. Obviously, at LON the receiver region is important. The average standard deviations of amplitudes from the individual Russian test sites are lower than are the average standard deviations of amplitudes measured from collections of earthquake sources. However, the standard deviations of amplitudes from the northern azimuth, which are averaged over the five Russian test sites, have values comparable to the average standard deviation of amplitude for the northwest and south-southeast azimuths comprised of earthquakes. This shows that variation among the source regions contribute to the scatter of P waves, while P wave amplitudes from a small source region have relatively low scatter. Scatter is an important phenomena which may be qualitatively discussed, but not quantitatively addressed easily. In interpreting the mean relative amplitudes at individual seismic stations the influence of scatter in relation to other seismic amplitude effects must be considered and weighed, but a more quantitative evaluation must await a more refined seismic experiment.

Mapping P wave Amplitude Variations into Q_a

The density and elastic properties of the seismometer site enter into the energy amplitude relationship. It was for this reason that site corrections for sediment amplification were derived earlier. By correcting the amplitudes of seismometers situated on sediments to values appropriate for hard bedrock, the seismometer site effects are normalized to a common basis. Note, however, that estimated sediment amplitude corrections are squared in transformation to energy. Therefore, the uncertainties in the true corrections also squared. With the corrections for sediment amplification applied, the square of the relative amplitude variation in the United States is equivalent to the variation of relative energy content in the P wavefronts recorded by the seismic stations.

By transforming the amplitude variations into seismic energy variations, effective Q variations naturally follow. Let us assume for the moment that the energy variations are due to energy losses from attenuation. From the definition of the quality factor Q (e.g. Anderson, 1967),

$$\Delta E / E = 2\pi / Q \quad (20)$$

where ΔE is the energy loss per cycle. In an attenuating medium characterized by the dissipation parameter Q, in each cycle of motion the energy decreases by a factor of $[1 - 2\pi / Q]$, and over n cycles the decrease is a factor of $[1 - 2\pi / Q]^n$. Since the amplitude variations in the United States are relative, then the energy variations and hence the energy losses are relative. Since the amplitude variations were developed in relation to the geometric mean amplitude for the United States, then the energy variations are in relation to the mean energy. If the P waves at each seismic station i have incurred energy losses from attenuation due to a local Q_i , then the geometric mean amplitude in the United States has incurred an energy loss from attenuation due to Q_{av} , the average Q.

Illustrative example: let station i record a P wave amplitude A_i and station m record amplitude A_m with both stations situated on the same material, and let the P waves recorded at both stations have the same apparent period. Then the energy E_i at station i is related to the amplitude A_i by $E_i \sim A_i^2$, and at station m the same relation in $E_m \sim A_m^2$. Since the two seismic stations are situated on the same material and the P waves recorded have the same apparent periods, the squared amplitude ratio equals the energy ratio:

$$(A_i / A_m)^2 = E_i / E_m \quad (21)$$

Now assume that the energy in the P wavefronts at both stations i and m were equal to E_0 at some depth and that energy losses were incurred in propagation through an attenuating region. If the energy loss occurred over n cycles, then

$$E_i = E_0 \left[1 - \frac{2\pi}{Q_i} \right]^n \quad (22)$$

and

$$E_m = E_0 \left[1 - \frac{2\pi}{Q_m} \right]^n \quad (23)$$

where Q_i and Q_m are the average quality factors controlling the attenuation at station i and m , respectively. Substituting (22) and (23) into (21) and canceling the common energy E_0 , a relation between relative amplitude and relative Q is derived

$$\left(\frac{A_i}{A_m} \right)^2 = \frac{\left[1 - \frac{2\pi}{Q_i} \right]^n}{\left[1 - \frac{2\pi}{Q_m} \right]^n} \quad (24)$$

Note that in (24) only the ratio of the measured P wave amplitude enters. Since only the ratio is important, let $A_m = 1$, that is, station m records amplitudes at a level equal to the geometric mean amplitude for the United States. Then, $Q_m = Q_{AV}$, the average level of attenuation beneath the United States over n cycles of motion.

In mapping the variations of P wave amplitudes into variations in Q_a beneath the seismic stations following the method of the previous section all other effects influencing the P wave amplitudes must be corrected. Amplification effects for seismometers situated on sediments relative to hard bedrock sites are most important and most easily recognized. Elastic focussing/defocussing effects are second in importance, but their specific influence is unknown at almost all seismic stations at this time. Following amplitude stability results in a previous section, amplitude variability among stations of a region averages at about a factor of 1.25 around the regional mean, suggesting elastic focussing/defocussing effects of this order are credible. Amplitude variations between azimuths average at a factor of 1.5 for the WWSSN stations. Random scattering probably increases the standard deviation of the relative amplitude measurements, but the effect of random scattering upon the mean relative amplitude is unknown at this time.

In transforming the variations of amplitude into variations of Q_a , only sediment amplification effects will be corrected. Part of the amplitude variations are probably due to scatter. In mapping the variation into attenuation, the resultant Q_a values must be considered to be effective or apparent Q_a . The fundamental direction is to obtain Q_a variations which are consistent with the observed amplitude variations. The standard errors of the mean relative amplitudes will be used to estimate the uncertainty of the effective Q_a at each station.

Geologic site information was listed in earlier and estimated sediment amplitude corrections where appropriate are listed in Appendix Table A22 for the WWSSN stations in the United States. Seven stations out of 29 required sediment corrections: BKS, LUB, DAL, FLO, OXF, AAM, SHA, and BEC. These amplitude corrections neither effect the highest amplitude station, RKON, nor the

lowest amplitude station, GOL

The greatest amplitude ratio in the data set is between RKON and GOL - ratios of 3.2 for the south-southeast, 5.2 for northwest azimuth. The amplitude value of RKON to north will be discussed in a moment. Following the previous section an amplitude ratio of 5.2 is equivalent to an energy ratio of 27. The energy loss of GOL relative to RKON may be related to Q_a if the number of cycles over which the energy loss occurred is estimated. As an assumption the size of the attenuation zone must be estimated. In this analysis it shall first be assumed that the attenuation variation takes place in the upper 300 km of the earth. This data set has little resolution of depth, and the 300 km range was chosen to be consistent with free oscillation Q models which have relatively higher Q below this depth (Anderson and Hart, 1978; Sailor and Dziewonski, 1978). The apparent lack of a distance trend in the body wave attenuation data between $30^\circ\Delta$ and $85^\circ\Delta$ further suggests attenuation occurs primarily in the upper mantle (e.g., Hart and Butler, 1977; Sengupta and Toksöz, 1977). The actual attenuation zone could occur over a narrower or broader depth range with a corresponding respective decrease or increase in the apparent effective Q_a . The basic data are the apparent energy losses, which are unaffected by our choice of where the attenuation occurs.

To define the starting estimate of Q_{AV} - the average Q_a for the United States - the geometric mean amplitude γ was calculated for each azimuth, excluding the sediment amplitude corrected stations above and also LON, BOZ, and RKON for reason of high azimuthal amplitude variability. The geometric mean γ was then divided into the observations in each azimuth. The resulting baseline is then nearly free of sediment amplitude correction uncertainties and instability due to the azimuthal highly varying stations. After this renormalization all stations were included in the further analysis.

Assuming the average Q_a of $Q_{AV} = 140$ for the renormalized baseline, the variation of effective Q_a for the seismic stations may be calculated from equation (24), using $n = 35$ cycles for northwest and south-southwest azimuth and $n = 34$ cycles for the northern azimuth. The effective values of Q_a model KMR1 for the WWSSN stations in the United States, derived under the restrictive assumptions mentioned, are listed in Table 13 for the three azimuths studied. The effective Q_a are computed from the mean relative amplitudes, and the ranges of effective Q_a are computed from the standard error of the mean relative amplitudes. Using the $Q_{AV} = 140$ yields a range of relative Q_a values which are finite and positive to within a standard error in the mean relative amplitude measure for all data except the unique observations to a northern azimuth for RKON and HNME. HNME has an effective $Q_a > 1000$ estimated from the high amplitude and from uncertainty of standard errors of the means at other stations. If Q_{AV} equals 150 or greater certain stations - RKON, HNME, DAL, COR - will show negative effective Q_a , implying relative amplification in relation to the energy loss differential available from attenuation over 34 to 35 cycles. Q_{AV} for

Table 13
 Q_a Model KMR1

Station	Northern Azimuth		Northwestern Azimuth		South-Southeastern Azimuth	
	Q_a	Range*	Q_a	Range*	Q_a	Range*
(west)						
BKS	168	132-215	157	126-198	125	113-139
COR	168	141-199	262	197-367	916	494-4100
LON	298	167-681	70	60-81	83	69-98
GSC	147	123-178	118	106-132	153	135-173
OB2NV	430	312-563	145	134-158	279	208-401
MSO	147	113-194	116	103-130	130	115-148
DUG	97	85-113	215	184-255	171	145-203
TUC	127	123-131	84	79-88	104	95-114
BOZ	451	324-596	239	193-302	68	54-83
ALQ	77	72-83	91	85-98	102	94-110
GOL	68	62-77	65	62-68	90	87-94
LUB	122	101-149	91	80-103	203	133-349
JCT	187	161-215	228	158-360	225	81-4600
DAL	950	533-1600	140	96-211	415	68-**
RKON	>1000	***	956	470-13500	999	385-**
ONF	122	108-140	209	160-285	195	89-677
SHA	161	125-210	99	84-116		
AAM	212	174-256	270	128-1170	89	65-118
ATL	111	100-125	201	170-270	143	120-173
BLA	145	105-207	346	254-513	180	132-257
SCP	327	188-702	153	131-179	112	106-117
CEO	463	262-1000	147	120-182	143	115-181
OGD	111	97-129	133	99-182	90	77-105
WES	88	75-105	250	202-319	104	101-107
HNME	>1000	****	165	139-197	198	162-246
(east)						

- * From standard error of the mean relative amplitudes
- ** Q_a slightly out of range of finite positive value, implying very high Q_a
- *** RKON has higher frequency content to the northern azimuth and extremely high amplitude, implying very high Q_a .
- **** Estimated from uncertainty of standard errors of the means at other stations

P waves may be less than 140, which represents an upper bound. As $Q_{AV} = 140$ for 1 sec P waves in the United States is already low in relation to free oscillation and surface wave Q models of the upper mantle, there seems to be little reason to chose a lower value.

The mean and range of Q_a for Q_a model KMR1 naturally follow the pattern of the amplitude data, with corrections included in Q_a model KMR1 for sediment amplification. The range of $65 < Q_a < 105$ is evident for all azimuths along the Rock Mountain front and Rio Grande Rift Zone at GOL and ALQ. Effective $Q_a > 950$ is consistent with the amplitude observations on the Canadian shield at RKON and to the north of Maine at HNME. The range $450 < Q_a \leq 950$ is observed for certain azimuths of DAL and COR. The range $250 < Q_a < 450$ is observed at certain azimuths of COR, LON, OB2NV, BOZ, DAL, FLO, AAM, BLA, SCP, GEO, and WES. At the low end stations with $Q_a < 100$ for certain azimuths include LON, BOZ, TUC, ALQ, GOL, LUB, AAM, OGD, and WES.

Tying LRSM Amplitudes to the WWSSN Array

Having mapped the variations of mean relative amplitudes into variations of effective Q_a for WWSSN stations, we now proceed to tie LRSM amplitude variations to the WWSSN array. Cleary's (1967) amplitude study of LRSM amplitudes, although not azimuthal in scope, analyzed more than fifty LRSM stations, published error bounds, and used a consistent amplitude measure of the P wave first motion. Eighteen out of twenty-two earthquakes measured by Cleary (1967) lay to azimuths northwest and south-southeast from the United States, indicating that the non-azimuthal Cleary (1967) LRSM amplitudes were influenced mostly from NW and SSE azimuths of approach. While 8 out of 26 WWSSN stations in the United States were situated on sediments, 30 out of 56 LRSM stations were situated on sediments. Geologic site information and estimated sediment amplitude corrections are listed in the Appendix in Table A23. The WWSSN

- SDCS stations RKON and HNME are located at sites previously occupied by LRSM instruments used by Cleary (1967). No other site locations are shared by the WWSSN and LRSM systems. However, the siting of LCNM at Las Cruces, New Mexico within the Rio Grande rift zone is similar to the site of ALQ, Albuquerque, New Mexico. In tying the LRSM to the WWSSN-SDCS array, the relative amplitude triangle RKON-HNME-LCNM is matched to RKON-HNME-ALQ. Three amplitude ratios are formed combining the three stations two at a time. For Cleary (1967) the amplitude ratios are: $RKON/LCNM = 2.95$, $RKON/HNME = 1.74$, and $HNME/LCNM = 170$. For the WWSSN-SDCS amplitudes presented herein, the northwest and south-southeast azimuths are used [NW, SSE]: $RKON/ALQ = [3.11, 2.74]$, $RKON/HNME = [1.76, 1.57]$, and $HNME/ALQ = [1.77, 1.74]$. Thus the relative amplitudes of the LRSM stations RKON-HNME-LCNM form a similar triangle with relative amplitudes of the WWSSN-SDCS stations, RKON-HNME-ALQ. To obtain the best least-squares amplitude match for RKON-HNME-LCNM from Cleary (1967) to RKON-HNME-ALQ amplitudes presented here, a constant log amplitude of (+ 0.01) was added to each log amplitude determination of Cleary (1967). This procedure yields mean relative amplitudes of RKON 2.00, HNME 1.15, and LCNM 0.68 for Cleary's (1967) LRSM stations which compare favorably with northwest and south-southeast [NW, SSE] azimuthal determinations for the present study: RKON [1.99, 2.00], HNME [1.13, 1.27], and ALQ [0.64, 0.73]. This shows that log amplitudes of Cleary (1967) with a small baseline shift of (+ 0.01) are compatible with relative amplitudes determined for the WWSSN array. From the Cleary (1967) study, 56 LRSM stations were tied to the WWSSN-SDCS baseline. While the amplitude measurements in Evernden and Clark (1970) and Booth et. al. (1974) were not limited to the first cycle of P wave motion, the measurements present amplitude variations at a period $T \sim 1$ sec. To obtain an amplitude estimate for Q_0 at LRSM stations not covered by Cleary (1967), the

station amplitude anomalies from Evernden and Clark (1970) and Booth et. al. (1974) were tied to the Cleary (1967) study through common stations. Sediment corrections are estimated from Tables 11 and 12 where necessary. Appendix Tables A24 and A25 list amplitude and Q_a data for LRSM stations in the studies of Evernden and Clark (1970) and Booth et. al. (1974), respectively, for stations not covered in the study of Cleary (1967).

Effective Q_a for the LRSM Array

Applying the small (+ 0.01) baseline shift to the Cleary (1967) log amplitudes and correcting the amplitudes of stations situated on low velocity sediments, the LRSM log amplitudes are transformed by exponentiation (10^x) to amplitude and then into effective Q_a . Table 14 lists the mean and range of effective Q_a for the LRSM stations of Cleary (1967), where the range is derived from the standard error of the station mean amplitude. As in the case of the earthquake sources for the WWSSN data, equation (24) was used assuming $n = 35$ cycles and $Q_{AV} = 140$. The mean Q_a for the LRSM stations range from a maximum 978 at RKON to a low of 64 for CKBC, Cache Creek, British Columbia. Stations with high amplitudes having apparent effective $Q_a \geq 200$ are: BDPA, Bedford, Pennsylvania; FSAZ, Flagstaff, Arizona; HHND, North Dakota; WNSD, South Dakota; PFMI, Pickford, Michigan upper peninsula; RKON, Red Lake, Ontario and RYND, Ryan, North Dakota. With exception to FSAZ the highest Q_a stations lie in the north for the LRSM data set. Stations with low amplitude and apparent effective $Q_a \leq 100$ are: CKBC, Cache Creek, British Columbia; CPCL, Campo, California; CVTN, Centerville, Tennessee; GDVA, Grundy, Virginia; GONB, Nebraska; KGAZ, Kingman, Arizona; MPAR, Mount, Arkansas; MVCL, Marysville, California; TFCL, Taft, California; WINV, Winnemucca, Nevada, and WTTN, Wartburg, Tennessee.

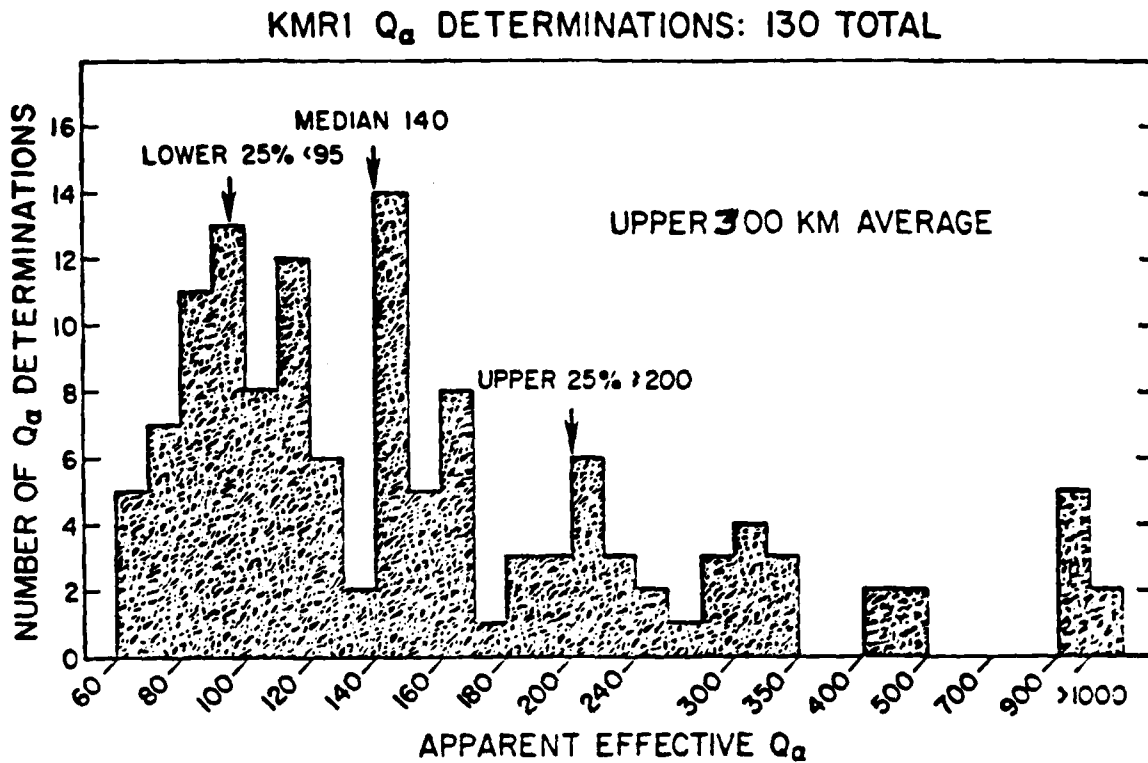


Figure 15. A histogram of 130 determinations of Q_a in the United States and southern Canada shows the distribution Q_a for Q_a model KMRI. The Q_a represent average values over 34 to 35 cycles of vibration in the upper 300 km of the earth. The median is $Q_a = 140$, while 25% of the Q_a are less than 95 and 25% are greater than 200.

Results for Q_a

A summary histogram of Tables 13 and 14 shows in Figure 15 the distribution of Q_a determinations for the United States and southern Canada, where numbers of observations are grouped versus Q_a values. The median Q_a is 140 for the 130 determinations of Q_a from Q_a model KMR1 using the amplitude data from Cleary (1967) and here. This median Q_a of 140 equals the starting value $Q_{av} = 140$ chosen for WWSSN stations. The equality of the median Q_a with the starting $Q_{av} = 140$ indicates that the sediment amplitude correction is a proper procedure and that the Q_a for sedimentary sites are not biased with respect to hard bedrock sites. Note also in Figure 15 that 25% of the determinations are $Q_a \geq 200$ and 25% have $Q_a < 95$.

The apparent effective q_a determinations of Q model KMR1 are plotted in

Figure 16. The WWSSN and SDCS stations are marked by solid dots at the station location - see Figure 1 for comparisons. Three Q_a determinations are (usually) plotted around the site in relation to the three azimuths of approach in the study - N, NW, and SSE. The LRSM stations of Cleary (1967) are marked by open circles, with a single Q_a plotted with the station location. Estimated Q_a from the studies of Evernden and Clark (1970) and Booth et.al. (1974) are plotted with an "X" in Figure 16. The effective Q_a are plotted with the station name code. The data plotted are the mean values from Tables 13 and 14 and from Appendix Tables A24 and A25. In the KMR1 Q_a model the amplitude variations are mapped into energy losses in the upper 300 km of the earth through attenuation over 34 to 35 cycles of vibration. The effective Q_a in Figure 16 are replotted as symbols in Figure 17 divided among the 4 quartiles of Figure 15: low $Q_a < 95$; low-intermediate $Q_a < 140$; intermediate-high $Q_a \geq 140$; and high $Q_a \geq 200$. Q_a values below 140 are surrounded by stippling to draw the low Q_a areas together. The symbol area in Figure 17 represents roughly the lateral distance the seismic ray travels in the upper 220 km of the earth. From a depth of 600 km a P wave travels a lateral distance of about 385 km when arriving from an event $60^\circ\Delta$ distant. The Q_a values are average values over some lateral distance.

The west coast of the United States shows the full range of effective Q_a . Some very low Q_a are seen in California in the Imperial Valley, Taft, and Marysville. The Great Basin has both high apparent Q_a at OB2NV in the Nevada Test Site and northwest of DUG, near Provo, Utah and low Q_a at WINV, Winnemucca and MNNV, Mina, Nevada. WINV, Winnemucca, Nevada is near the Battle Mountain heat flow high. High Q_a is seen near COR, Corvallis, Oregon and north of LON, Longmire, Washington. Low Q_a extends northwest and south-southeast of LON, across the Columbia Plateau and eastern Snake River plain to Yellowstone.

Table 14

Q_0 Model KMR1

Station	Q_0	Range*	Station	Q_0	Range*
ARWS	133	108-172	KGAZ	84	69-108
ATNV	144	104-235	KNUT	90	83-99
AYSD	90	77-109	LCNM	95	85-104
BDPA	324	170-4255	MMTN	101	91-113
BFCL	140	102-224	MNNV	93	85-102
BLWV	83	77-90	MPAR	72	68-78
BUQB	117	98-147	MVCL	72	68-77
CKBC	64	55-77	MZAR	110	85-145
CPCL	89	82-96	NDCL	114	85-154
CTOK	112	92-143	NGWS	110	95-130
CVTN	66	59-75	NPNT	169	114-330
DHNY	140	123-163	PFMJ	347	193-1789
DRCO	82	76-88	PMWY	90	83-98
EYNV	110	85-154	PTOR	99	90-110
FMUT	123	109-140	RKCN	978	299-***
FRMA	148	111-223	RTNM	93	75-125
FSAZ	212	171-279	RYND	347	176-40,000
GDVA	83	73-96	SEMN	144	125-169
GIMA	163	113-299	SJTX	93	84-105
GONB	86	72-105	SSTX	105	94-119
GVTX	136	120-158	STNV	148	105-253
HBOX	110	99-123	TFCL	70	65-75
HEND	324	170-4255	TKWA	101	79-139
HKWY	168	122-273	TUPA	129	105-167
HLID	103	9-112	WINV	78	73-84
HMBC	168	122-273	WNSD	189	157-233
HNME	168	142-208	WTTN	76	63-95
HTMN	195	135-352	WWUT	101	60-137
***			MDS[N]	235	194-291
BEC[N]	66	54-79	RCD[N]	162	137-194
FLO[N]	100	85-118	FLO[NW]	321	258-420
GHD[N]	55	42-68	FLO[SSD]	289	235-352

*From standard error of mean relative amplitudes

** Q_0 slightly out of range of positive finite value, implying very high Q_0

***The following WSSN stations from Butler and Ruff (1960) have [] as mutual Q_0 determinations.

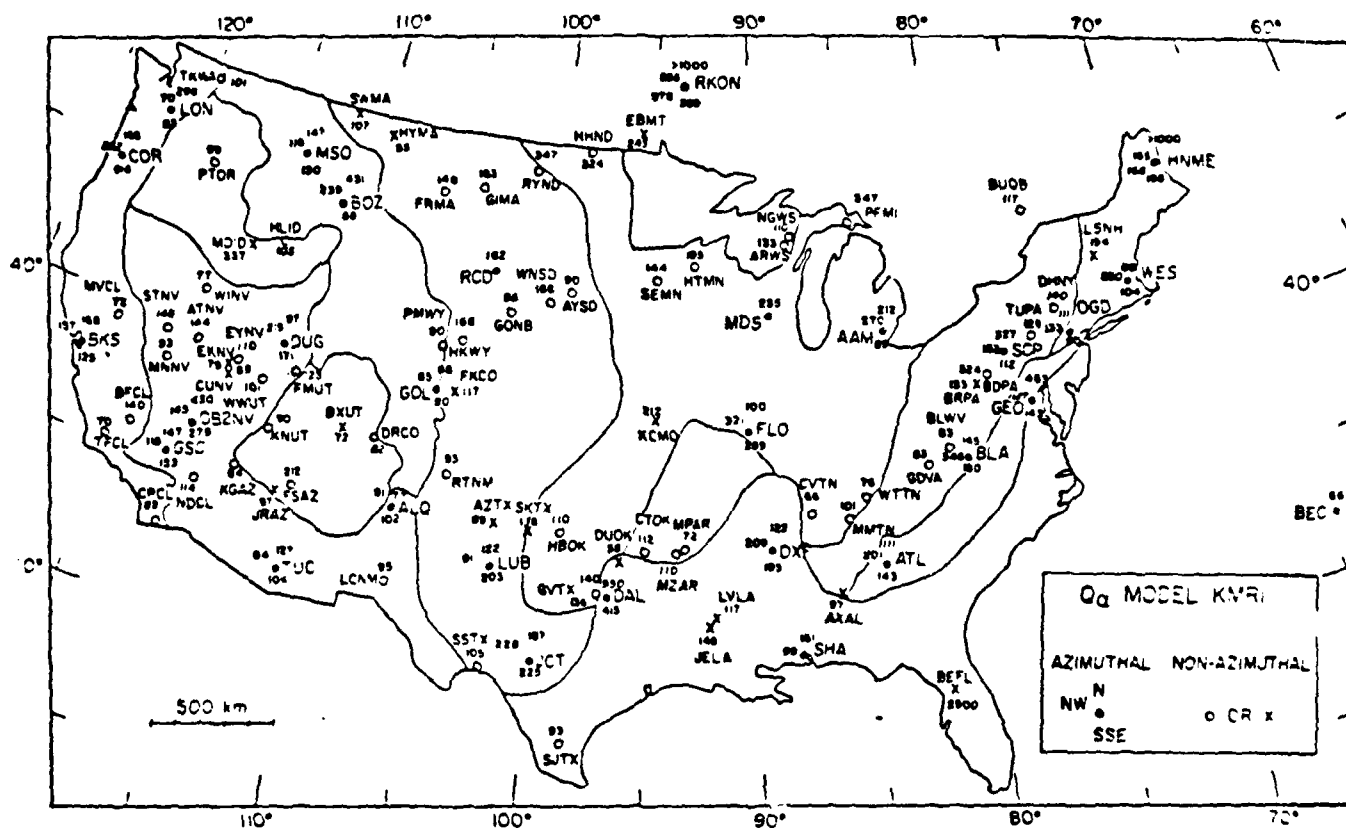


Figure 16. Determinations of Q_α for WSSN and LRSM seismic stations are plotted in relation to physiographic provinces. Q_α model KVR1 maps amplitude variations into apparent Q_α representing energy losses in the upper 300 km of the earth. Azimuthal Q_α determinations at stations with solid dots are plotted in relation to azimuth from the station. The Q_α values are determined in relation to an average $Q_\alpha = 140$.

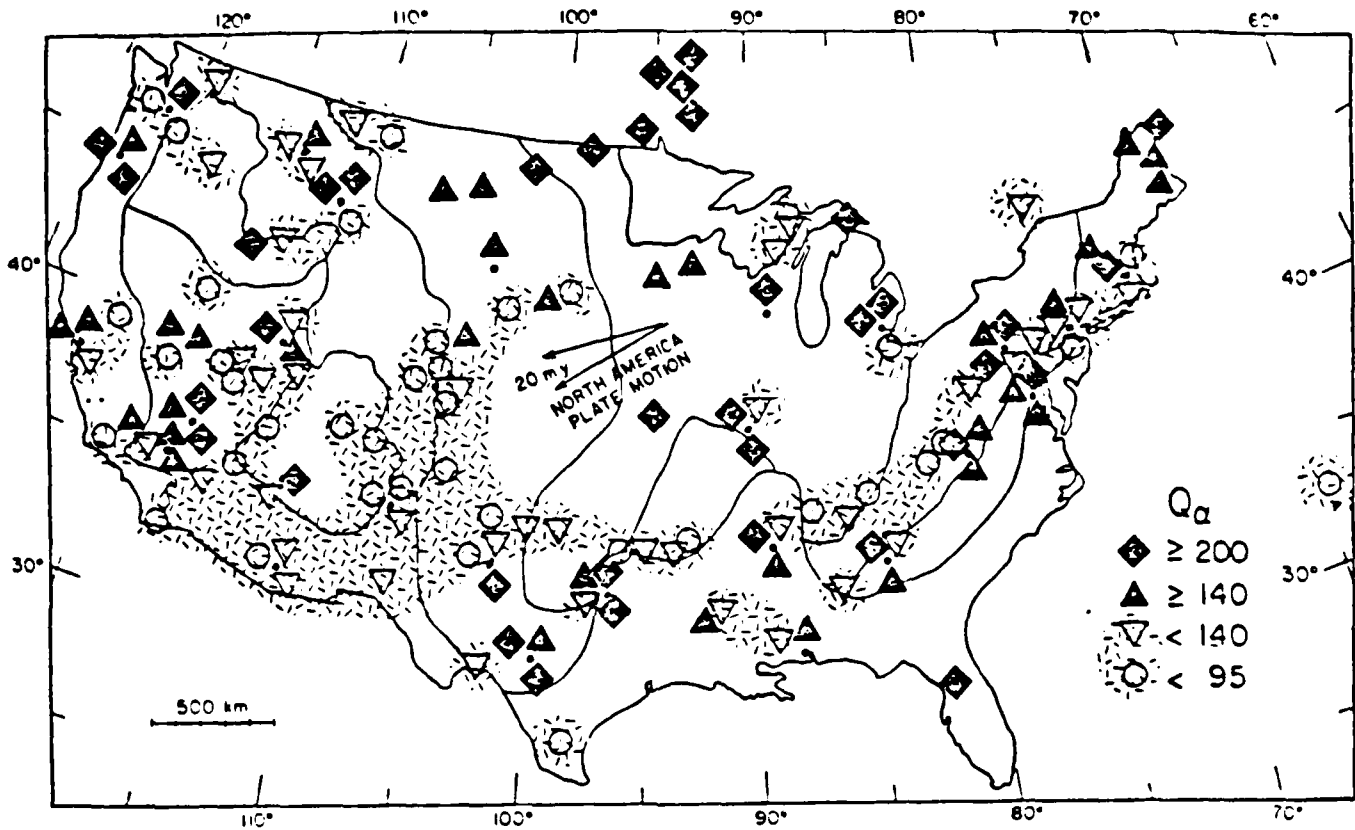


Figure 17. The variation of Q_α is shown with four symbols representing ranges of Q_α . Lower Q_α areas are stippled and lower Q_α values are plotted as triangles or circles. Higher Q_α values are plotted as solid triangles or diamonds. The motion of the North American plate for 20 m.y. is shown relative to the underlying mantle, the two arrows indicating the uncertainty of direction.

While no data are available for the central Rockies, low Q_a are evident along the Rocky Mountain front, the Rio Grande Rift, the Great Plains north of LUB, Lubbock, Texas, and in the southern basin and range at TUC, Tucson, Arizona. With the exception of FSAZ, Flagstaff, Arizona the edges of the Colorado plateau are characterized by low Q_a .

The central United States and Canada has among the highest effective Q_a at RKON, Red Lake, Ontario and DAL, Dallas, Texas. The northern Great Plains has a trend of intermediate high Q_a in eastern Montana increasing eastward to high Q_a in North Dakota and the highest Q_a at RKON on the Canadian shield. Intermediate Q_a occur across Nebraska, South Dakota, Minnesota, and Wisconsin. The Ozark plateau shows high Q_a to the northeast and low Q_a to the south. The low Q_a at MPAR, Mountain Pine, Arkansas lies very near to the hot springs of Arkansas. Intermediate to high Q_a are found in central Texas, with a low Q_a in south Texas at SJTX, San Jose.

The United States east of the Mississippi River displays a range of high to low apparent effective Q_a observed in the central and western United States. High to intermediate-low Q_a are seen at SHA, Spring Hill, Alabama along the Gulf coast and in Mississippi embayment at QXF, Oxford, Mississippi. High Q_a is found from south of AAM, Ann Arbor, Michigan, then east to BLWV, Beckley, West Virginia and GDVA, Grundy, Virginia, extending through Tennessee to northeastern Mississippi and bounded to the west at FLO, Florissant, Missouri near Saint Louis. Although the connection between these low Q_a stations may be more apparent than real, the individual low amplitudes are well determined. Intermediate and high Q_a occur in the eastern Appalachias and the Piedmont. The high apparent Q_a raypath northwest of BLA, Blacksburg, Virginia passes beneath the low amplitude station BLWV, Beckley, West Virginia at a depth of nearly 200 km. Intermediate and low Q_a are observed in southern New England.

High and intermediate-high effective Q_a are seen at HNME, Houlton, Maine and to the northwest of WES, Weston, Massachusetts near Boston. An intermediate-low apparent Q_a is found for BUQB, Buckingham, Quebec on the Grenville province of the Canadian shield. A low Q_a is observed at Bermuda in the Atlantic Ocean east of the United States.

The variation of the mean Q in the upper 300 km of the mantle within the continental U.S. can also be represented in the form of a contour map of Q_a . Of course, the station coverage of the U. S. is such that several areas are not well sampled, however, if the azimuthal variation of Q_a at the WWSSN stations is taken into account, the inference of the Q_a variation is somewhat more constrained. In any case, Figure 18 shows Q_a contours based on all the data, including the azimuth variations estimated at the WWSSN stations (black dots). While there are uncertainties in this representation, it nevertheless provides a useful summary diagram incorporating all the known results.

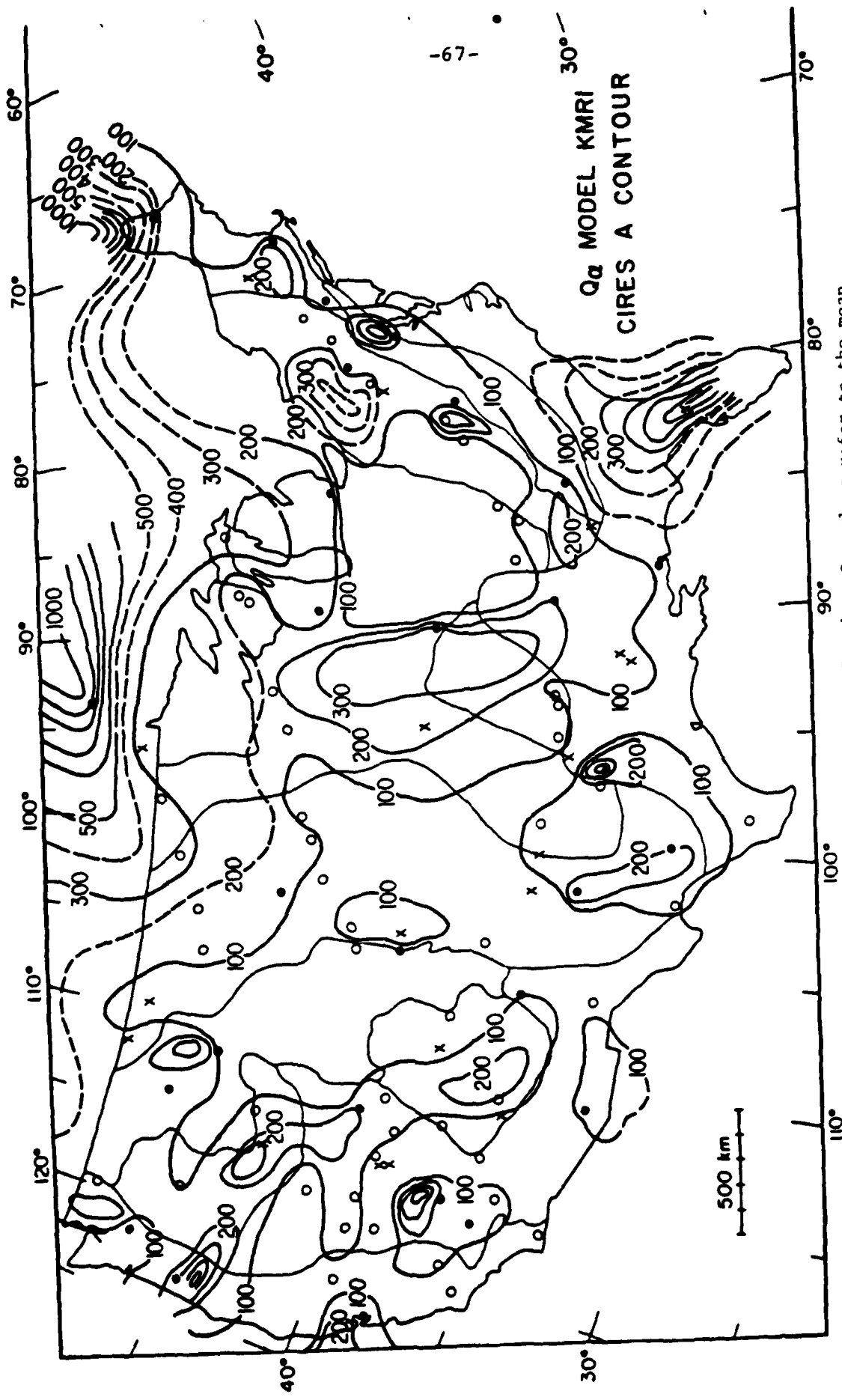


Figure 18. Q_α contour map for the Continental U. S. and So. Canada. Q_α values refer to the mean Q_α in the upper 300 km beneath the continent.

References

- Aki, K. (1973). Scattering of P-waves under Montana LASA, *J. Geophys. Res.*, **78**, 1334-1346.
- Aki, K., A. Christoffersson, and E. S. Husebye (1977). Determination of the three-dimensional seismic structure of the lithosphere, *J. Geophys. Res.*, **82**, 277-296.
- Anderson, D. L. (1967). The anelasticity of the mantle, *Geophys. J. R. Astr. Soc.*, **14**, 135-164.
- Anderson, D. L. and C. B. Archambeau (1964). The anelasticity of the earth, *J. Geophys. Res.*, **69**, 2071-2084.
- Anderson, D. L., A. Ben-Menahem, and C. B. Archambeau (1965). Attenuation of seismic energy in the upper mantle, *J. Geophys. Res.*, **83**, 58.
- Anderson, D.L. and R.S. Hart (1978a). Attenuation models of the earth, *Phys. of Earth and Planet. Interiors*, **16**, 289-306.
- Anderson, D.L. and R.S. Hart (1978b). Q of the earth, *J. Geophys. Res.*, **83**, B12, 5869-5882.
- Anderson, D. L. and J. W. Given (1982). Absorption band Q model for the earth, *J. Geophys. Res.*, **87**, 3893-3904.
- Archambeau, C. B., E. A. Flinn, and D. G. Lambert (1969). Fine structure of the upper mantle, *J. Geophys. Res.*, **74**, 5825.
- Archambeau, C. and C. Sammis (1970). Seismic radiation from explosions in prestressed media and the measurement of tectonic stress in the earth, *Rev. Geophys. Space Phys.*, **8**, 473.
- Armstrong, R.L., W.B. Leeman, and H.E. Malde (1975). K-AR dating, quaternary and neogene volcanic rocks of the snake river plain, Idaho, *Amer. J. Sci.*

275, 225-251.

Bachc, T. C., T. R. Blake, J. T. Cherry, T. G. Barker, P. G. Lambert, S. M. Savino and N. Rimer (1975). An explanation of the relative amplitudes of the teleseismic body waves generated by explosions in different test areas of NTS, *SSS-R-76-1746; DNA 3958F*.

Bakun, W. H. (1971). Crustal model parameters from P-wave spectra, *Bull. Seism. Soc. Amer.*, 61, 913-935.

Bath, M. (1969). Handbook on earthquake magnitude determinations, *VESIAC Special Report Sec. Edition*, 7895-36-X, Seismological Institute, Uppsala.

Berteussen, K. A. (1974). NORSAR location calibrations and time delay corrections, *Sci Rep. 2-73/74 NTN/NORSAR*, Kjeller, Norway.

Berteussen, K. A. (1975). P wave amplitude variability at NORSAR, *J. Geophys.* 41, 595-613.

Berteussen, K. A. (1977). Moho depth determinations based on spectral ratio analysis of NORSAR long period P-waves, *Phys. Earth Planet. Int.*, 15, 13-27.

Berteussen, K. A. and E. S. Husebye (1972). Predicted and observed seismic event detectability of the NORSAR array, *NORSAR Tech Rept. no 42 NTN/NORSAR*.

Berteussen, K. A. and E. S. Husebye (1974). Amplitude pattern effects on NORSAR P-wave detectability, *Scientific Report 1-74/75, NTN/NORSAR*, N-2007 Kjeller, Norway.

Berteussen, K. A., A. Christofferson, E. S. Husebye, and A. Dahle (1975). Wave scattering theory in analysis of P-wave anomalies at NORSAR and LASA, *Geophys J R Astr. Soc.* 42, 403-417.

Best, W. J., L. R. Johnson and T. V. McEvilly (1974). ScS and the mantle beneath

- Hawaii, Abstract EOS Trans. Am. Geophys. Un. 56, 1147.
- Bock, G. and J. R. Clements (1982). Attenuation of short-period P, PcP, ScP, and PP waves in the earth's mantle, *J. Geophys. Res.*, 87, 3905-3915.
- Booth, D. C., P. D. Marshall and J. B. Young (1974). Long and short period P-wave amplitudes from earthquakes in the range $0^\circ - 114^\circ$, *Geophys. J. R. Astr. Soc.*, 39, 523-537.
- Borcherdt, R. D. (1970). Effects of local geology on ground motion near San Francisco Bay, *Bull. Seism. Soc. Am.*, 60, 29-61.
- Bullen, K.E. (1965). *An Introduction to the Theory of Seismology*. Third edition, Cambridge Press.
- Bungum, H., E. S. Husebye, and F. Ringdal (1971). The NORSAR array and preliminary results of data analysis, *Geophys. J.*, 25, 115-126.
- Bungum, H. and E. S. Husebye (1974). Analysis of the operational capabilities for detection and location of seismic events at NORSAR, *Bull. Seism. Soc. Am.*, 64, 637-656.
- Burdick, L. J. (1978). t^* for S waves with a continental ray path, *Bull. Seism. Soc. Amer.*, 68, 1013-1030.
- Burdick, L. J. and G. R. Mellman (1976). Inversion of the body waves from the Borrego Mountain earthquakes to the source mechanism, *Bull. Seism. Soc. Am.*, 66, 1485-1499.
- Burdick, L.J. and Helmberger, D.V. (1978). The upper mantle P-velocity structure of the western United States, *J. Geophys. Res.*, 83, 1699-1712.
- Burdick, L. J. and C. A. Langston (1977). Modeling crustal structure through the use of converted phases in teleseismic body wave forms, *Bull. Seism. Soc. Am.*, 65, 55-70.
- Burridge, R. (1963). The reflection of a pulse in a solid sphere, *Proc. Roy. Soc.*

Ser A 176, 367-400.

Butler, R. (1977). Lateral variation of P wave amplitudes from bombs: A case for variation in T^* , *EOS Trans.*, vol 58, no 12, 1183.

Butler, R. (1979a). *Seismological studies using observed and synthetic waveforms* (Doctoral Dissertation), Calif. Inst. of Technology, Pasadena, California.

Butler, R. (1979b). Variation of short period P wave amplitudes in the United States, *EOS Trans. Vol 60, no. 46*, 880-881.

Butler, R. (1979c). Shear wave travel times from SS, *Bull. Seism. Soc. Am.*, 69, 1715-1732.

Butler, R., and R.S. Hart (1979). *Summary of current research on seismic wave form analysis of underground nuclear explosions*, Technical Report SG1-R-79-004, Sierra Geophysics, Inc. Arcadium CA 91106.

Butler, R., L. J. Ruff, R. S. Hart, G. R. Mellman (1979). Seismic waveform analysis of underground nuclear explosions, Sierra Geophysics Technical Report SG1-R-79-011, Sierra Geophysics, Inc., 150 N. Santa Anita Ave., Arcadia, California 91006.

Butler, R. and L. Ruff (1980). Teleseismic short-period amplitudes: source and receiver variations, *Bull. Seism. Soc. Am.*, 70, 831-850.

Capon, J., R. J. Greenfield, R. J. Kolker and R. T. Lacoss (1968). Short-period signal processing results for the large aperture seismic array, *Geophysics*, 33, 452-472.

Capon, J. (1974). Characteristics of crust and upper mantle structure under Iasa as a random medium, *Bull. Seism. Soc. Amer.*, 25, 115-126.

Carpenter, E. W. (1967). Teleseismic signals calculated for underground, underwater and atmospheric explosions, *Geophys. J.*, 32, 17-32.

- Carpenter, E. W. and E. A. Flinn (1965). Attenuation of teleseismic body waves, *Nature*, 207 745-746.
- Carpenter, E. W., P. D. Marshall and A. Douglas (1967). The amplitude distance curve for short period teleseismic P-waves, *Geophys. J. Roy. Astr. Soc.*, 13, 61-70.
- Chang, A. C. and D. H. von Seggern (1980). A study of amplitude anomaly and m_b bias at LASA subarrays, *J. Geophys. Res.*, 85, 4811-4828.
- Chernov, L. (1960). *Wave Propagation in Random Medium*, McGraw-Hill, New York.
- Choy, G. L., and P. G. Richards (1975). Pulse distortion and Hilbert transformation in multiply reflected and refracted body waves, *Bull. Seism. Soc. Am.*, 65, 55-70.
- Christiansen, R. L. and P. W. Lipman (1972). Cenozoic volcanism and plate-tectonic evolution of the western United States, II. Late Cenozoic, *Phil. Trans. R. Soc. Lond. A* 271, 249-284.
- Cleary, J. (1967). Analysis of the amplitudes of short period P-waves recorded by long range seismic measurements stations in the distance range $30^\circ - 102^\circ$, *J. Geophys. Res.*, 72, 4705-4712.
- Cleary, J. and A. Hales (1966). An analysis of the travel times of P waves to north American stations in the distance range $32^\circ - 100^\circ$, *Bull. Seism. Soc. Amer.*, 56, 467-489.
- Clements, J. (1982). Intrinsic Q and its frequency dependence, *Phys. Earth and Planet. Inter.*, 27, 286-299.
- Davies, D. and B.R. Julian (1972). A study of short period P wave signals from Longshot, *Geophys. J. Roy. Astr. Soc.*, 29, 185-202.
- Der, Z. A., R. P. Masse, and J. P. Gurski (1975). Regional attenuation of short-

- period P and S waves in the United States, *Geophys J R Astr Soc.*, 40, 85-106.
- Der, Z. A. and T. W. McElfresh (1976). Short period P-wave attenuation along various paths in N. America as determined from P wave spectra of the Salmon Nuclear explosion, *Bull. Seism. Soc. Amer.*, 66, 1609-1622.
- Der, Z. A., T. W. McElfresh and A. O'Donnell (1982). An investigation of the regional variations and frequency dependence of anelastic attenuation in the mantle under the United States in the 0.5-4 Hz band, *Geophys. J. R. Astr. Soc.*, 69, 67-99.
- Der, Z. A., E. Smart, and A. Chaplin (1980). Short-period S-wave attenuation under the United States, *Bull. Seism. Soc. Am.*, 70, 101-125.
- Diment, W. H., T. C. Urban, J. H. Sass, B. V. Marshall, R. J. Munroe, and A. E. Lachenbruch (1975). Temperatures and heat contents based on conductive transport of heat, *Assessment of Geothermal Resources of the United States - 1975*, U. S. Geol. Surv. Cir. 726, p. 84-103.
- Douglas, A., J. B. Young, and P. D. Marshall (1981). Some analyses of P- and Rayleigh wave amplitudes observed at North American stations, *Geophys J R Astr. Soc.*, 67, 305-324.
- Dziwonski, A. and D.L. Anderson (1981). Preliminary reference earth model, *Phys. Earth Planet. Inter.*, 25, 297-356.
- Evernden, J. F. (1967). Magnitude determination at regional and near-regional distances in the United States, *Bull. Seism. Soc. Amer.*, 57, 591-639.
- Evernden, J. and D. M. Clark (1970). Study of teleseismic P. I. Travel-time data, *Phys. Earth Planet. Int.*, 4, 1-23.
- Evernden, J. F. and D. M. Clark (1970). Study of teleseismic P. II Amplitude data, *Phys. Earth Planet. Int.*, 4, 24-31.

- Ewing, W.M., W.S. Jardetzky, and F. Press (1957). *Elastic waves in layered media*, Int. Series Earth Sci., McGraw-Hill.
- Faust, L. Y. (1950). Seismic velocity as a function of depth and geologic time, *Geophys.*, 16, 192-206.
- Frasier, C. W. and J. Filson (1972). A direct measurement of the earth's short period attenuation along a teleseismic ray path, *J. Geophys. Res.*, 72, 3782-3787.
- Futterman, W. I. (1962). Dispersive body waves, *J. Geophys. Res.*, 67, 5279.
- Girardin, N. (1980). Travel-time residuals of PP waves reflected under oceanic and continental platform regions, *Phys. Earth Planet. Int.*, 23, 199-206.
- Greenfield, R.J. and R.M. Sheppard (1969). The Moho depth variations under Iasa and their effect on DT/D Δ measurements, *Bull. Seism. Soc. Amer.*, 59, 409-420.
- Gutenberg, B. (1956). Effects of ground on shaking in earthquakes, *Transactions, AGU*, 37, 757-760.
- Gutenberg, B. (1957). Effects of ground on earthquake motion, *Bull. Seism. Soc. Am.*, 47, 221-250.
- Haddon, R. A. and E. S. Husebye (1978). Joint interpretation of P-wave time and amplitude anomalies in terms of lithospheric heterogeneities, *Geophys. J. R. Astr. Soc.*, 55, 19-43.
- Hart, R. S. and R. Butler (1978). Shear-wave travel times and amplitudes for two well constrained earthquakes, *Bull. Seism. Soc. Am.*, 68, 973-985.
- Hart, R. S., D. M. Hadley, G. R. Mellman, and R. G. Butler (1979). Seismic amplitude and waveform research, *Technical Report SGI-R-79-012*, Sierra Geophysics, 150 N. Santa Anita Ave., Arcadia, CA 91006.
- Helmberger, D. V. and D. M. Hadley (1981). Seismic source functions and

- attenuation from local and teleseismic observations of the NTS events JORUM and HANDLEY, *Bull. Seism. Soc. Amer.*, 71, 51-67.
- Herrin, E. and J. Taggart (1962). Regional variations in P_n velocity and their effect on the location of epicenters, *Bull. Seism. Soc. Amer.*, 52, 1037-1046.
- Herrin, E. (1969). Regional variations of P-wave velocity in the mantle beneath North America, in *The Earth's Crust and Upper Mantle*, edited by P.J. Hart, p. 242, American Geophysical Union Monograph 13, Washington, D.C.
- Hong, Tai-lin, and D. Helmberger (1978). Glorified optics and wave propagation in non planer structure, *Bull. Seism. Soc. Am.*, 68, 1313-1330.
- Hunt, Charles B. (1956). Cenozoic geology of the Colorado Plateau, *U. S. Geological Survey Professional Paper 279*.
- Husebye, E. S., A. Dahle, and K. A. Berteussen (1974). Bias analysis of NORSAR and ISC reported seismic event m_b magnitudes, *J. Geophys. Res.*, 79, 2967-2978.
- Iyer, H. M. (1971). Variation of apparent velocity of teleseismic P waves across the Large Aperture Seismic Array, Montana, *J. Geophys. Res.*, 76, 8554-8567.
- Jackson, D. (1969). *Grain Boundary Relaxation and the Attenuation of Seismic Waves*, (Ph.D. thesis), MIT, Cambridge, Massachusetts.
- Jeffreys, H. and K.E. Bullen (1958). *Seismological Tables*, Brit. Assoc. Adv. of Sci., Gray-Milne Trust, London, 55 pp.
- Jeffreys, H. and E.R. Lapwood (1957). The reflection of a pulse within sphere, *Proc. Roy. Soc. (London)*, Ser. A, 241, 455-479.
- Jeffreys (1970). *The Earth*, 5th edition, Cambridge Press.
- Jordan, J., R. Black, and C. C. Bates (1965). Patterns of maximum amplitudes of P_n and P waves over regional and continental areas, *Bull. Seism. Soc.*

- Amer.*, 55, 693-720.
- Jordan, T. H. and W. S. Lynn (1974). A velocity anomaly in the lower mantle, *J. Geophys. Res.*, 79, 2679-2685.
- Jordan, T. H. and S. A. Sipkin (1977). Estimation of the attenuation operator for multiple ScS waves, *Geophys. Res. Letters*, 4, 167-170.
- Kanamori, H. (1967a). Spectrum of P and PcP in relation to the mantle-core boundary and attenuation in the mantle, *J. Geophys. Res.*, 72, 559-571.
- Kanamori, H. (1967b). Spectrum of short-period core phases in relation to the attenuation of the mantle, *J. Geophys. Res.*, 72, 2181-2186.
- Kanamori, H. (1970). Velocity and Q of mantle waves, *Phys. Earth Planet. Inter.*, 2, 259-275.
- Keller, G. R., L. W. Braille, and J. W. Schlue (1979). Regional crustal structure of the Rio Grande Rift from surface wave dispersion measurements, in *Rio Grande Rift: Tectonics and Magmatism*, editor: Reicker, R. E., Am. Geophys. Un., p. 115-125.
- Kohlstedt, D. L. and G. Goetze (1974). Low-stress high-temperature creep in olivine single crystals, *J. Geophys. Res.*, 79, 2045-2051.
- Kohlstedt, D.L., H.P.K. Nichols and P. Hornack (1980). The effect of pressure on the rate of dislocation recovery in olivine, *J. Geophys. Res.*, 85, 3122-3130.
- Kovach, R.L. and D.L. Anderson (1964). Attenuation of shear waves in the upper and lower mantle, *Bull. Seism. Soc. Amer.*, 54, 6, 1855-1864.
- Kron, A. and G. Heiken (1980). Geothermal Gradient Map of the Conterminous United States, Los Alamos Scientific Laboratory publication, #LA-8476-MAP.
- Kurita, T. (1973). Regional variations in the structure of the crust in the central U. S. from P-wave spectra, *Bull. Seism. Soc. Amer.*, 63, 1663-1667.

- Kurita, T. (1974). Upper mantle structure in the central United States from P and S wave spectras, *Phys. Earth Planet. Int.*, **8**, 177-201.
- Kurita, T. (1976). Crustal and upper mantle structure in the central U.S. of A. from body wave spectra, surface-wave dispersion, travel time residuals and synthetic seismograms, *Phys. Earth Planet. Int.*, **12**, 65-86.
- Langel, R. A. and C. C. Schnetzler (1982). Initial vector magnetic anomaly map from Massat, *Geophys. Res. Letters*, **9**, 273-276.
- Langel, R. A., J. D. Phillips, and R. J. Horner (1982). Initial scaler magnetic anomaly map from Massat, *Geophys. Res. Letters*, **9**, 269-272.
- Langston, C. A. (1977). The effect of planar dipping structure on source and receiver responses for constant ray parameter, *Bull. Seism. Soc. Am.*, **67**, 1029-1050.
- Langston, C. A. (1979). Structure under Mount Rainier, Washington, inferred from teleseismic body waves, *J. Geophys. Res.*, **84**, 4749-4762.
- Langston, C. A. (1981). Evidence for the subducting lithosphere under southern Vancouver Island and western Oregon from teleseismic P waved conversions, *J. Geophys. Res.*, **86**, 3857-3866.
- Lay, T. and D. V. Helmberger (1981). Body wave amplitude patterns and upper mantle attenuation variations across North America, *Geophys. J. R. Astr. Soc.*, **66**, 691-726.
- Lee, W. B. and S. C. Solomon (1978). Simultaneous inversion of surface wave phase velocity and attenuation: Love waves in western North America, *J. Geophys. Res.*, **83**, 3389-3400.
- Lerch, F.J., B.H. Putney, C.A. Wagner and S.M. Klosko (1981). Goddard Earth models for oceanographic applications (CEM 10B and 10C), *Marine Geodesy*, **5**, 145-187.

- Lipman, P. W., H. J. Prostka, and R. L. Christiansen, Cenozoic volcanism and plate-tectonic evolution of the western United States. I. Early and Middle Cenozoic, *Phil. Trans. R. Soc. Lond. A* 271, 217-248.
- Lundquist, G. (1979). *The Frequency Dependence of Q*, Doctoral Dissertation, Univ. of Colorado, Boulder, Colorado.
- Lundquist, G.M. and V.C. Cormier (1980). Constraints on the absorption band model of Q, *J. Geophys. Res.*, 85, 5244-5256.
- Mack, H. (1969). Nature of short-period P-wave signal variation at LASA, *J. Geophys. Res.*, 74, 3161-3170.
- Marshall, P.D. and D.L. Springer (1976). Is the velocity of P_n an indicator of Q_n , *Nature*, 264, 531-533.
- Marshall, P.D., D.L. Springer and H.C. Rodean (1979). Magnitude corrections for attenuation in the upper mantle. *Geophys. J. R. astr. Soc.*, 57, 609-638.
- Mayhew, M. A., H. H. Thomas and P. J. Wasilewski, Satellite and surface geophysical expression of anomalous crustal structure in Kentucky and Tennessee, *Earth Planet. Sci. Letters*, 58, 395-405.
- McGinley, J.R. and D.L. Anderson (1969). Relative amplitudes of P and S waves as a mantle reconnaissance tool, *Bull. Seism. Soc. Am.*, 59, 1189-1200.
- Mellman, G. R. and R. S. Hart (1980). Review of magnitude/yield estimation, *Technical Report SGI-R-80-017*, Sierra Geophysics, 150 N. Santa Anita, Arcadia, CA 91006.
- Mikami, N. and Hirahara, K. (1981). Global distribution of long-period P-wave attenuation and its tectonic implications, *J. Phys. Earth*, 29, 97-117.
- Mikumo, T. and T. Kurita (1968). Q distribution for long-period P waves in the mantle, *J. Phys. Earth*, 16, 11-29.
- Minster, J.B., J.M. Sasino, W.L. Rodi, T.H. Jordan and J.F. Masso (1981). *Three-*

- dimensional velocity structure of the crust and upper mantle beneath the Nevada Test Site*, Report SSS-R-81-5138, Systems, Sciences, and Software, P.O. Box 1620, LaJolla, CA, 92038.
- Minster, J.B. (1978a). Transient and impulse response of a linearly attenuation medium, Part I. Analytic results, *Geophys. J. R. astr. Soc.*, 52, 479.
- Minster, J.B. (1978b). Transient and impulse response of a linearly attenuation medium, Part II. A parametric study, *Geophys. J. R. astr. Soc.*, 52, 503.
- Minster, J. B., T. H. Jordan, P. Molnar and E. Haines (1974). Numerical modeling of instantaneous plate tectonics, *Geophys. J. R. Astr. Soc.*, 36, 541-576.
- Morgan, W.J. (1972). Deep mantle convection plumes and plate motions, *Amer. Ass. Petrol. Geol. Bull.*, 56, 203-213.
- Nakanishi, I. (1979a). Phase velocity and Q of mantle Rayleigh waves, *Geophys. J. R. astr. Soc.*, 58, 35-59.
- Nakanishi, I. (1979b). Attenuation of Multiple ScS waves beneath the Japanese arc, *Phys. Earth Planet. Inter.*, 19, 337-347.
- North, R. G. (1977). Station magnitude bias - its determination, causes and effects, Lincoln Lab. Technical Note TN-1977-24, Massachusetts Institute of Technology, Cambridge, Massachusetts.
- Nuttli, O. W. (1972). The amplitude of teleseismic P waves, *Bull. Seism. Amer.*, 62, 343-356.
- Poppe, B. B. (1980). Directory of world seismograph Stations vol. 1. The Americas - Pt. 1, United States, Canada, and Bermuda, Report SE-25, World Data Center A for Solid Earth Geophysics, U. S. Dept. of Interior, Geological Survey, Denver, CO 80225.
- Press, F. (1966). Seismic Velocities, in: *Handbook of Physical Constants*, Rev. Ed., Editor S. P. Clark, Jr., 197-218.

- Reiter, M. A. and J. K. Costain (1979). Heat flow in southwest Virginia, *J. Geophys. Res.*, **78**, 1323-1333.
- Richter, C. F. (1958). *Elementary Seismology*, W. H. Freeman and Company, San Francisco.
- Ringdal, F. (1976). Maximum-likelihood estimation of seismic magnitude, *Bull. Seism. Soc. Am.*, **66**, 769-802.
- Ringdal, F. (1977). P-wave amplitudes and sources of scattering in m_b operations, *J. Geophys.*, **43**, 611-622.
- Romanowicz, B. (1978). Seismic structure of the upper mantle beneath the U.S. by three-dimensional inversion of body wave arrival times, *Geophys. J. R. Astr. Soc.*, **57**, 479-508.
- Romney, C., B. G. Brookes, R. H. Mansfield, D. S. Carder, J. N. Jordan, and D. W. Gordon (1962). Travel times and amplitudes of principal body phases recorded from Gnome, *Bull. Seism. Soc. Amer.*, **52**, 1057-1074.
- Ruff, L. and R. Butler (1978). Amplitude variation of Russian nuclear events: Implications for source regions and the lowermost mantle, *EOS Trans.*, **59**, 327.
- Ruff, L. and D.V. Helmberger (1982). The structure of the lowermost mantle determined by short-period P-wave amplitudes, *Geophys. J. R. astr. Soc.*, **68**, 95-119.
- Sailor, R. and A. Dziewonski (1978). Measurements and interpretation of normal mode attenuation, *Geophys. J. R. astr. Soc.*, **53**, 559-582.
- Samuels, C. G., J. C. Smith, and G. Schubert (1981). A critical assessment of estimation methods for activation volume, *J. Geophys. Res.*, **86**, 10707-10731.
- Sass, J. H., A. E. Lachenbruch, R. J. Munroe, G. W. Greeve and T. H. Moses, Jr. (1971). Heat flow in the western United States, *J. Geophys. Res.*, **76**, 6376-

6413.

- Sass, J. H., W. H. Diment, A. H. Lachenbruch, B. V. Marshall, R. J. Munroe, T. H. Moses and T. C. Urban (1976). A new heat-flow contour map of the conterminous United States, *Open-File Report 76-756*, Geological Survey, U. S. Department of Interior.
- Sato, R. (1967). Attenuation of seismic waves, *J. Geophys. Earth*, 2, 32-60.
- Sato, R. and A.F. Espinosa (1967). Dissipation in the Earth's mantle and rigidity and viscosity in the Earth's core determined from waves multiply reflected from the mantle-core boundary, *Bull. Seism. Soc. Amer.*, 57, 5, 829-856.
- Savage, J.C. (1966). Radiation from a realistic model of faulting, *Bull. Seism. Soc. Amer.*, 56, 577-592.
- Sengupta, M.K. (1975). *The Structure of the Earth's Mantle from Body Wave Observations*, (Ph.D. Dissertation), Mass. Inst. of Technology, Cambridge, Massachusetts, 579 pp.
- Sengupta, M. K. and M. N. Toksöz (1977). The amplitude of P waves and magnitude corrections for deep focus earthquakes, *J. Geophys. Res.*, 82, 2971-2980.
- Sipkin, S.A. and T.H. Jordan (1979). Frequency Dependence of Q ScS, *Bull. Seism. Soc. Amer.*, 69, 1055-1079.
- Solomon, S. C. (1972). Seismic wave attenuation and partial melting in the upper mantle of North America, *J. Geophys. Res.*, 77, 1483-1502.
- Solomon, S. C. and M. N. Toksöz (1970). Lateral variation of attenuation of P and S waves beneath the United States, *Bull. Seism. Soc. Amer.*, 60, 814-838.
- Spence, W. (1974). P wave residual differences and inferences on an upper mantle source for the Silent Canyon Volcanic Centre, Southern Great

- Basin, Nevada. *Geophys. J. R. astr. Soc.*, **38**, 505-523.
- Stockwell, C.H. (1964). Fourth report on structural provinces, orogeneis and time classification of the Canadian precambrian shield, *Geol. Surv. Canada, Dept. of Mines and Tech. Surveys paper*, 64-117, Part II.
- Suppe, J., C. Powell, and R. Berry (1973). Regional topography, seismicity, volcanism, and the present-day tectonics of the western United States, *Stanford Univ. Pubs. Geol. Sci.*, **13**, 181.
- Teng, T.L. (1968). Attenuation of body waves and Q structure of the mantle, *J. Geophys. Res.*, **73**, 2195-2205.
- Tremblay, L.D. and J.W. Berg (1968). Seismic source characteristics from explosion-generated P waves, *Bull. Seism. Soc. Amer.*, **58**, 1833.
- Tsai, Y. B. and K. Aki (1969). Simultaneous determination of the seismic moment and attenuation of seismic surface waves, *Bull. Seism. Soc. Am.*, **59**, 275-287.
- Von Seggern, D. and R. Blandford (1972). Source time functions and spectra for underground nuclear explosions, *Geophys. J. R. astr. Soc.*, **31**, 83.
- Willey, G., J. R. Cleary and P. D. Marshall (1970). Comparison of least squares analyses of long and short period P wave amplitudes, *Geophys. J. R. Astr. Soc.*, **19**, 439-445.
- Yoshida, M. and M. Tsujiurn (1975). Spectrum and attenuation of multiply reflected core phases, *J. Phys. Earth*, **23**, 310-342.

CIRES
Cooperative Institute for Research in Environmental Sciences
University of Colorado / NOAA
Boulder, Colorado

III. Anelasticity of the Lower Mantle and Source Excitation Inferred from Low Frequency Free Oscillations.

INTRODUCTION

In recent years, the availability of improved quality seismic records has stimulated research efforts directed at determining the anelastic behavior of the earth. Obtaining refined estimates of the Q of the earth free oscillations has been one of the primary goals of this research. Research efforts directed at measuring the Q of free oscillations have included Alsop *et al.* (1961); Slichter (1967); Norwozi (1968, 1974); Dratler *et al.* (1971); Sailor and Dziewonski (1978); Buland and Gilbert (1978); and Stein and Geller (1978b) among others. Anderson and Hart (1978) very nicely summarize the results of these research efforts. Because of these efforts, many reliable estimates of Q for all but the longest period (lowest order) free oscillation modes are now available. The reliable measurement of Q for the lowest order modes has suffered from the relative scarcity of high-quality very long period (VLP) seismic records. However, this is not the only obstacle to Q estimation for these modes. Every earth free oscillation with non-zero angular order is subject to a spectral splitting of its resonance peak that results from the earth's rotation, slightly aspherical shape, and lateral heterogeneities (the mechanical analog of the Zeeman effect). At very long periods, the spacing of the split members (singlets) of a given free oscillation is such as to cause an interference that manifests itself, in the time domain, as a beating, and, in the frequency

domain, as a deformation of spectral peaks. Stein and Geller (1978b), in an experiment to evaluate the effects of this splitting on commonly used methods of measuring attenuation, demonstrated that the splitting can introduce substantial inaccuracies in the results of such measurements. One such "conventional" method, that of estimating the rate of decay of a time series, is thrown off by the time domain beating, while another method, that of measuring the width of a resonant spectral peak, is thrown off by the interference of the neighboring singlet peaks. Reliable measurement of Q at these long periods requires techniques that take into account the spectral splitting. Stein and Geller present such a technique. Making use of assumed source properties, they model the excitation of the free oscillation for several values of Q and then compare the envelope functions† of the resulting time series with the envelope of the actual time series band-pass filtered about the frequency range of the free oscillation under consideration. The value of Q that corresponds to the envelope that most closely approximates the actual envelope is the value that they present as the Q determined by their method. In this study (Schnapp, 1983), I present a method of measuring Q that, also, involves modeling the split normal mode. However, I deviate from the approach taken by Stein and Geller in that the modeling is done independently of any

† The definition of the envelope function that I use throughout this paper is $E(t) = \left[f(t)^2 + \tilde{f}(t)^2 \right]^{1/2}$ where $E(t)$ is the envelope function, $f(t)$ is the time series, and $\tilde{f}(t)$ is the quadrature of the time series, defined as the inverse fourier transform of $\text{sign}(\omega) i \hat{f}(\omega)$.

knowledge of the source, and the comparison or 'fitting' is done in the frequency domain. Further, estimations of the source dependent excitation amplitudes are obtained in addition to estimates of Q for each mode inverted, giving the inversion results potential value in an inversion for source properties.

THEORETICAL DEVELOPMENT

The equation of motion governing the oscillations of an elastic, rotating and self-gravitating body is (Dahlen 1968)

$$\Lambda S = \rho_0 \omega^2 S \quad (2.1)$$

where Λ is an operator defined by:

$$\Lambda S = \Pi S + 2i\rho_0 \Omega \times S$$

and

$$\begin{aligned} \Pi S = & \rho_0 \nabla \varphi_1 + \rho_1 \nabla (\varphi_0 + \psi) + \nabla [S \rho_0 \nabla (\varphi_0 + \psi)] \\ & - E - \nabla [S (\nabla \cdot \tau_0)] + \nabla \cdot (S \nabla \tau_0) \end{aligned}$$

where the following definitions apply:

ρ_0 the equilibrium density distribution

$\rho_1 = -\nabla \cdot (\rho_0 S)$ is the change in density due to displacement

φ_0 is the equilibrium gravitational potential

$$\nabla^2 \varphi_1 = 4\pi G \rho_1$$

$\psi(r) = -\frac{1}{2} [\Omega^2 r^2 - (\Omega \cdot r)^2]$ is the rotational potential

E is the elastic stress tensor

$$\tau_0 = T_0 - \frac{1}{3} (\text{tr } T_0) I \text{ is the static stress deviator}$$

T_0 is the static stress field tensor

Thus, Π defines the effects of gravity and the relationship of stress to strain in the body.

Under the assumption that the effects of rotation and deviations of the earth from radial symmetry and lateral homogeneity

**Best
Available
Copy**

are small, it is possible to deal with these effects as perturbations to the equation of motion of a spherical, non-rotating, radially symmetric earth model. Dahlen (1968) applies perturbation theory, and, by taking advantage of the hermitian character of Λ , he derives an expression for the first order perturbation to the eigenfrequency due to the effects of the earth's ellipticity and rotation. He shows that, to zeroth order, the perturbed eigenfunctions are the same as the eigenfunctions of the unperturbed equation of motion. Because Λ is hermitian, the eigenvalues of Eqn. 2.1, ω^2 , are real, so that the normal mode solutions are unattenuated in time.

Following Liu and Archambeau (1975), the effects of anelasticity for an isotropic body can be included in the equation of motion by adding an anelastic operator Ξ to Π , where, for an isotropic material with complex elastic constants λ^* and μ^* ,

$$(\Pi + \Xi)\mathbf{S} = -(\lambda^* + 2\mu^*)\nabla(\nabla \cdot \mathbf{S}) + \mu^*(\nabla \times (\nabla \times \mathbf{S})) \\ - (\nabla \lambda^*)(\nabla \cdot \mathbf{S}) - (\nabla \mu^*)(\nabla \mathbf{S} + \mathbf{S} \nabla) \quad (2.2)$$

If we approximate the anelastic behavior of the body by a Kelvin-Voigt solid model, Π is the real part, and Ξ is the imaginary part of the expression on the right side of Eqn. 2.2. If we assume the somewhat more general standard linear solid approximation for the body, Ξ takes on a real component. Liu and Archambeau (1975) compute the complex perturbation to the eigenfrequency of toroidal normal modes for the Kelvin-Voigt solid approximation, and in a subsequent paper (1976), they do the same for a standard linear solid approximation. They determined that the corrections

to the real part of the eigenfrequency for the Kelvin-Voigt case were on the order of 0.1 percent which was at the limit of observational accuracy at that time, while in the more general standard linear solid case, the corrections were considerably more significant, between 2 and 5 percent. In either case, the effect of Ξ is to make the operator Λ non-hermitian so that ω takes on an imaginary component. The result is that the solutions to the equation of motion, $S(r, \theta, \varphi; \omega)$, transformed into the time domain, take the form

$$S_k(r, \theta, \varphi; t) = A_k(r, \theta, \varphi) e^{-\gamma_k t} e^{i\Omega_k t}$$

where the subscript k is an index that distinguishes the individual solutions and Ω_k and γ_k are the real and imaginary parts of the perturbed eigenfrequency. From this expression for the solutions, it is immediately evident that the effect of the perturbation is to introduce the damping term $e^{-\gamma_k t}$ into the solutions. In terms of the quality factor, Q , the solution takes the form

$$S_k(r, \theta, \varphi; t) = A_k(r, \theta, \varphi) e^{-\Omega_k t / 2Q} e^{i\Omega_k t} \quad (2.5)$$

It is this form of the solution to the equation of motion of an isotropic, anelastic, rotating, elliptical, and self-gravitating earth model that forms the foundation for the method of inversion presented in the following discussion.

The inversion technique for determining the Q of the low order free oscillations consists of finding a suitably constrained model that has a complex spectrum that is closer to the actual spectrum, in a least squares sense, than any other similarly constrained model. The model is an ideal damped multi-mode oscillator with

resonances at frequencies that correspond to the singlet frequencies of the free oscillation. Its time dependence is simply that of Eqn. 2.3. The mathematical form of the model, in the time domain, is:

$$F(t) = \text{Real} \left[\sum_{m=-l}^{m=l} A_m e^{-\frac{\Omega_m t}{2Q}} e^{i\Omega_m t} \right] \quad (2.4)$$

where the subscript m denotes the singlet of azimuthal order m . A_m is the complex excitation amplitude corresponding to the m^{th} singlet whose magnitude and phase are determined by both the source properties and the lag between the time when the actual excitation occurred, and the reference time of the model (the time $t=0$ in Eqn. 2.4). Ω_m is the angular frequency of oscillation of the m^{th} singlet and the Q is the Q of the free oscillation. In an effort to minimize the number of independent parameters in the inversion, I have assumed that Q is substantially constant over the frequency range of the multiplet.

Eqn. 2.4 defines the time domain representation of a model of a single normal mode multiplet (radial order n and angular order l are fixed). In actual application, such a multiplet is isolated from other multiplets by the application of a narrow band-pass filter to the data. The width of the filter is chosen so that all spectral samples that display significant signal content as compared to the ambient noise level are included in the pass-band. Isolation of the ${}_0S_2$ and ${}_0S_3$ multiplets from other multiplets is insured in this way because of the fact that at the long periods corresponding to

these modes, neighboring multiplets are well separated in frequency.

The Fourier transform (abbreviated FT) of $F(t)$ in Eqn. 2.4 is:

$$\hat{F}(\omega) = \sum_{m=-l}^{m+l} A_m f_m(\omega, Q, \Omega_m) \quad (2.5)$$

where f_m is the complex function that corresponds to the FT of the exponents in Eqn. 2.4. The inversion technique involves finding the model whose complex spectrum, \hat{F} , minimizes the difference function:

$$\Delta = \int \left| \hat{F}(\omega) - F_0(\omega) \right|^2 d\omega$$

where F_0 is the spectrum of the data to be inverted. Since the spectra that I'll be dealing with are not continuous but, rather, discretely sampled, a more appropriate form for the difference function minimized by the inversion is

$$\Delta = \sum_{k=1}^N \left| \hat{F}(\omega_k) - F_0(\omega_k) \right|^2 \Delta\omega$$

where N is the number of sampled frequencies ω_k , and $\Delta\omega$ is the spectral sampling interval.

An important property of Eqn. 2.5 is that \hat{F} is linear in the complex excitation amplitudes A_m . So, with given singlet frequencies Ω_m , \hat{F} exhibits a nonlinear dependence on only one unknown, Q . The linearity of Eqn. 2.5 in all unknowns except for Q permits the application of a simple, fast inversion method for both the Q and the A_m 's simultaneously. This technique involves solving a linear least-squares problem in the unknown A_m 's for fixed values of Q . By

comparing the resulting values of the difference function, the Q which minimizes Δ can be determined.

At this point, it is useful to formulate the problem in vector form. Let \underline{F} be the vector $[\hat{F}(\omega_k), k=0,1,\dots,N]$ and \underline{A} be the vector $[A_m, m=-l,\dots,l]$. Since \hat{F} is linear in the A_m 's, Eqn. 2.5 can be written in vector form as

$$\underline{F} = \underline{M}\underline{A} \quad (2.6)$$

where \underline{M} is the matrix whose elements are (from Eqn. 2.5) $M_{kj} = f_1(\omega_j, Q, \Omega_k)$. For fixed Q and singlet frequencies Ω_m , minimizing the difference function expressed in vector form as:

$$\Delta = |\underline{F} - \underline{F}_0|^2 = (\underline{F} - \underline{F}_0)' (\underline{F} - \underline{F}_0)$$

becomes a problem in determining the least-squares inverse of Eqn. 2.6, that is, in solving the vector equation

$$\underline{M}'\underline{M}\underline{A} = \underline{M}'\underline{F}_0$$

for \underline{A} . If $\underline{M}'\underline{M}$ is non-singular the solution can be written as

$$\underline{A} = (\underline{M}'\underline{M})^{-1}\underline{M}'\underline{F}_0 \quad (2.7)$$

Thus, given a set of observed complex spectral amplitudes, \underline{F}_0 , and a set of singlet frequencies, Ω_m , for any one value of Q , the elements of \underline{M} can be computed and a least-squares *closest-fitting* set of excitation amplitudes \underline{A} can be determined by computing the product of the matrix $(\underline{M}'\underline{M})^{-1}\underline{M}'$ with the vector of the actual complex spectrum, \underline{F}_0 . Repeating the process for several values of Q , the relative fits of the resulting *closest-fitting* models to the actual spectrum (as measured by Δ) can be compared to find the Q that

minimizes Δ . This Q and associated set of excitation amplitudes I refer to as the *estimated* or *inverted* Q and associated excitation amplitudes. The model generated by this Q and associated excitation amplitudes I refer to as the *best-fitting* model.

Throughout the preceding discussion the singlet frequencies were assumed to be known. Uncertainty in the singlet frequencies can be taken into account by allowing them to vary within their respective uncertainty limits over the course of repeated applications of the previously described inversion process to a particular data set. Each set of singlet frequencies will have associated with it a *best-fitting* model and corresponding *inverted* Q . Uncertainty in the Q that results from an uncertainty in the singlet frequencies can then be estimated by statistically evaluating this set of inverted Q 's.

APPLICATION TO REAL DATA

For a first attempt at applying the Q inversion technique to a real data set, I obtained the highest quality long-period seismogram that I could find, a 500 hour length of the Isabella strain record of the May 22, 1960 great Chilean earthquake. The raw time series had a sampling interval of one minute and contained 32768 points. I pre-processed the raw data by de-glitching and low-pass filtering (to inhibit aliasing) the time series. This allowed me to decimate the time series by a factor of eight so as to obtain a somewhat more manageable length of 4096 points. Fig. 3.1 displays the pre-processed seismogram. I then took a 280 hour long section of the time series starting at 28.4 hours after the main shock and applied a Fast Fourier Transform to it to obtain a discretely sampled, finite length complex spectrum. Fig. 3.2 displays the modulus of the resulting spectrum. Many of the low order free oscillations, especially the ${}_0S_2$, ${}_0S_3$, ${}_0S_4$, and ${}_0S_5$ modes, are quite evident in the spectrum. The ${}_0T_2$, ${}_0T_3$, and ${}_0T_4$ modes are not quite so apparent.

In order to apply the inversion routine to this data set, I required estimates of the splitting parameters that define the singlet frequencies of the free oscillations. Buland, Berger, and Gilbert (1979) obtained refined estimates of the singlet frequencies for ${}_0S_2$ and ${}_0S_3$ by stacking spectra from the IDA records of the 1976 Sumbawa Indonesia earthquake. From these frequencies, they com-

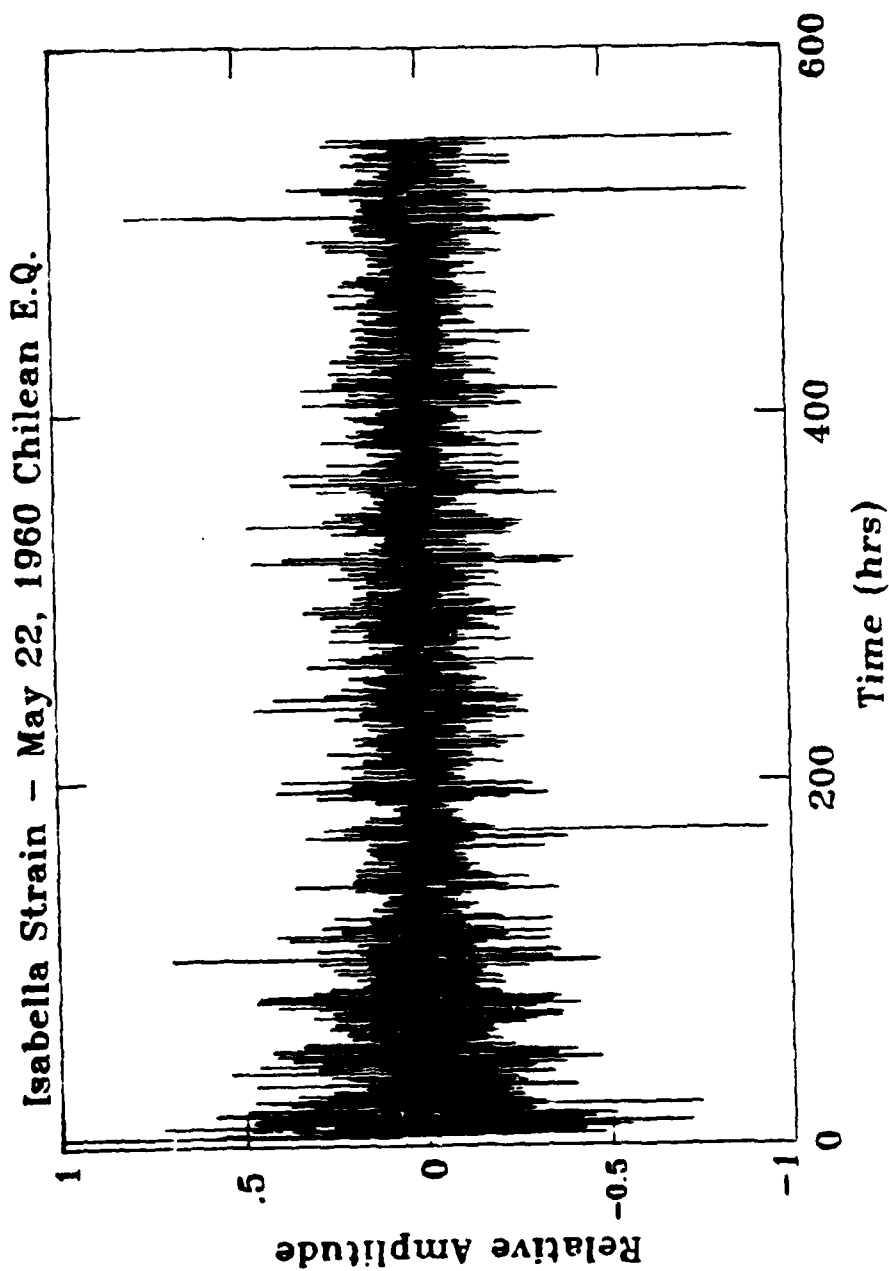


Fig 3.1 Pre-processed (de-glitched and low-pass filtered to inhibit aliasing) seismogram of the May 22, 1960 Chilean Earthquake. Amplitude is relative scaled to 1 and time is in hours after the main shock.

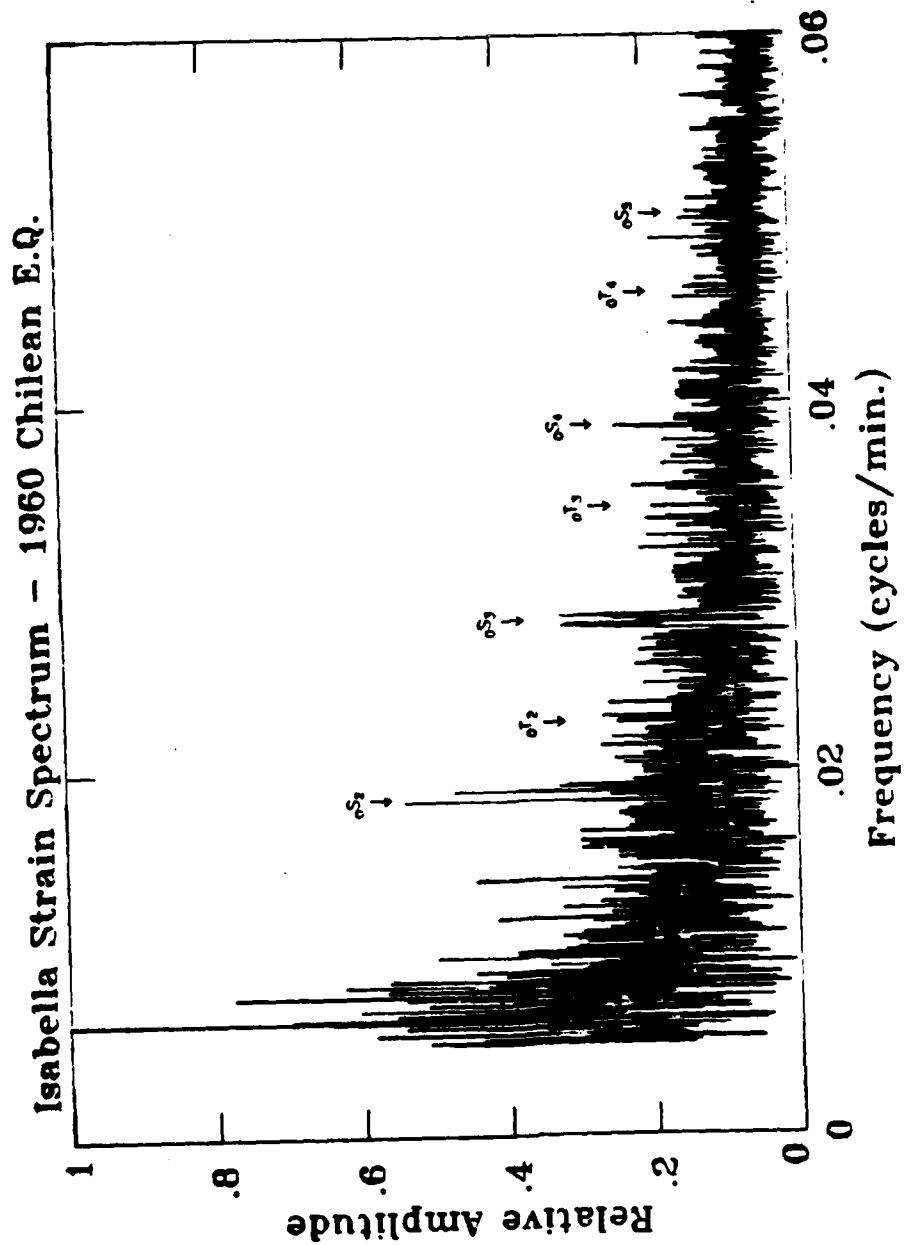


Fig. 3.2 Spectrum of seismogram displayed in Fig. 3.1. The low order Spheroidal Modes are evident in the spectrum. The Toroidal modes are somewhat more obscure. Amplitude is relative scaled to 1 and Frequency is given in cycles/minute.

puted the three splitting parameters ω_0 , f , and g , that define the singlet frequencies via the relation $\omega_m = \omega_0 + fm + gm^2$, where m is the azimuthal order of the singlet. Table 1 lists these splitting parameters and associated singlet frequencies for ${}_0S_2$ and ${}_0S_3$. All frequency values presented in this thesis are in units of cycles/minute (cpm) unless otherwise noted. Note that in order to apply the theory developed in chapter 2, these values must be converted to angular frequency (e.g., radians/second).

TABLE 1
Assumed Splitting Parameters and
Associated Singlet Frequencies

Mode	Splitting Paras. (cpm)	Azimuthal Order	Singlet Freq (cpm)
${}_0S_2$	$\omega_0 = .018568$ $f = 2.771 \times 10^{-4}$ $g = -3.253 \times 10^{-6}$	$m = -2$.018001
		-1	.018288
		0	.018568
		1	.018842
		2	.019109
${}_0S_3$	$\omega_0 = .028125$ $f = 1.316 \times 10^{-4}$ $g = -4.078 \times 10^{-6}$	$m = -3$.027693
		-2	.027845
		-1	.027989
		0	.028125
		1	.028252
		2	.028372
		3	.028483

Using these splitting parameters as the *assumed* splitting parameters (the splitting parameters used to compute the singlet frequencies required by the inversion routine), band-limited sections of the complex spectrum in the ${}_0S_2$ and ${}_0S_3$ frequency ranges were processed through the inversion routine. The width of the spectral bands were chosen so as to minimize the noise power in the band while retaining all spectral points that have a significant signal component. For ${}_0S_2$, the band selected extended from .0178 to .0193 cycles per minute. For ${}_0S_3$, the band extended from .027575 to .028575 cycles/min. For these modes, the inversion routine determined a single minimum in the difference function Δ (see chapter 2) for a range of Q 's extending from 50 to 2000.* The resulting *inverted* Q 's were 399 for ${}_0S_2$ and 358 for ${}_0S_3$. The associated complex excitation amplitudes are presented in Table 2. In the table, the amplitude values corresponding to a given multiplet are all scaled by the same factor so that the root-mean-square of the values is unity.

In order to evaluate qualitatively the results of this application of the inversion routine to the Chilean data, I generated some plots that display a comparison of the actual data to the *best-fitting* model. Figs. 3.3 and 3.4 show, for each mode, a time domain comparison of the envelopes of the inverse Fourier transform of the

* I used the criterion of a single minimum in Δ for Q 's between 50 and 700 to determine which modes might be reliably invertable. ${}_0S_2$ and ${}_0S_3$ were the only modes that met the criterion.

TABLE 2

Complex Excitation Amplitudes

Mode	Azimuthal Order	Complex Excitation	
		Amplitude	Phase (rad)
${}_0S_2$	$m = -2$	0.539 ± 0.357	0.571 ± 0.964
	-1	1.950 ± 0.379	-0.622 ± 0.265
	0	0.238 ± 0.340	0.917 ± 0.798
	1	2.102 ± 0.337	0.788 ± 0.240
	2	1.195 ± 0.379	-2.164 ± 0.605
${}_0S_3$	$m = -3$	0.974 ± 0.400	-0.272 ± 1.286
	-2	2.092 ± 0.426	-1.534 ± 0.474
	-1	0.957 ± 0.376	1.229 ± 1.162
	0	0.703 ± 0.439	0.035 ± 1.100
	1	0.874 ± 0.535	-2.206 ± 1.193
	2	2.237 ± 0.351	1.517 ± 0.570
	3	1.202 ± 0.418	-0.214 ± 0.868

band-limited section of the spectrum defined previously. The time series envelopes so compared are equivalent to the envelopes of the actual data and the *best-fitting* model after being *box-car* band-pass filtered in the characteristic frequency range of the free oscillation. The solid curve corresponds to the actual data and the dashed curve to the results of the inversion. Time is given in hours after the main shock.

Figs. 3.5 and 3.6 display a frequency domain comparison of the observed amplitude spectrum (the square-root of the power spec-

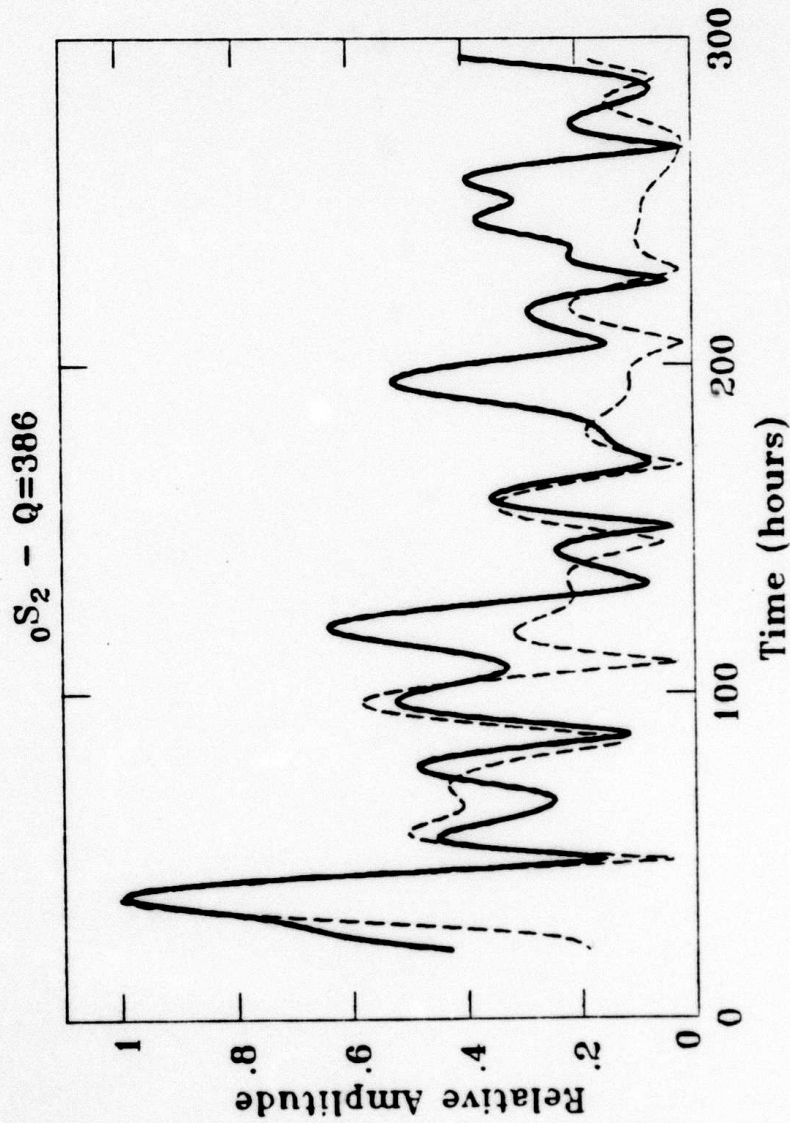


Fig. 3.3 Time domain comparison of the envelopes of the inverse fourier transform of band-limited sections of the actual spectrum and the *best-fitting* spectrum for oS_2 . The range of the frequency band used here was .0178 - .0193 cycles/minute. Amplitude is relative scaled to 1 and time is in hours after the main shock.

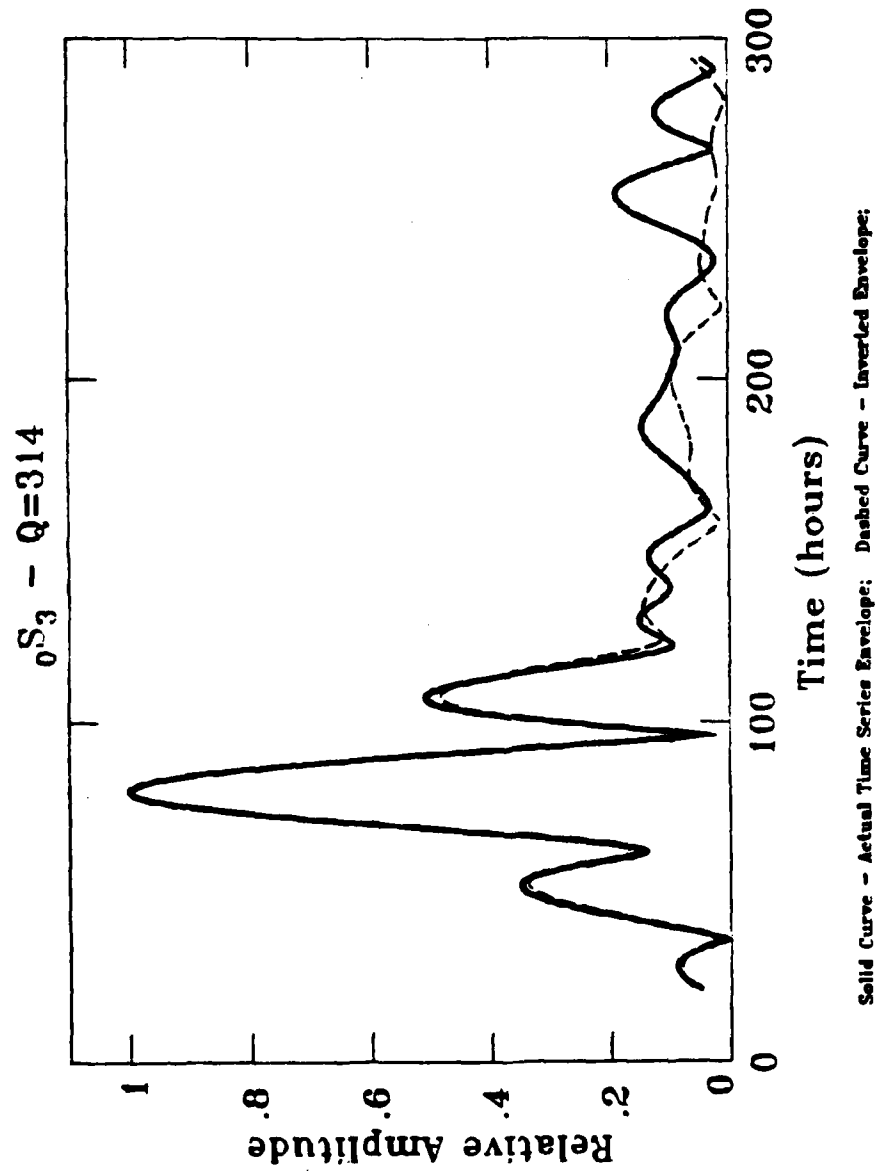
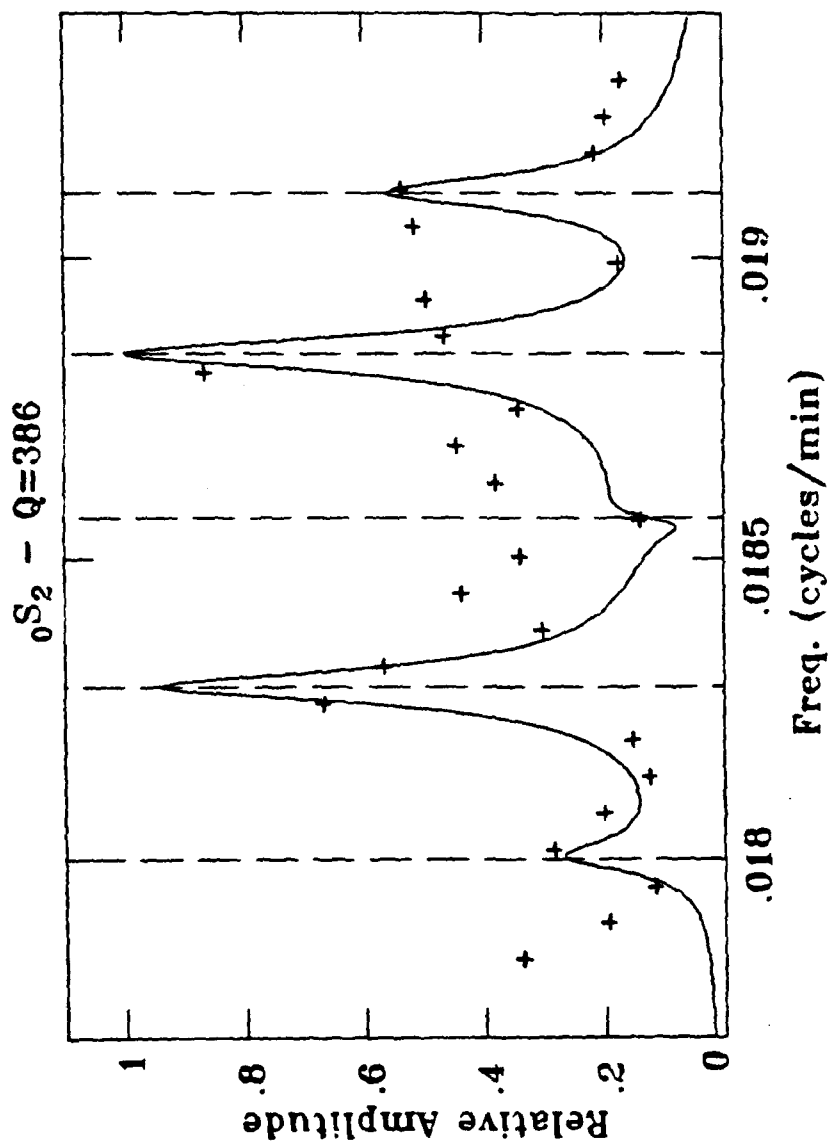


Fig. 3.4 Same type of comparison as displayed in Fig. 3.3 for $0S_3$. The frequency range used here was .027575 - .028575 cpm.

trum) and the spectrum of the *best-fitting* model in the frequency range of the modes. The crosses correspond to the discrete samples of the actual spectrum, and the continuous curve, to the inverted spectrum. The dashed lines indicate the location of the singlet frequencies used in the inversion.

The plots show that the inversion routine is yielding model parameters that generate envelope functions and amplitude spectra that fit the data reasonably well. The envelope comparisons show that it is the signal in the earlier portions of the record that is primarily being fit as it should be, while the noise in the latter portions are not. The ${}_0S_3$ envelope fit appears to be quite close in the first 150 hours. The closeness of the fit, however, is an artifact of the large number of inversion parameters, 15 (7 complex excitation amplitudes and Q), relative to the number of data points, 17 real and 17 imaginary components of the spectrum. The number of degrees of freedom ($=$ # of data points - # of parameters) is therefore only 21. Note that for ${}_0S_2$, with 37 degrees of freedom (11 parameters and 48 data points), the envelope fit is not as good. Thus, the apparently good ${}_0S_3$ envelope fit should not be used as an indicator of especially reliable inversion results. The spectral comparisons also show that the spectral points that contain the majority of the information on the signal, i.e., the highest peaks in the spectrum, are fit the best. The ${}_0S_2$ comparison displays this better than the ${}_0S_3$ one. Note that in the ${}_0S_2$ comparison, the curve showing the spectrum of the *best-fitting* model falls consistently below



— Actual Spectrum; Solid Curve - Inverted Spectrum; Dashed Lines - Singlet Frequencies;

Fig. 3.5 Comparison of the actual amplitude spectrum with the spectrum of *best-fitting* model for $0S_2$. The discrete points of the actual spectrum are plotted as crosses while the inverted spectrum is plotted as a continuous curve. The vertical dashed lines indicate the locations of the singlet frequencies used in the inversion. Amplitude is relative scaled to 1 and frequency is given in cycles/minute.

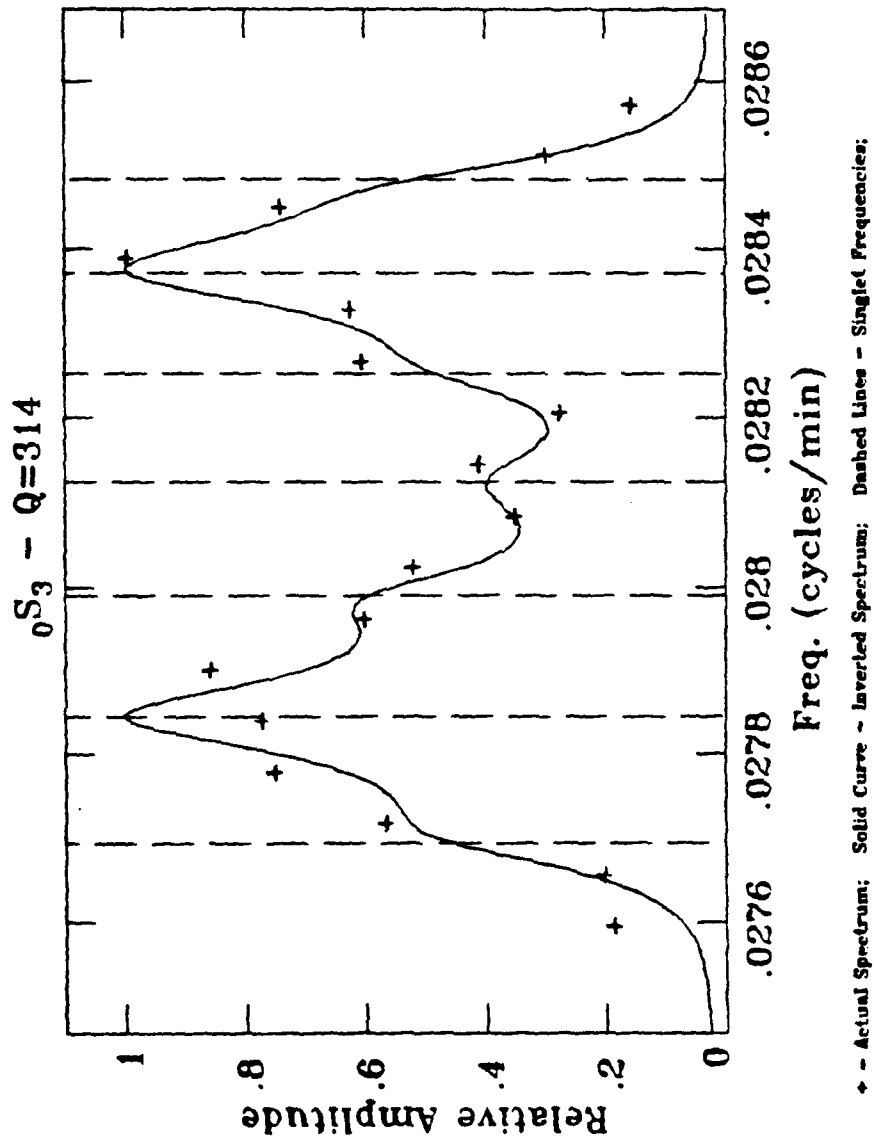


Fig. 3.6 Same type of comparison as displayed in Fig. 3.5 for $0S_3$.

the actual spectral amplitudes. This is a result of the fact that the inversion fits the complex spectrum, i.e., the real and imaginary parts, while the plot displays the modulus of the spectrum. Since the modulus is the sum of the squares of the real and imaginary parts, if the *best-fitting* spectrum, on the average, deviates from the actual spectrum equally in both the plus and minus directions, the modulus will tend to deviate more in the minus direction, thus causing apparent bias in the plot. As with the envelopes, the cS_3 spectra of the *best-fitting* model and the actual data compare quite well. Once again, this is likely an artifact of the large number of inversion parameters relative to the number of independent data points being fit.

The primary function of these plots is to provide a means of comparison of the results of different applications of the inversion to a given data set, in addition to providing reassurance that a "reasonable looking" fit is being obtained. I refrain from using them to compare the results obtained here with those of other researchers since there is no common ground on which to base such a comparison. Stein and Geller (1978b) make use of plots of *smoothed* time series envelopes to display the results of their efforts at estimating Q . However, since their models are more heavily constrained than mine (being constrained by the assumed source properties), it is difficult to use such qualitative comparisons as the plots to evaluate the relative merit of the two techniques

A somewhat more quantitative evaluation of the inversion results can be made by appealing to normal mode excitation theory to supply a relationship among the excitation amplitudes within a given multiplet. Stein and Geller (1977) derive such a relationship. If the displacement associated with an earth normal mode of angular order l and azimuthal order m , $U_{l,m}(r)$, is expressed in terms of a displacement amplitude, $B_{l,m}$, and the eigenfrequency, ω_{lm} , via the relation

$$U_{l,m}(r,t) = B_{l,m}(r)e^{i\omega_{lm}t} + (B_{l,m}(r))^*e^{-i\omega_{lm}t}$$

then the displacement amplitudes within a multiplet obey the following symmetry relation:

$$B_{l,m} = (B_{l,-m})^*$$

where $*$ denotes complex conjugation. While Stein and Geller derived this relation for a point double-couple source, by using the formalism developed by Gilbert (1971) and the expressions for the normal mode strain tensor elements given by Gilbert and Dziewonski (1975), it is possible to show that the relation holds true for any point source. Now, for gravimeter records, an excitation amplitude, $A_{l,m}$, determined by the inversion routine is the component in the recording direction of the seismograph of $B_{l,m}(r_R)$, where r_R is the receiver location, so that the excitation amplitudes must also satisfy the above symmetry relation. For strain records such as the Chilean data, the $A_{l,m}$'s are a component of $\nabla B_{l,m} + B_{l,m}\nabla$. Since ∇ is a purely real linear operator, $\nabla(B_{l,m})^* + (B_{l,m})^*\nabla = (\nabla B_{l,m} + B_{l,m}\nabla)^*$ so

that $B_{l,m} = (B_{l,-m})^*$ implies $A_{l,m} = (A_{l,-m})^*$. This symmetry leads to the following constraints on the amplitude and phase components of the excitation amplitudes:

$$|A_{l,m}| = |A_{l,-m}| \quad \gamma_{l,m} = -\gamma_{l,-m}$$

where $|A_{l,m}|$ and $\gamma_{l,m}$ are the amplitude and phase components of $A_{l,m}$ defined by $A_{l,m} = |A_{l,m}| e^{i\gamma_{l,m}}$. These symmetry relations provide a means of evaluating the results of the inversion of the actual data. The components of the amplitudes obtained from the inversion should, within their uncertainty limits, satisfy the above symmetry constraints. By referring to Table 2 and to the plots in Figs 4.5 to 4.8 in the following section, one can see that this is indeed the case for every excitation amplitude obtained from the inversion of the Chilean data. Where the uncertainty is relatively small, as with the $m = \pm 1$ singlets of ${}_0S_2$ and the $m = \pm 2$ singlets of ${}_0S_3$, the estimates come quite close to actually meeting the symmetry conditions.* This result contributes significantly to the confidence that I have in the reliability of the results.

REFERENCES

- Agnew, D. C., and J. Berger, 1978, Vertical Seismic Noise at Very Low Frequencies, *J. Geophys. Res.* **83**, 5420-5424.
- Agnew, D., J. Berger, R. Buland, W. Farrell, and F. Gilbert, 1976, International Deployment of Accelerometers: A network for very long period seismology, *EOS Trans. AGU*, **57**, 180-188.
- Aki, K. and P. G. Richards, 1980, *Quantitative seismology. Theory and methods*, Vol. 2. San Francisco, Freeman and Co.,
- Alsop, L. E., G. H. Sutton and M. Ewing, 1961, Measurement of Q for very long period free oscillations, *J. Geophys. Res.* **66**, 2911-2915.
- Alterman, Z., H. Jarosch, and C. L. Pekeris, 1959, Oscillations of the earth, *Proc. Roy. Soc. London, Ser. A*, **252**, 80-95.
- Anderson, D. L., A. Ben-Menahem, and C. B. Archambeau, 1965, Attenuation of seismic energy in the upper mantle, *J. Geophys. Res.*, **70**, 1441-1443.
- Anderson, D. L., and R. S. Hart, 1978, Q of the earth, *J. Geophys. Res.*, **83**, 5869-5882.
- Backus, G. and F. Gilbert, 1961, The rotational splitting of the free oscillations of the earth, *Proc. Natl. Acad. Sci. U.S.*, **47**, 362-371.
- Backus, G. and F. Gilbert, 1967, Numerical application of a formalism for geophysical inverse problems, *Geophys. Jour. Roy. Astro. Soc.*, **13**, 247-276.
- Backus, G. and F. Gilbert, 1968, The resolving power of gross earth data, *Geophys. Jour. Roy. Astro. Soc.*, **16**, 169-205.
- Backus, G. and F. Gilbert, 1970, Uniqueness in the inversion of inaccurate gross earth data, *Phil. Trans. Roy. Soc. London, Ser. A*, **266**, 123-192.
- Benioff, H., F. Press, and S. Smith, 1961, Excitation of the free oscillations of the earth, *J. Geophys. Res.*, **66**, 605-619.
- Bolt, B. A. and D. R. Brillinger, 1979, *Geophys. Jour. Roy. Astro. Soc.*, **59**, 593-603.

- Brune, J. N., and J. Oliver, 1959, The seismic noise of the earth's surface, *Bull. Seismol. Soc. Amer.*, **49**, 349-353.
- Buland, R. and F. Gilbert, 1978, Improved resolution of complex eigenfrequencies in analytically continued seismic spectra, *Geophys. Jour. Roy. Astro. Soc.*, **52**, 457-470.
- Buland, R., J. Berger, and F. Gilbert, 1979, Observations from the IDA network of attenuation and splitting during a recent earthquake, *Nature*, **277**, 358-362.
- Dahlen, F. A., 1968, The normal modes of a rotating elliptical earth, *Geophys. Jour. Roy. Astro. Soc.*, **16**, 329-367.
- Dahlen, F. A., and R. V. Sailor, 1979, Rotational and elliptical splitting of the free oscillations of the earth, *Geophys. Jour. Roy. Astro. Soc.*, **58**, 609-624.
- Dahlen, F. A., and M. L. Smith, 1975, The influence of rotation on the free oscillations of the earth, *Phil. Trans. Roy. Soc. London, Ser. A*, **279**, 583-624.
- Dratler, J. W., E. Farrell, B. Block, and F. Gilbert, 1972, High Q overtone modes of the earth, *Geophys. Jour. Roy. Astro. Soc.*, **36**, 399-410.
- Fix, J. E., 1972, Ambient earth motion in the period range .1 to 2560 seconds, *Bull. Seismol. Soc. Amer.*, **62**, 1753-1760.
- Geller, R. J. and S. Stein, 1977, Split free oscillation amplitudes for the 1960 Chilean and 1964 Alaskan earthquakes, *Bull. Seismol. Soc. Amer.*, **67**, 651,660.
- Gilbert, F., 1971, Excitation of the normal modes of the earth by earthquake sources, *Geophys. Jour. Roy. Astro. Soc.*, **22**, 223-226.
- Gilbert, F. and G. Backus, 1965, The rotational splitting of free oscillations of the Earth, 2, *Rev. Geophys.*, **3**, 1-9.
- Gilbert, F., and A. M. Dziewonski, 1975, An application of normal mode theory to the retrieval of structural parameters and source mechanisms from seismic spectra, *Phil. Trans. Roy. Soc. London, Ser. A*, **278**, 187-269.
- Kanamori, H., 1980, Use of the IDA network for fast determination of earthquake source parameters, *EOS Trans. AGU*, **61**, 296.

- Kanamori, H. and J. J. Ciper, 1974, Focal process of the great Chilean earthquake May 22, 1960, *Phys. Earth Planet Interiors*, **9**, 128-136.
- Lancsoz, C., 1961, *Linear Differential Operators*. London, D. Van Nostrand, 564pp.
- Liu, H. and Archambeau, C. B., 1975, The effect of anelasticity on periods of the Earth's free oscillations (toroidal modes), *Geophys. Jour. Roy. Astro. Soc.*, **43**, 795-814.
- Liu, H. and C. B. Archambeau, 1976, Correction to 'The effect of anelasticity on periods of the Earth's free oscillations (toroidal modes)', *Geophys. Jour. Roy. Astro. Soc.*, **47**, 1-7.
- Lundquist, Gary M., 1979, The Frequency Dependence of Q . Ph.D. Thesis, University of Colorado, Boulder, Colorado.
- Mendiguren, J., 1973, Identification of free oscillation spectral peaks for 1970 July 31, Colombian deep shock using the excitation criterion. *Geophys. Jour. Roy. Astro. Soc.*, **33**, 281-321.
- Norwooz, A. A., 1968, Measurement of Q values from the free oscillations of the earth, *J. Geophys. Res.*, **73**, 1407-1415.
- Norwooz, A. A., 1974, Characteristic periods and Q for oscillations of the earth following an intermediate-focus earthquake, *J. Phys. Earth*, **22**, 1-23.
- Pekeris, C. L., Z. Alterman, and H. Jarosch, 1961, Rotational multiplets in the spectrum of the earth, *Phys. Rev.*, **122**, 1692-1700.
- Sailor, R. V., and A. M. Dziewonski, 1978, Measurements and interpretation of normal mode attenuation, *Geophys. Jour. Roy. Astro. Soc.*, **53**, 559-581.
- Saito, M., 1967, Excitation of free oscillations and surface waves by a point source in a vertically heterogeneous earth, *Geophys. Jour. Roy. Astro. Soc.*, **72**, 3689-3699.
- Slichter, L. B., 1967, Spherical oscillations of the earth, *Geophys. Jour. Roy. Astro. Soc.*, **14**, 171-177.

- Smith, S. W., 1972, The anelasticity of the mantle, *Tectonophysics*, **13**, 601-622.
- Stein, S. and R. J. Geller, 1977, Amplitudes of the split normal modes of a rotating, elliptical earth excited by a double couple, *J. Phys. Earth*, **25**, 117-142.
- Stein, S. and R. J. Geller, 1978a, Time-domain observations and synthesis of split spheroidal and torsional free oscillations of the 1960 Chilean earthquake: preliminary results, *Bull. Seismol. Soc. Amer.*, **49**, **68**, 325-332.
- Stein, S. and R. J. Geller, 1978b, Attenuation measurements of split normal modes for the 1960 Chilean and 1964 Alaskan earthquakes, *Bull. Seismol. Soc. Amer.*, **68**, 1595-1611.
- Stein, S. and J. A. Nunn, 1979, Analysis of split normal modes for the 1977 Indonesian earthquake, *Bull. Seismol. Soc. Amer.*, in press.
- Wiggins, R. A., The general linear inverse problem: Implication of Surface Waves and Free Oscillations for Earth Structure, *Rev. Geophys.*, **10**, 251-285.

IV. Signal Detection and Analysis Using Quasi-Harmonic

Decomposition (QHD) Methods

Introduction

In many research efforts in geophysics, time series analysis plays an important role. The data that the seismologist often deals with is often quite complex, consisting of many distinct components (e.g., seismic phases of various types, noise, etc.) superimposed on one another. Such data typically must be filtered (in a variety of ways) in order to facilitate the extraction of the discrete components that are required. The data components of interest ordinarily consist of isolated arrivals, or phases, that carry the basic units of information. One such filtering scheme, designed specifically to isolate individual arriving phases in a complex time series, is *Quasi-Harmonic Decomposition* (QHD)*. QHD filtering of a time series yields estimates of the arrival times of discrete seismic phases, together with a spectral estimate of each detected phase. The arrival time and spectral estimate associated with a given phase can then be used to reconstruct the arrival in the time domain. The net result is a decomposition of a complex time series into a series of discrete arrivals that can then be used in a variety of ways to infer properties of the source of the phases and the path they followed.

Some aspects of the QHD approach, in the context of seismic signal analysis, are discussed by Alexander (1963), Archambeau *et al.* (1965), Archambeau and Flinn (1965), Dziewonski, Block and Landisman (1969), Dziewonski, Mills and Block (1972), Instron, Marshall and Blamey (1971), Cara (1973) and Denny and Chin (1976), among others. This early work focused on narrow band filtering of seismic time series to determine the dispersive characteristics of

*Some of the terminology used in the QHD approach is somewhat specialized and therefore a glossary of the most common terms and symbols used is given in the Appendix 1.

surface waves and on polarization filtering, employing the multi-component information contained in the seismic wave field to extract seismic phases having particular particle motion characteristics. The QHD analysis procedure to be described here involves a combination of dispersion analysis, threshold detection and polarization analysis (when multi-component data is processed), used jointly in a pattern recognition procedure designed to automatically detect and isolate body wave arrivals of a particular type. (Other versions of the computer program can be employed to isolate and analyze surface waves of various types.) The methods and analysis procedures are described in Archambeau et al. (1982).

Thus the QHD analysis procedure used in the computer processing is capable of identifying body waves, of prescribed type, in a background of noise and other signal types, and provides the user with both the spectra and time domain wave forms for the individual signals occurring within the time series. In view of this capability, the program should be a useful tool for seismologists.

Basic Features and Methods in QHD Analysis

The essential feature of a quasi-harmonic decomposition of a time series, as opposed to a Fourier decomposition, is that *both* time and frequency information are retained. This is accomplished by parallel filtering of the time series with a set of Gaussian narrow band filters, the output of each filter corresponding to a single "quasi-harmonic component" of the original time series, with each of these having a modulated sinusoidal form. It is the modulation of the sinusoidal output that contains information concerning the *time* of energy arrival (group times) within the original time series, while the sinusoid (or "carrier") contains the spectral information related to these arrivals. (By contrast, a "Fourier decomposition" is equivalent to filtering with a set of delta function filters, centered at a discrete set of frequencies, the output of each being a

pure sinusoid. Since the sinusoids are not modulated they contain no arrival time information in themselves.)

Thus QHD analysis is designed to provide time varying spectral information. While moving window Fourier analysis also provides time varying spectral estimates, such an approach suffers from poor time resolution and contamination due to truncation effects, which can be severe. On the other hand, QHD provides time varying spectral estimates for which time resolution can be controlled (automatically by a computer or interactively by a user) and truncation effects do not occur. However, uncertainty in the frequency of the spectral estimate obtained does occur, and is the price to be paid for the time resolution achieved. The trade-off between time and frequency resolution in QHD is expressed by an "uncertainty principle" having the form $\overline{\Delta\omega\Delta t} \geq 1/2$, where $\overline{\Delta\omega}$ and $\overline{\Delta t}$ are the uncertainties in the frequency and time to be associated with each group arrival time and the spectral estimate of the signals. (For Gaussian filters $\overline{\Delta\omega\Delta t} \approx 1/2$, while for non-Gaussian filters $\overline{\Delta\omega\Delta t} > 1/2$). The uncertainty in frequency resolution results, in practice, in spectral smoothing, which can usually be tolerated and is often even desirable. Since $\overline{\Delta\omega}$ is nearly equal to the bandwidth of the Gaussian filter used, then this uncertainty principle provides us with a useful, quantitative, way of estimating the time and spectral value uncertainties associated with a QHD analysis.

In order to obtain accurate time and spectral information in practice (i.e. by automated, computer controlled analysis) a pattern recognition method is used to detect and isolate signals of specified character. The pattern recognition procedure is applied in the signal parameter space generated from the narrow band filtering operations. The idea is to have the computer search for regular patterns within the parameter "space" and to isolate, or pick out, those patterns that correspond to signals of interest to the user. For example, the

program can be instructed to search throughout the time series for signals with particular dispersion characteristics.

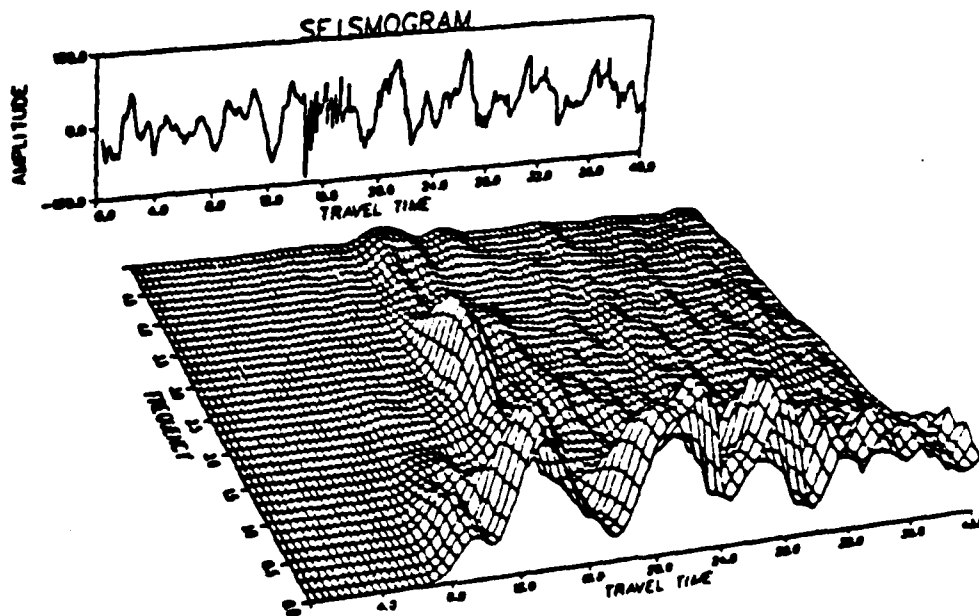


Figure 1 - Envelope functions, for the (reduced) travel time interval 8 to 40 sec, plotted on the time-frequency plane. The original seismic time series is shown in the panel. Body wave signals from an earthquake in a high noise background arrive at (approximately) 15 sec, and can be detected in both the original seismogram and in the time-frequency plane. The envelope amplitude "ridges" extending to high frequency are discrete body wave arrivals from the seismic event while the large envelope maxima at the lower frequencies are (primarily) due to the noise background.

The signal parameters are generated automatically by QHD and are derived from a set of functions associated with the time series being analyzed. In particular, at each narrow band filter frequency the envelope, or modulation function of each filter output is generated along with the instantaneous phase and frequency associated with the time series. Maxima in the envelope functions, corresponding to energy group arrival times at the frequencies

sampled by the filters, are determined by the program and this data set is plotted in the time-frequency plane; where coherent patterns formed by the measured group arrival time data define the dispersion relations for "signals" arriving within the time series being analyzed. Figure 1 illustrates the time-frequency plane for a recorded seismic event in a high noise background. One function of the pattern recognition component of the QHD program is to locate and "follow" coherent "ridges" of envelope maxima in the t-f plane, and to extract (or "isolate") those that conform to "signals" having a particular, desired, dispersion characteristic.

In addition to measuring the times of envelope maxima, the program determines both the instantaneous phase and amplitude of the envelope at the maxim. (If the time series corresponds to a spatial component of the wave field, and other components are available and are similarly processed by QHD, then the polarization is also computed at each group arrival time. The polarization, is defined to be the phase difference between the vertical and horizontal component time series, at a point of observation.) The envelope amplitude and instantaneous phase at the group arrival times are directly related to the Fourier spectral amplitude and phase. Thus, at each observed group arrival time-frequency point in the time-frequency plane a signal parameter "vector" composed of the estimated Fourier amplitude and phase, and polarization when available, is defined and "attached" to each measured group arrival time value. Thus, in addition to searching for coherent patterns of arrival time versus frequency, corresponding to those of interest to the user, the program simultaneously compares the spectral amplitude relative to noise (and the polarization of the wave field when available) to values required for the signal specified by the user. Thus, the program will perform joint dispersion "filtering", threshold detection and polarization filtering. The actual procedure fol-

lowed by the program in performing this "filtering-detection" task involves iterative pattern recognition in the time-frequency plane, wherein signal detections are "removed" (spectrally subtracted) from the time series and the whole filtering-pattern recognition procedure repeated using the residual time series. This iterative procedure is designed to combat interference effects among closely time spaced signals and/or noise "pulses".

Once a set of candidate detections of signals have been made on the basis of the criteria indicated, they are considered as a group by the program, using criteria for association of the isolated "pulses" detected, into seismic phases. In particular, if QHD obtains two or more signal detections within the time resolution range of the narrow band filters employed in the analysis, then these detections will be merged to form a single seismic phase. (Such occurrences are fairly common and are due, in part, to the multiple pattern searches using residual time series. In this case a signal can be detected more than once if it was not completely removed in the first pass.) However, the instantaneous frequency variation with time for the original time series is used to check for indications of interference within the filter "resolution time window", which may occur when two or more seismic phases are present. When significant variation of the instantaneous frequency from the filter center frequency occurs at a number of filter frequencies within the resolution time window, then the detections within the window are not merged, but are considered to be separate seismic phases.

Once the seismic phases have been defined in terms of a set of signal vectors (containing the spectral amplitude and phase) associated with a set of group arrival times, the program inverts the signal spectral information to the time domain and thereby generates waveforms for each signal identified. The program also computes the envelope functions for these wave forms and uses

the first inflection point in the envelope to estimate the first arrival time (signal arrival time) for the seismic phase. The program then provides a final list of seismic phase detections. The associated spectral variables, as well as signal timing data for each detection, are written to an output file. A separate utility program will then plot results for the user.

Program Operations and Structure

A summary of the program operations, in the order in which they are performed is as follows:

- (1) Read an input data file containing the time series to be processed.
- (2) Preprocess the time series: Bandpass filter, detrend, taper, remove spikes, etc.
- (3) Obtain a noise sample from the data record and compute, or select from an input file supplied by the user, appropriate narrow band filter parameters.
- (4) Decompose the time series into quasi-harmonic components by Gaussian narrow band filtering.
- (5) Compute associated functions, including the envelope, instantaneous phase and instantaneous frequency functions, for each filter.
- (6) Determine the times of envelope maxima and the amplitudes of the envelope functions at these maxima for each filter. Also determine the instantaneous phase values at these times. (Also compute the polarization and emergence angle of the wave field at the group arrival times, when multi-component data is processed.)
- (7) Search for and identify specified types of signals, based on pattern recognition in the time-frequency plane, having appropriate disper-

-118-

sion and signal power levels (relative to noise). (Also select only those with proper polarization and emergence angles, when multiple-component data is being processed.)

- (8) Subtract the spectral values (amplitude and phase) associated with detected signals from the time series spectrum and invert the "residual" spectrum to obtain a "residual" time series". Repeat the processing steps (4) through (8) on residual time series. (Iterative pattern recognition.) Terminate when step (7) produces no new detections or when a preselected number of such iterations have been performed.
- (9) Associate the collection of signal detections produced after exit from step (8) into a set of seismic phases, using criteria based on the resolution (or uncertainty) time of the Gaussian filters employed and the instantaneous frequency. (Termed the "culling process".)
- (10) Invert the isolated seismic phase spectra to the time domain to give wave forms and determinations of the "first motion" times of each.
- (11) List results and write output files.
- (12) Return to read a new data file or terminate run.

The actual structural elements and flow of the program operations are indicated in Figure 2. Detailed operational steps within the input/output sections and the various execution sections indicated in the diagram are described separately in the Users Guide to QHD and in the QHD Program Operations Manual.

Examples of QHD Analysis Results

Applications of the QHD analysis approach to both observed and synthetically produced seismic time series provide the best means of evaluating the

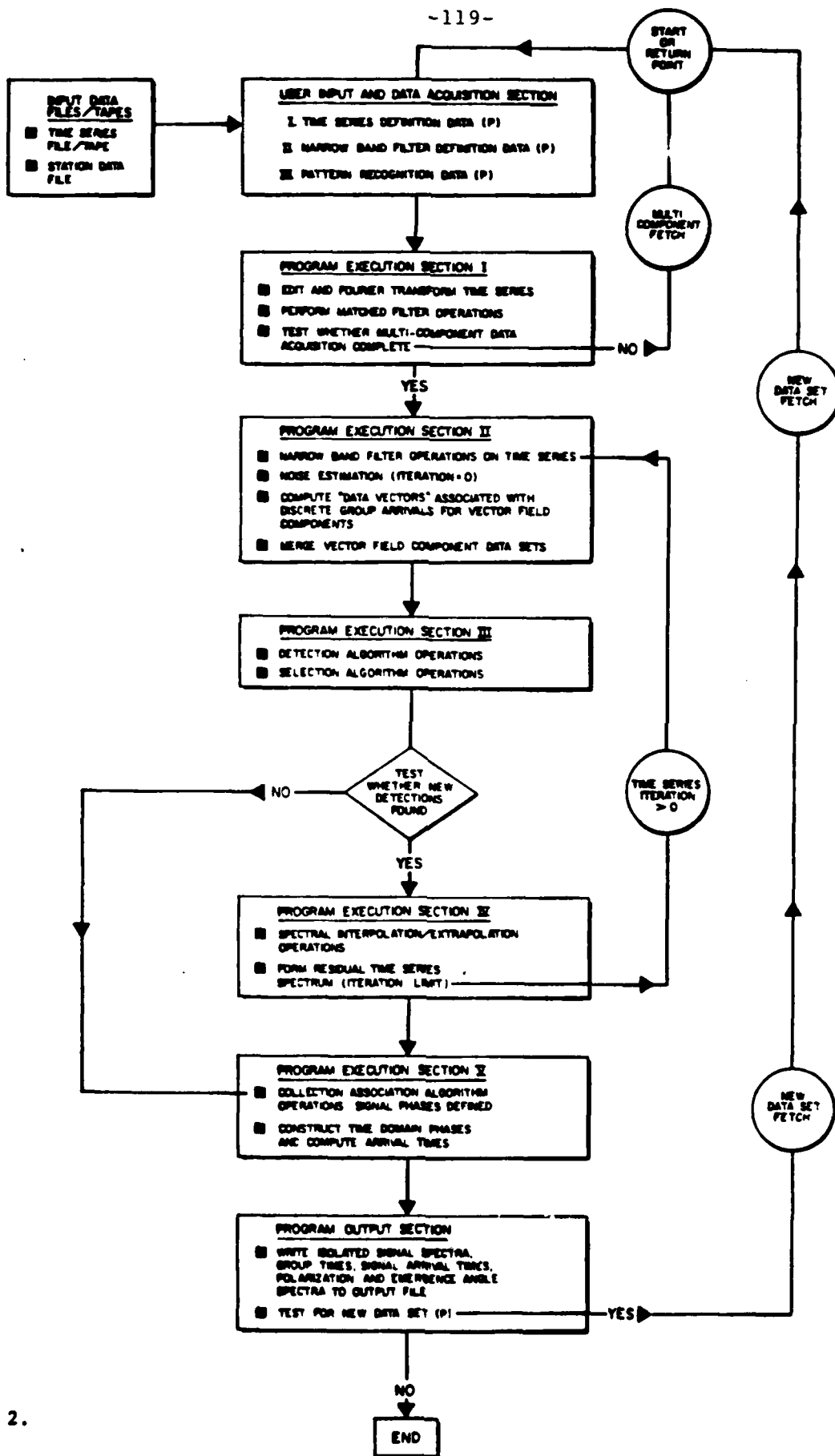
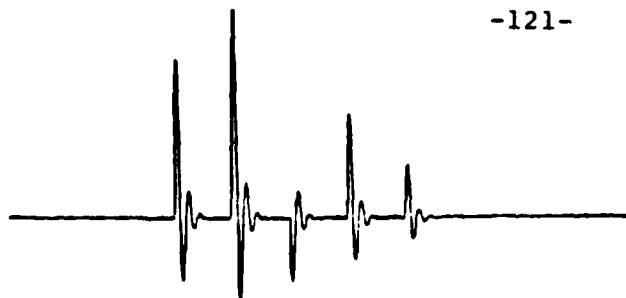


Figure 2.

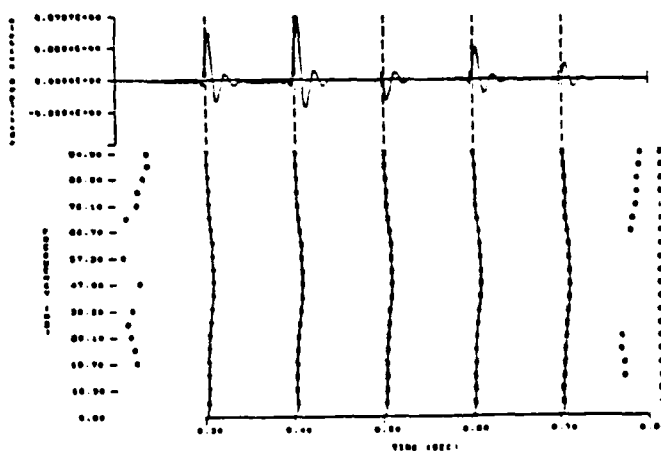
entire "filtering-pattern recognition" approach used in this program. With applications to synthetic "data" we can systematically (and quantitatively) determine the accuracy and sensitivity of the method as a function of noise and signal properties using entirely known signal input which can closely approximate real seismic data. On the other hand, since observed seismic data can differ from synthetic data in many (unknown) ways, it is also important to test and evaluate the method using a variety of observed data. Usually this involves interpreting the results of the processing in the context of what is known about the source and path of propagation. For example, large explosions observed at regional and teleseismic distances can produce relatively simple seismograms, with signal arrival times that are predictable with fair accuracy. In these cases the QHD results can be compared with expected arrival times, wave forms and spectra of the most prominent seismic phases from these more "controlled events and "known" paths, to evaluate performance. Similar statements apply to reflection seismograms from explosions or vibrator sources recorded in "test areas" where the seismic velocity structure is reasonably well known.

The following figures provide some examples of QHD processing for both synthetic and observed data. These examples constitute only a very small and incomplete part of the systematic testing which is required for a full evaluation. These examples are actually only meant to demonstrate the kind of tests performed and the general nature of the results obtained for a range of "data"; from simple pulse synthetics to very complex observed earthquake data. They also graphically illustrate the steps in the processing and the nature of the output obtained.

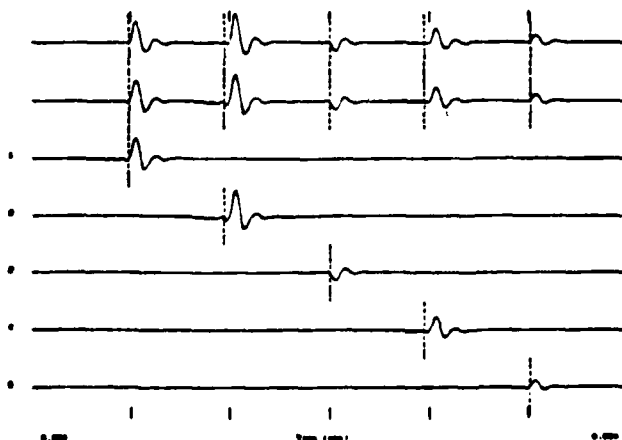
Figure 3 illustrates results of QHD analysis of a sequence of fairly closely spaced seismic pulse synthetics, in a background of random noise. As Figure



Five synthetic pulses (damped sinusoids), separated by .1 sec, with random noise superposed.



QHD generated time-frequency plane. Amplitude of group arrivals are indicated by numerical values in the t-f plane. Larger numbers indicate larger amplitudes with stars denoting the largest. The program automatically detects the five undispersed signals and indicates the time of the first arriving energy for each.



Time domain synthesis of the QHD estimated undispersed signal spectra (traces labeled 1 through 5). Top trace is the original sequence of five synthetic pulses, the second trace is the sum of the five QHD isolated pulses.

Figure 3a. A simple test example of QHD signal isolation using single component synthetic data. The signal pulses have maximum power near 40 Hz. and approximate pulse forms generated in exploration seismic surveys. The QHD pattern recognition in the time-frequency plane uses threshold detection combined with "dispersion filtering" to automatically isolate the five undispersed signal pulses.

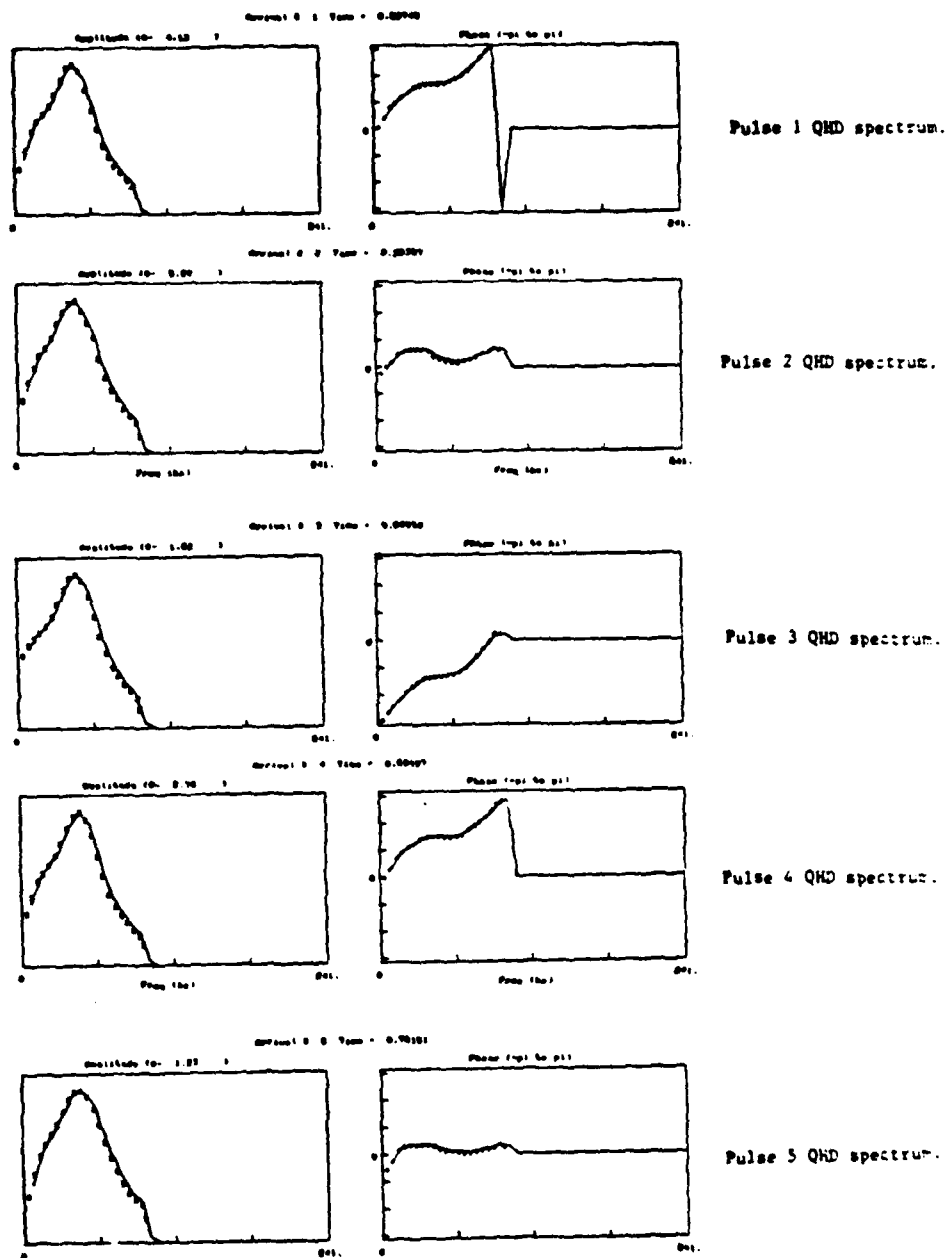


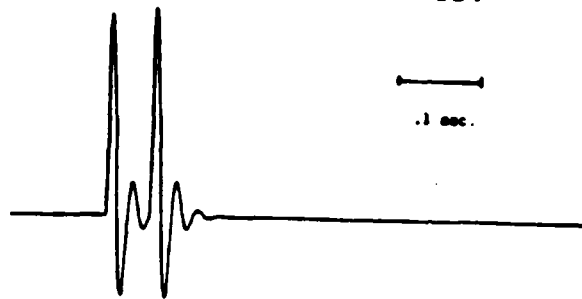
Figure 3b. Spectral estimates of each of the five isolated test pulses. The QHD spectral amplitude estimate is very close to the known Fourier amplitude, while the phase is sometimes less accurately determined but, nevertheless, with sufficient accuracy to yield time domain reconstructions that are very close to the original time domain pulses.

3a shows, in a low noise environment such as this, the isolation of multiple non-overlapping undispersed pulses is accomplished with high accuracy by QHD pattern recognition in the time-frequency plane, and the automatic timing of the pulse arrivals is quite accurate. Figure 3b shows the spectral estimation of each of the five pulses, obtained from the amplitudes of the envelope functions at their maxima in the t-f plane and the instantaneous phase values at the times of these maxima. As noted in the figure caption, the spectral phase is not as accurately determined as the spectral amplitude. In the frequency range around the spectral maximum, however, the phase values are quite accurate and hence the time domain wave forms generated from these spectral estimates closely match the original pulses.

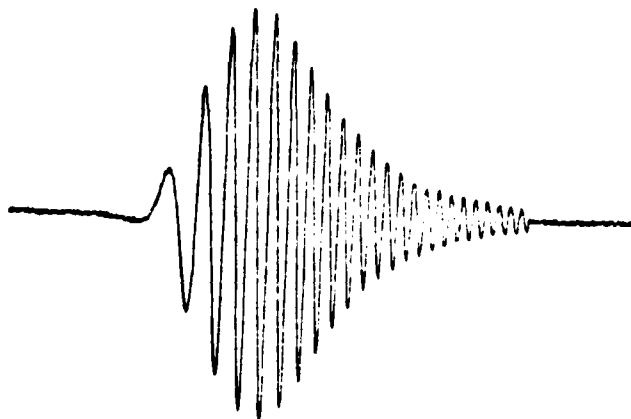
Figure 4 illustrates QHD isolation of two overlapping pulses in a high noise background. In this example the noise is non-random, having the dispersive structure of a seismic Rayleigh wave. Figure 4a shows the QHD determined dispersion of the synthetic Rayleigh wave. Figure 4b shows the isolation of the two pulses, by the QHD "dispersion filtering". In this moderately demanding test case the arrival times of the pulses are very well determined, while the spectral estimates, and the wave forms generated from them, are somewhat distorted due to interference between the two pulses themselves, as well as from the Rayleigh wave. (No analytical corrections were made for interference in this example.)

Figure 5 shows a similar example, with five variable amplitude pulses distributed throughout the Rayleigh wave signal train. As can be seen from the patterns in the time-frequency plane, the Rayleigh wave strongly distorts the pulse dispersion. However, the pattern recognition procedure employed nevertheless accurately identifies and times all the pulses. It can also be seen that the spectral estimates and associated wave forms, while resembling the

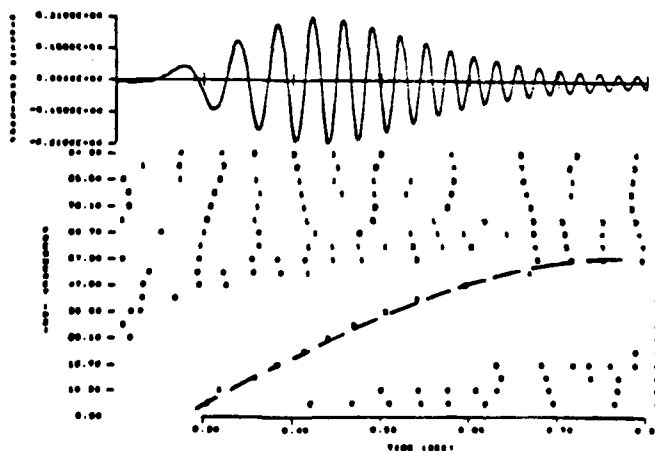
-124-



Two synthetic pulses (damped sinusoids) separated by .05 sec.

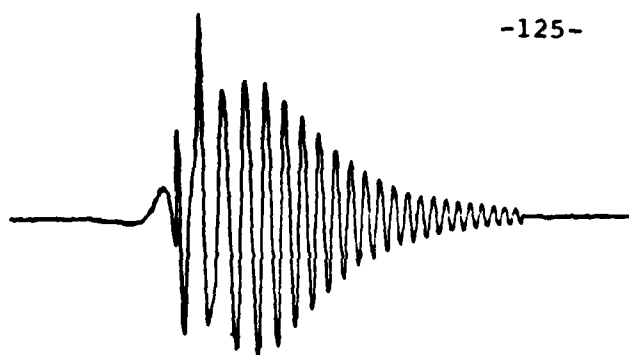


Inversely dispersed Rayleigh surface wave with noise (maximum amplitude near 30 Hz).

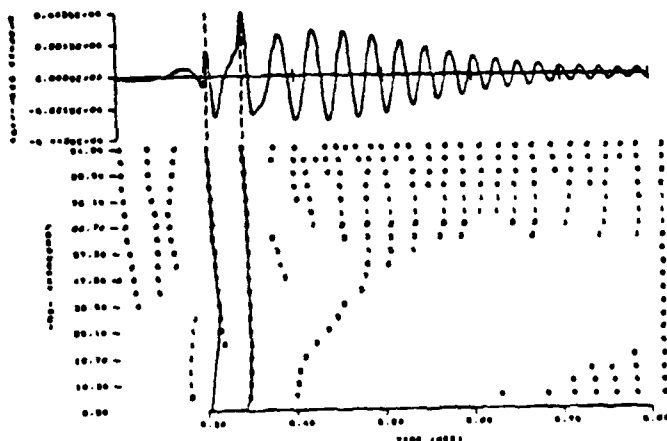


QHD generated time-frequency plane. Amplitude of group arrivals are indicated by numerical values in the $t-f$ plane. Larger numbers indicate larger amplitudes. Stars are the largest. Dispersion of the surface wave is shown.

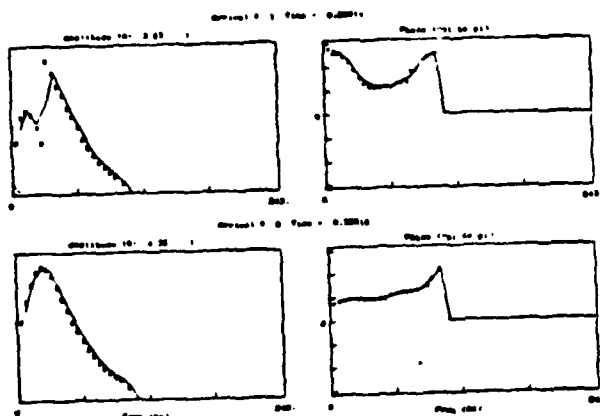
Figure 4a. Example of the isolation of two closely spaced body wave signal pulses in a Rayleigh type surface wave background. The pure (unmixed) signals are shown, along with the QHD generated time-frequency plane results for the pure Rayleigh wave.



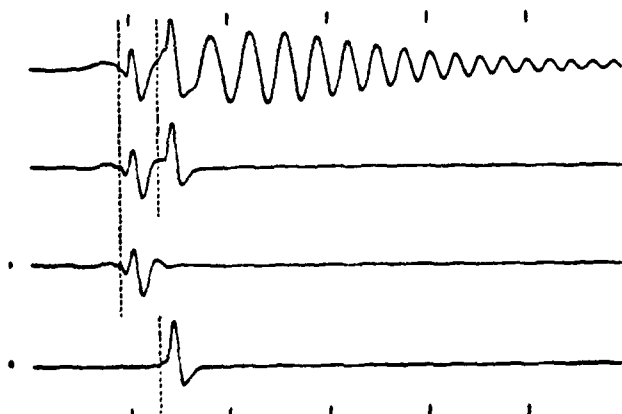
Sum of synthetic pulses and surface wave.



QHD generated time-frequency plane for composite time series. The original composite time series is shown at the top. Undispersed pulses are isolated, as shown, by the QHD pattern recognition method in the time-frequency domain.



Spectral estimates obtained by QHD for the isolated pulse signals.



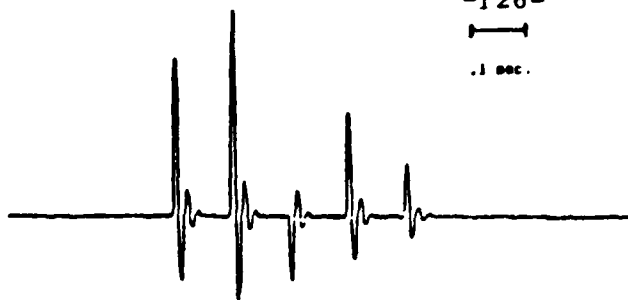
Time domain synthesis of the QHD estimated undispersed signal spectra (traces labeled 1 and 2). Top trace is original composite time series, second trace is the sum of the two QHD isolated pulses.

Figure 4b. Results of QHD analysis of the body wave plus surface wave time series. The QHD analysis was designed to isolate each body wave pulse.

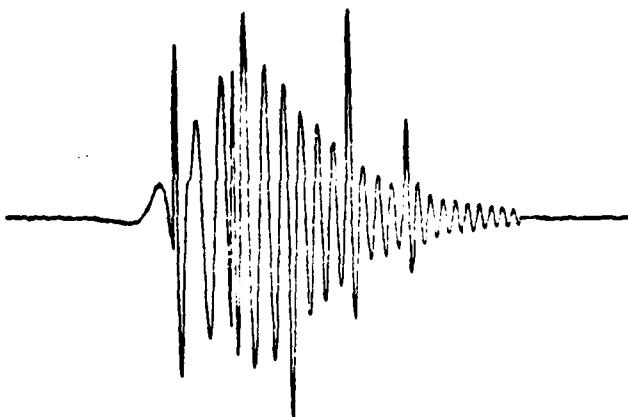
-126-



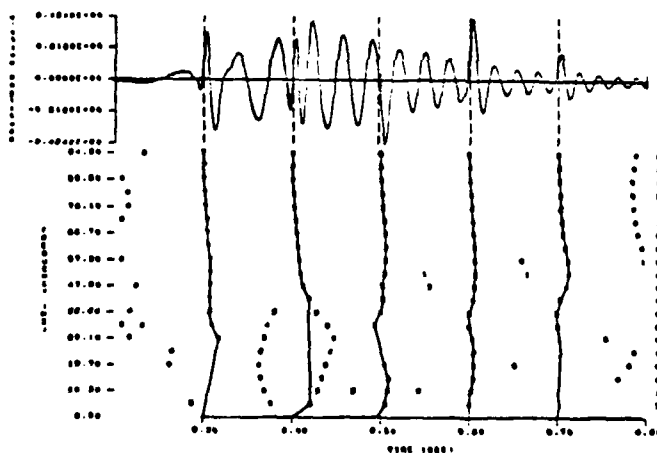
.1 sec.



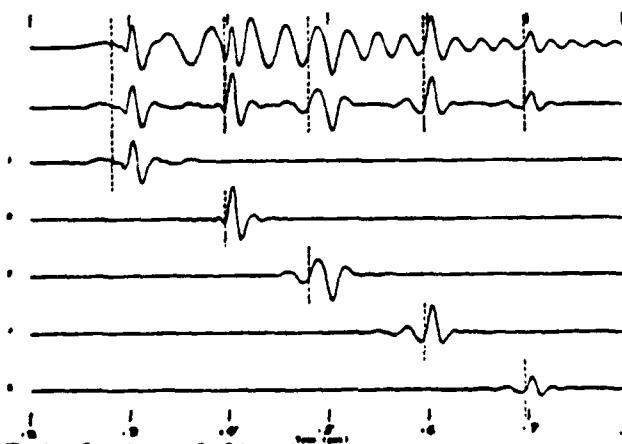
Sequence of undispersed synthetic pulses separated by .1 sec.



Superposition of dispersed surface wave and the five pulse sequence.



QMD generated time-frequency plane for composite time series. The original composite time series is at the top. The five undispersed pulses are detected, as shown, by the QMD pattern recognition method in the time-frequency plane.



Time domain synthesis of the QMD estimated spectra of each of the five pulses detected. The isolated undispersed signals detected are shown in the traces labeled 1 through 5. The top trace is the original composite time series, the second trace is the sum of the QMD isolated pulse.

Figure 5. QMD isolation of five body wave pulses immersed in a dispersed Rayleigh wave background.

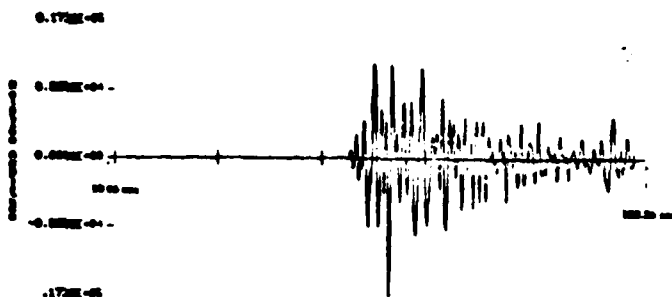
originals reasonably well, are somewhat distorted by the Rayleigh wave "noise".

Figure 6 provides a reasonably complete example of the application of the QHD automated analysis to a complex teleseismic earthquake. In particular, this example illustrates (1) the automated selection of Gaussian narrow band filters (which is based on the event signal to noise ratio as a function of frequency) in Figure 6a; and (2) the iterative pattern recognition in the time-frequency plane, in Figure 6b. All of these results, in Figures 6a through 6d are part of the standard output from the program and serve to provide a user with a good mean of evaluating the final results, which are the spectral and timing information in Figure 6c and/or the isolated wave form results in Figure 6d.

The final example, in Figure 7, is an application of this analysis method to a relatively "high" frequency (0-20 Hz) regionally recorded earthquake. In this example, as can be seen simply from the original time series in Figure 7a, the noise level is higher than in the previous example. The "event" is also very complex, consisting of many closely spaced seismic phases resulting from variable energy radiation from the spatially finite source itself, plus multiple arrivals due to many strong reflectors and refractors at depth between the source and receiver. Here again, many of the important QHD program operations enumerated in the previous section are illustrated, in particular the pattern recognition operations which are shown in Figures 7b and 7c.

The most important observation to be made regarding this method is that the QHD signal isolation provides individual spectral information for each coherent signal within the complicated event wave train and thereby allows rapid, quantitative analysis for path and source properties to be undertaken. The confidence which one may place in the signal identifications, timing and spectral estimates is directly proportional to the accuracy of the method when

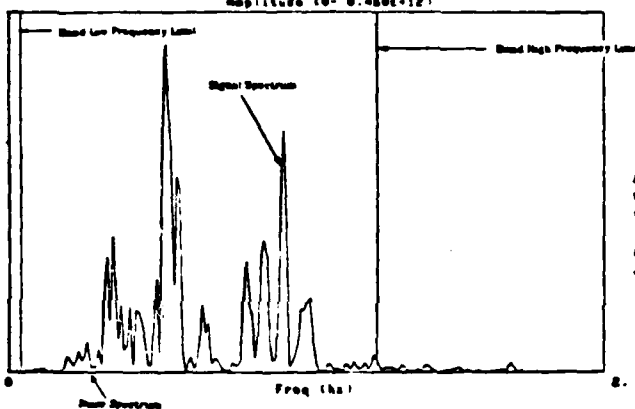
00000 Station - STP (short period 2)
Δ = 1000 km



Short Period teleseismic signals from an earthquake. The compressional wave train is shown.

00000 Station - STP (short period 2)
Δ = 1000 km

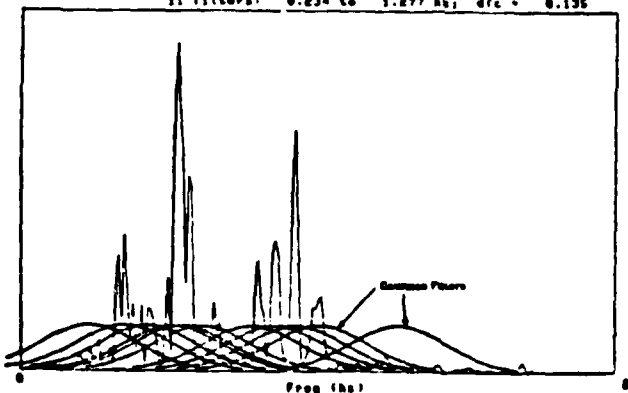
Signal vs. Noise Spectra
Amplitude (0- 0.480E-12)



Amplitude spectra from a long signal window, consisting of the entire P wave train, and a long noise sample. The frequency band within which QHD spectral analysis is to take place is indicated, and is automatically set by the program.

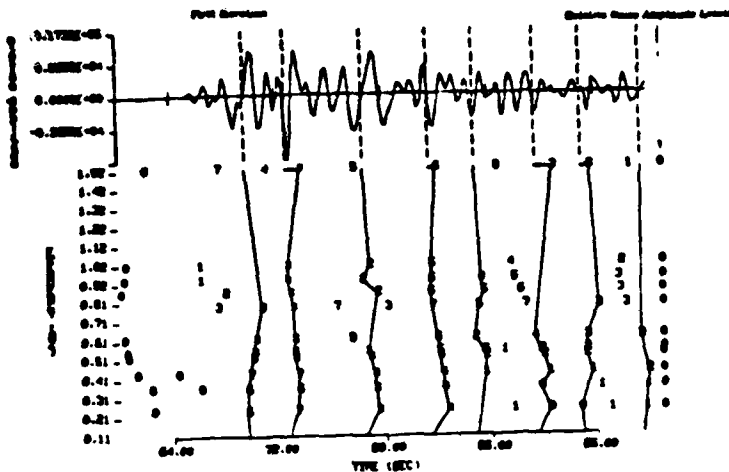
00000 Station - STP (short period 2)
Δ = 1000 km

Filters plotted against Signal
11 filters: 0.234 to 1.277 Hz; drc = 0.135

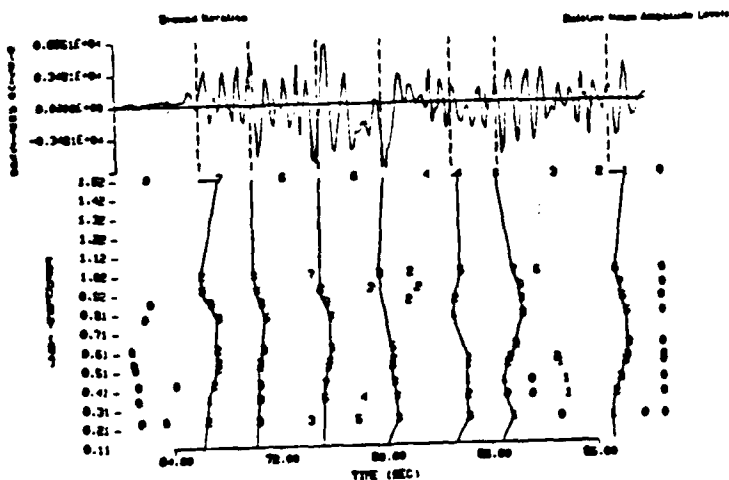


Distribution of Gaussian filters that have been automatically designed and distributed within the frequency band selected by the program.

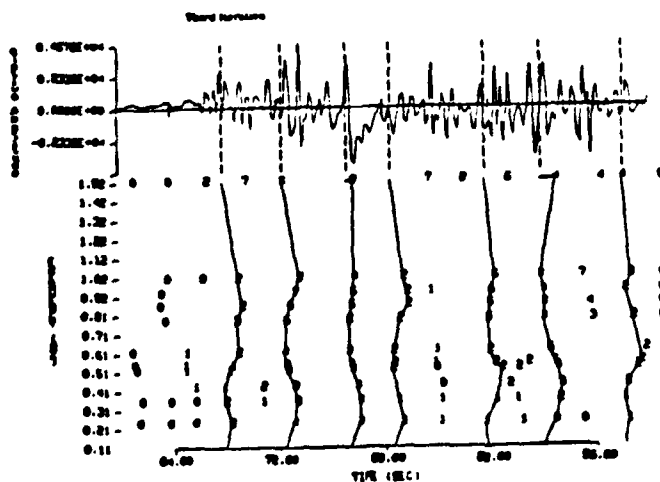
Figure 6a. Example of the sequence of QHD operations applied to teleseismic data.
(a) Design of the Gaussian filters.



QND generated time-frequency plane data, with isolated "arrivals", corresponding to undispersed signal pulses. The original time series (shown at the top) is processed in this "first iteration", with the spectral estimates obtained for body wave arrivals to be subtracted from this original time series to generate "residual" time series, which will again be searched by the program for undispersed signals.

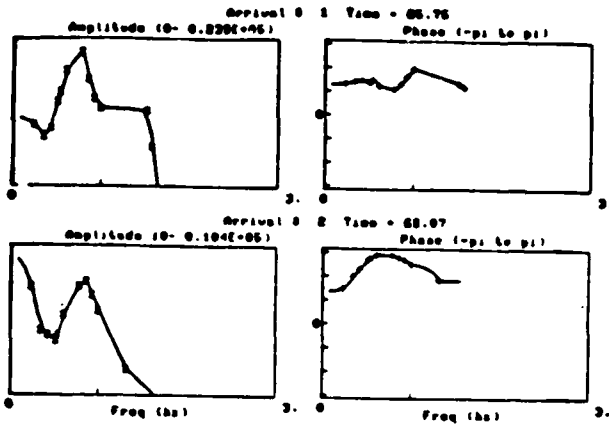


QND generated time-frequency plane data for the second iteration residual-time series from which previously detected "signals", isolated in the first detection iteration, have been (spectrally) removed.



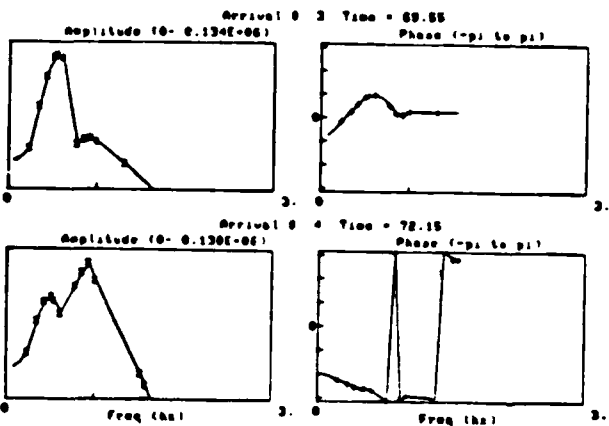
QND generated time-frequency plane data for the third iteration time series from which previously detected "signals", isolated in the first and second detection iterations, have been removed.

Figure 6b. QND operations applied to teleseismic data. (b) Iterative pattern recognition in the time-frequency plane.



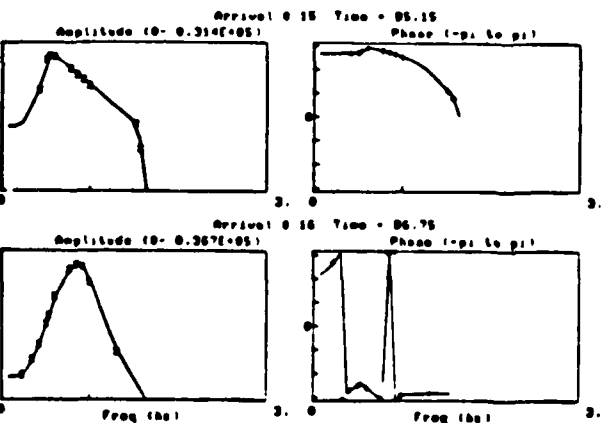
Pulse 1 QHD spectral estimate (amplitude and phase)

Pulse 2 QHD spectral estimate (amplitude and phase).



Pulse 3 QHD spectral estimate (amplitude and phase).

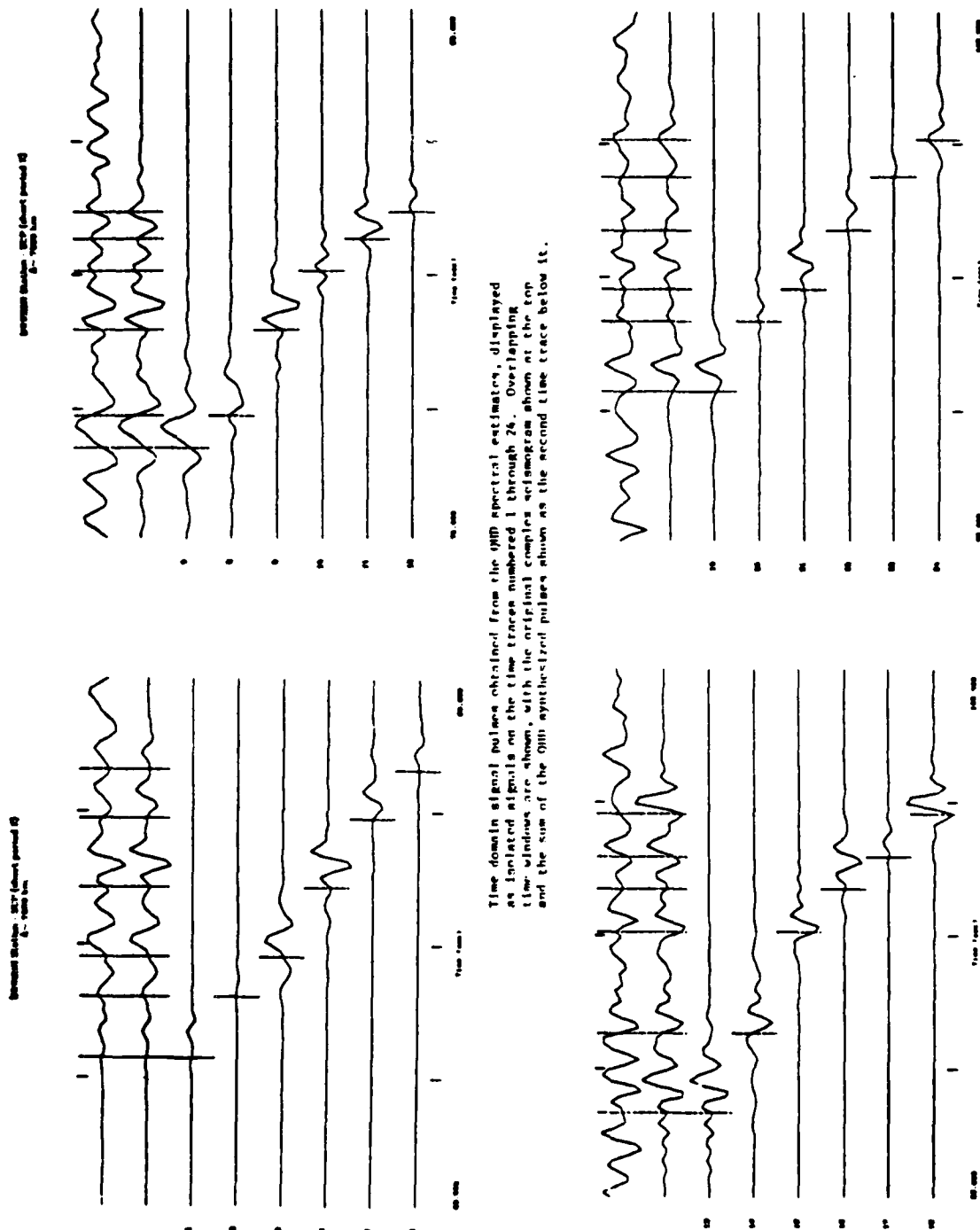
Pulse 4 QHD spectral estimate (amplitude and phase).

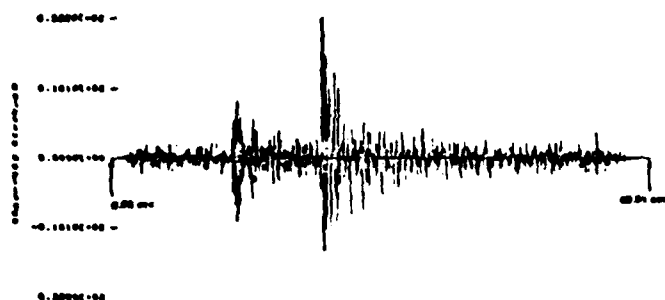


Pulse 15 QHD spectral estimate (amplitude and phase).

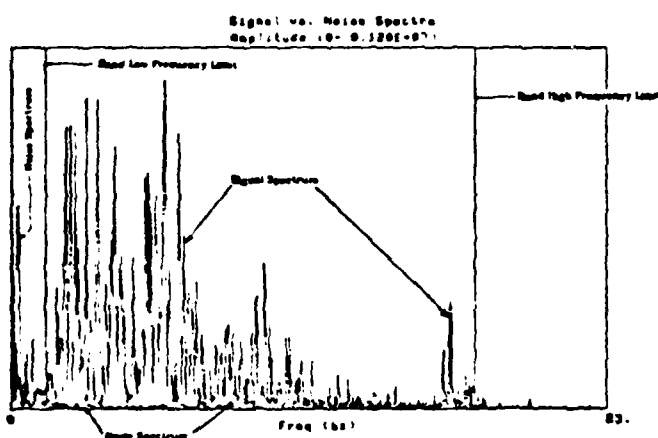
Pulse 16 QHD spectral estimate (amplitude and phase).

Figure 6c. QHD operations applied to teleseismic data. (c) Examples of QHD spectral estimates for isolated body wave (P) signals.

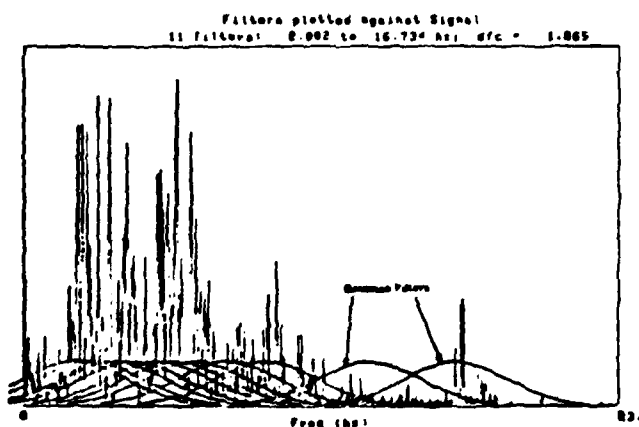




Short period near field signals from a Southern California earthquake. The entire signal wave train from the event is shown, with complex P and S wave trains indicated by the prominent bursts of energy beginning near 18 and 25 seconds, respectively.

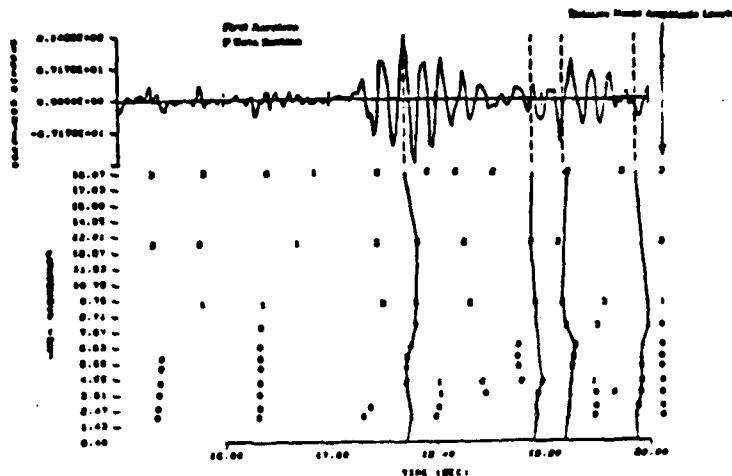


Signal and noise amplitude spectra. The signal spectrum shown corresponds to the spectrum for the entire event. The noise spectrum is generated from a long time window of noise preceding the event. Vertical lines indicate the frequency band selected by the program for QHD analysis.

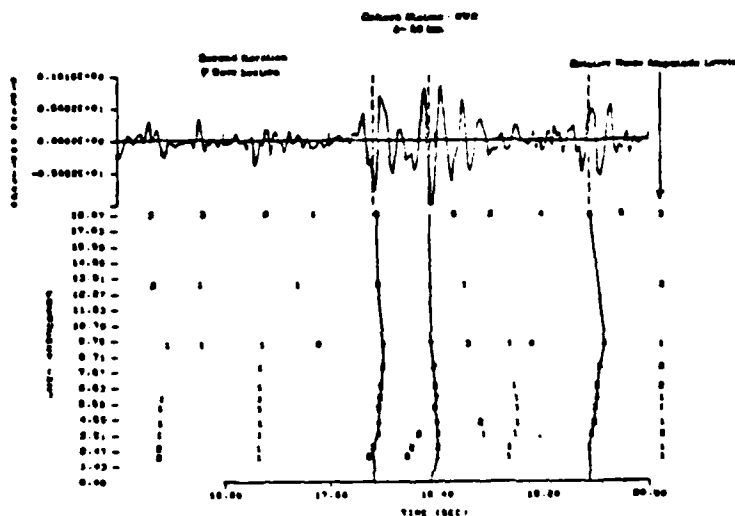


Automatically determined distribution of Gaussian filters, centered within the program selected frequency band, to be used in the QHD processing.

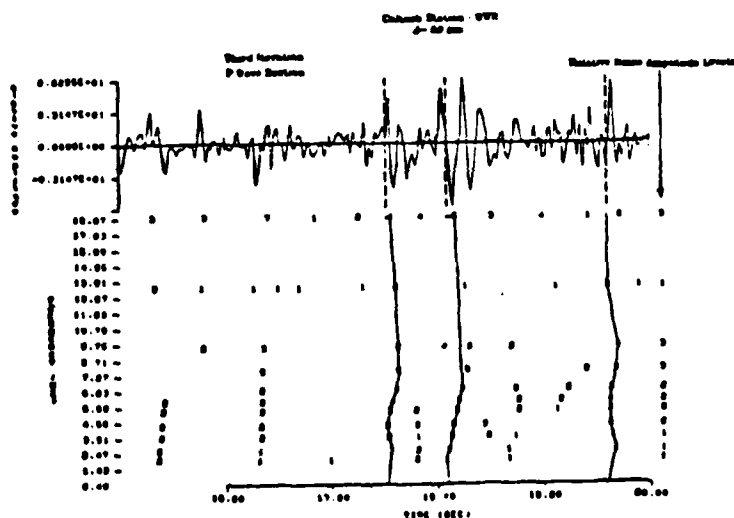
Figure 7a. Example of the sequence of QHD operations applied to complex regional distance range seismic data from an earthquake. (a) Design of the Gaussian filters.



QND generated time-frequency plane data, with isolated P wave "arrivals", corresponding to undispersed signal pulses. The original time series (shown at the top) is processed in the "first iteration", with the spectral estimates obtained for the P wave arrivals to be subtracted from this original time series to generate "residual" time series, which will again be searched by the program for undispersed signals.

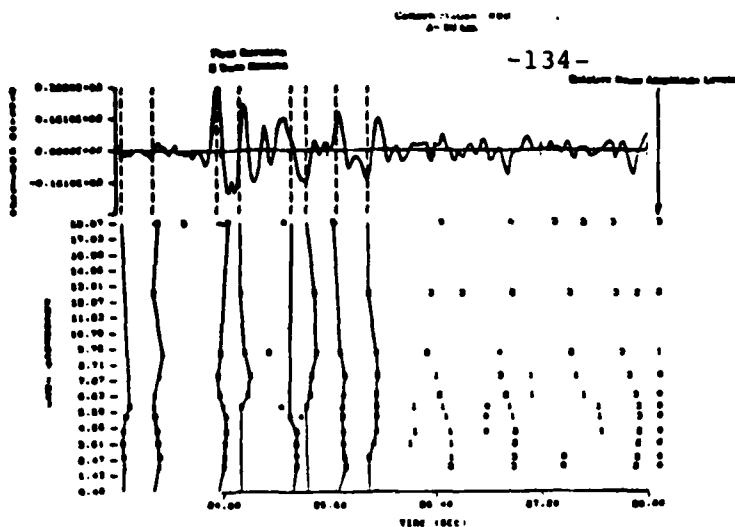


QND generated time-frequency plane data for the second iteration residual time series from which previously detected P wave "signals" isolated in the first detection iteration, have been (spectrally) removed.

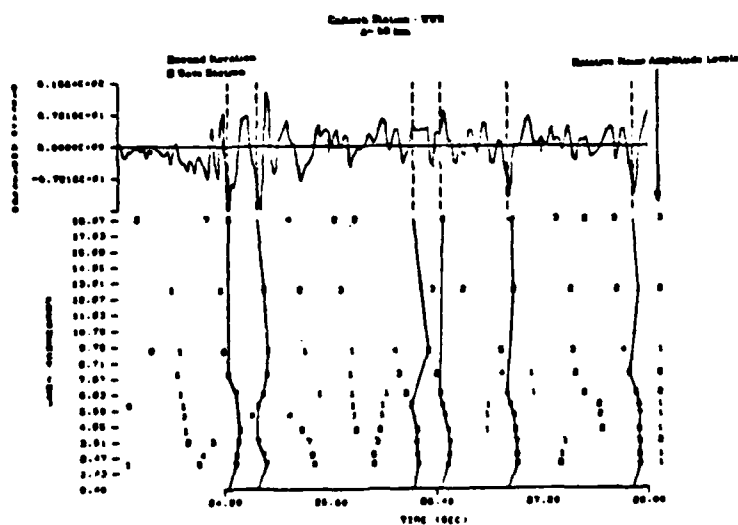


QND generated time-frequency plane data for the third iteration time series from which previously detected P wave "signals", isolated in the first and second detection iterations, have been removed.

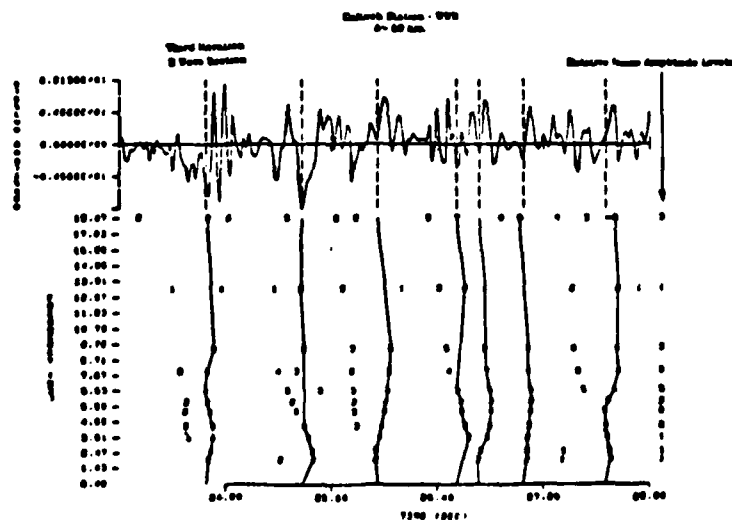
Figure 7b. QND operations applied to regional earthquake data. (b) Iterative pattern recognition in the time-frequency plane (P wave section).



QHD generated time-frequency plane data, with isolated S wave "arrivals", corresponding to undispersed signal pulses. The original time series (shown at the top) is processed in the "first iteration", with the spectral estimates obtained for the S wave arrivals to be subtracted from this original time series to generate "residual" time series, which will again be searched by the program for undispersed signals.



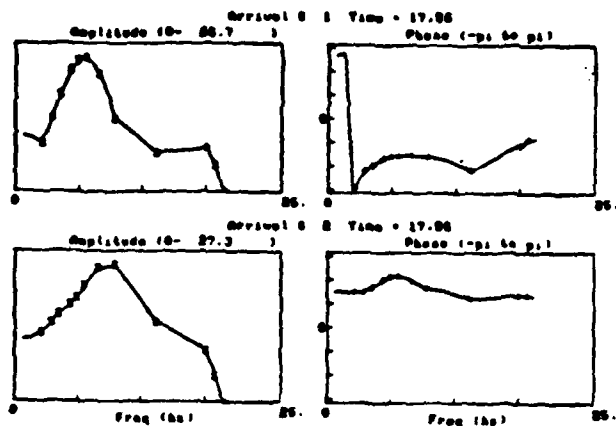
QHD generated time-frequency plane data for the second iteration residual time series from which previously detected S wave "signals" isolated in the first detection iteration, have been (spectrally) removed.



QHD generated time-frequency plane data for the third iteration time series from which previously detected S wave "signals", isolated in the first and second detection iterations, have been removed.

Figure 7c. QHD operations applied to regional earthquake data. (c) Iterative pattern recognition in the time-frequency plane (S wave section).

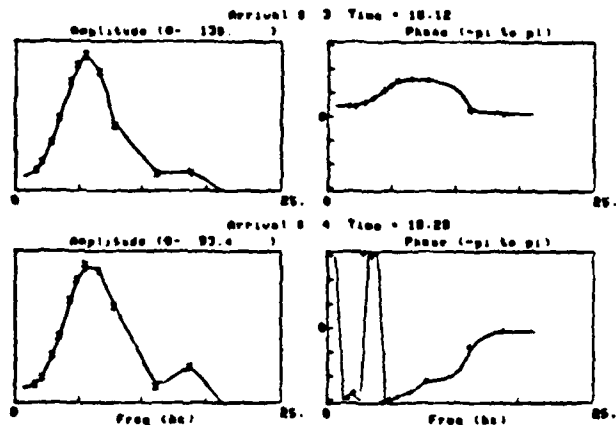
Station Name: 004
0-10 Hz



Pulse 1 QHD P wave spectral estimate (amplitude and phase).

Pulse 2 QHD P wave spectral estimate (amplitude and phase).

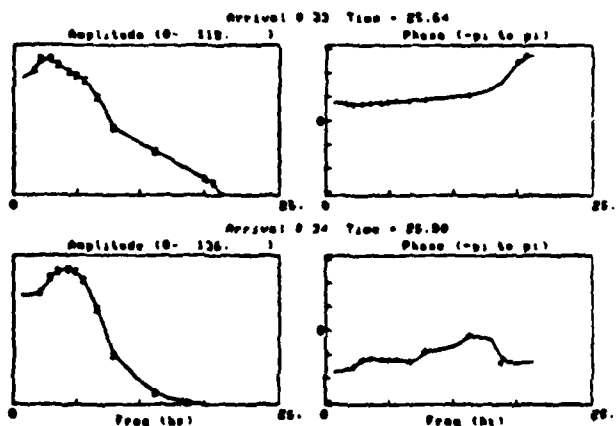
Station Name: 004
0-10 Hz



Pulse 3 QHD P wave spectral estimate (amplitude and phase).

Pulse 4 QHD P wave spectral estimate (amplitude and phase).

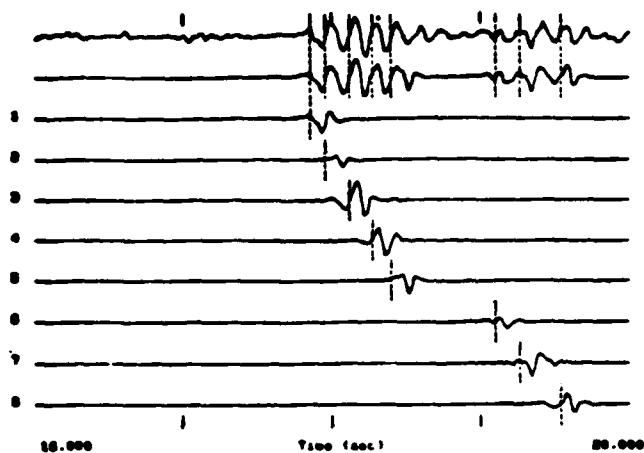
Station Name: 004
0-10 Hz



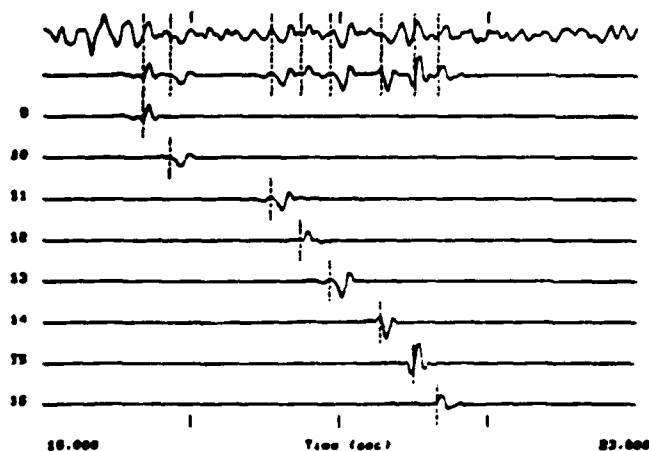
Pulse 33 QHD S-wave spectral estimate (amplitude and phase).

Pulse 34 QHD S-wave spectral estimate (amplitude and phase).

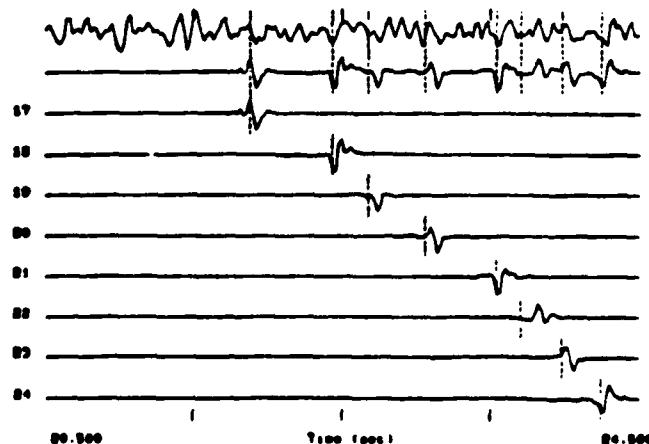
Figure 7d. QHD operations applied to regional earthquake data. (d) Examples of QHD spectral estimates for isolated body wave signals (P and S waves).



Time domain signal pulses obtained from the QHD spectral estimates for the earliest arriving P wave signals from the event. Top trace is the original time series, the second trace is the sum of the QHD isolated P waves shown in the traces labeled 1 through 8.



Later time section of the P wave signal train (with some time overlap with that shown above).



End of the P wave train showing isolated late arriving P waves.

Figure 7e. QHD operations applied to regional earthquake data. (e) Time domain signal pulse estimates.

applied systematically to synthetic "data", such as that illustrated in Figures 3, 4 and 5, and similarly when applied to observed data from tests under controlled conditions. In addition however, the closeness of the reproduction of the original time series by the summation of the coherent signals obtained by the QHD analysis is clearly indicative of the accuracy and validity of the results, even though the signal content of the original time series may be uncertain or unknown. As illustrated in Figure 7e (and in Figure 6d) the sum of the isolated signals does closely approximate the original event time series, so that a reasonable degree of confidence can be attached to the detailed results. With additional systematic testing and extensive applications in the future it should be possible to rigorously quantify this degree of confidence.

References

- Alexander, S. S. (1963), Surface wave propagation in the Western United States, Ph.D Thesis, California Institute of Technology, 241 pages.
- Archambeau, C. B., J. C. Bradford, P. W. Broome, W. C. Dean, E. A. Flinn and R. L. Sax (1965), Data Processing techniques for the detection and interpretation of teleseismic signals, *Proceedings of the IEEE*, vol. 53, no. 12, December, pp. 1860-1884.
- Archambeau, C. B. and E. A. Flinn (1965), Automated analysis of seismic radiation for source characteristics, *Proceedings of the IEEE*, vol. 53, no. 12, December, pp. 1876-1884.
- Archambeau, C. B., M. Schnapp, R. Goff, J. M. Savino, J. F. Masso and K. Hamilton, Methods of seismic signal detection and analysis based on Quasi-Harmonic Decomposition (QHD), submitted to *J. Roy. Astron. Soc.*, 1982.
- Cara, M. (1973), Filtering of dispersed wave trains, *Geophys. J. R. Astr. Soc.*, 33, pp. 6580.
- Denny, M. D. and R. C. Y. Chin (1976), Gaussian filters for determining group velocities, *Geophys. J. R. Astr. Soc.*, 45, pp. 495-525.
- Dziewonski, A., S. Block and M. Landisman (1969), A technique for the analysis of transient seismic signals, *BSSA*, 59, no. 1, pp. 427-444.
- Dziewonski, A., J. Mills and S. Block (1972), Residual dispersion measurement - A new method of surface wave analysis, *BSSA*, 62, pp. 129-139.
- Instron, H. H., P. D. Marshall and C. Blamey (1971), Optimization of filter bandwidth in spectral analysis of wavetrains, *Geophys. J. R. Astr. Soc.*, 23, pp. 243-250.

Appendix 1

GLOSSARY OF SYMBOLS, ABBREVIATIONS AND TERMINOLOGY

Transfer Functions: Spectrum (amplitude and phase) of the impulse response of a filter. Used to define response of both sensor system and wave propagation in the earth. (Each wave type has a different transfer function.)

Quasi-Harmonic Signal Decomposition (QHD): Literally, the separation or decomposition of a time series into a set of nearly harmonic (or "quasi-harmonic") components, from which the envelope, instantaneous phase, frequency and polarization time series are generated. Functionally, narrow-band filters are used to generate nearly harmonic output at discrete frequencies (i.e., in narrow frequency bands), from which associated filter envelope functions; instantaneous phase, frequency and polarization, can be computed as functions of time at the discrete set of filter frequencies.

Matched Filtering: Cross correlation of an expected or sought for signal with a recorded time series, with a "detection" corresponding to a pulse (peak) in the correlation time series. In general: the operation of correlation of expected or sought for signal properties with "observed" properties of a time series.

Pattern Recognition: Search procedure, usually in two or more dimensions within a parameter space, aimed at the selection or detection of a series, or pattern, of parameter values that are characteristic of a signal. The matched filter concept and methods are often used for selection or detection of sought for signal within the parameter space.

Dispersion: General term referring to the variation of group velocity (or group arrival time) as a function of frequency or the variation of phase velocity, or phase arrival time, as a function of frequency.

"NBF" - Narrow-Band Filter: Narrow-band filter, usually of Gaussian type with transfer function:

$$G(\omega - \omega_j) = \frac{1}{\Delta\omega_j} \sqrt{\frac{\beta}{\pi}} \exp \left[-\frac{\beta}{2} \left(\frac{\omega - \omega_j}{\Delta\omega_j} \right)^2 \right]$$

where $\beta = \ln 2 / 2$. Here $Q_j^{-1} = \Delta\omega_j / \omega_j$, is the filter quality factor, with $\Delta\omega_j = 2\pi\Delta f_j$ equal to one half the frequency bandwidth at the half power points, and ω_j representing the center frequency of the j th filter ($j = 1, 2, \dots$) from a set of such filters.

Gaussian Filter Resolution Time, Δt : The time interval between two signal pulses that is generally required for the complete time resolution of the signals

in the narrow band filtered output. For a Gaussian filter, of half bandwidth $\Delta\omega$ at the filter half power points, then $\Delta t \Delta\omega \approx 1/2$.

NBF-Signal, $s(t;f_j)$, and NBF-Quadrature Signal $\hat{s}(t;f_j)$: The NBF signal corresponds to the direct output of the filter (inverse Fourier transform of the product of the signal spectrum and the filter transfer function or the time convolution of the signal time series and the impulse response of the filter) while the quadrature NBF-signal corresponds to the Hilbert transform of the filter output, that is the output signal shifted in phase by $\pi/2$. The quadrature signal may be obtained by multiplying the signal spectrum by $\exp[-i \operatorname{sgn}(\omega)\pi/2]$, followed by multiplication of this by the filter transfer function and inverse Fourier transforming the result.

Analytic (or complex) NBF-signal, $s_c(t;f_j)$: Complex signal representation formed from the NBF signal and quadrature signal; $s_c(t;f_j) = s(t;f_j) + i\hat{s}(t;f_j)$. Viewed in the complex signal plane (looking down the time axis) a vector from the origin to a point on y_c describes the "instantaneous phase" of the signal by the angle it makes with the real y_c axis. The rate of rotation of the vector about the origin, with time, describes the time rate of phase change or the "instantaneous frequency."

Envelope or Modulation Function, $E(t;f_j)$: Filter envelope (or modulation) function, equal to the values of the extreme variations of the narrow-band filtered time series. The envelope, or modulation function, is formed as a time series from the filtered signal time series, $s(t;f_j)$, and its quadrature time series, $\hat{s}(t;f_j)$ using: $E = [s^2 + \hat{s}^2]^{1/2}$. The envelope function is equal to the magnitude of the analytic signal.

Group Time, $t_g(f_j)$: Group (or energy) arrival time corresponding to the time of a peak in the filter envelope function $E(t;f_j)$ for a "NBF" filter with center frequency f_j . The group velocity $U(f)$ is the velocity at which energy is propagated, and is proportional to the source to receiver distance divided by t_g .

Group Spectrum, $A_g(f_j)$: Envelope amplitude at a maximum point, occurring at the group time $t_g(f_j)$. This amplitude is very nearly equal to the Fourier spectral amplitude of a signal at the frequency f_j for a properly designed (Gaussian) filter.

Instantaneous Phase, $\phi(t;f_j)$: Computed at each time point as the inverse tangent of the ratio of the quadrature NBF signal to the actual NBF signal. At a group time, t_g , it is very nearly equal to the Fourier phase of the signal.

Instantaneous Frequency, $\Omega(t;f_j)$: Corresponds to the time rate of change of the instantaneous phase, $\Omega = d\phi/dt$. Its value, for a NBF output, will be close to the center of frequency of the particular filter output, except at times when two signal pulses interfere, at which time it may have, essentially, any value.

Instantaneous Polarization, $P(t;f_j)$: Defined as the instantaneous phase difference between two spatial components of the vector displacement (or velocity or acceleration) field; for example: $P_{ZR}(t;f_j) = \varphi_Z(t;f_j) - \varphi_R(t;f_j)$ for the vertical (Z) and radial (R) vector components. Only the value at the group arrival time for a signal is a good approximation to the signal polarization or particle motion.

Time Varying Apparent Emergence Angle, $\bar{e}(t;f_j)$: Apparent wave number vector orientation in the vertical plane to the earth's surface, at a receiver point. The emergence angle is defined as the angle between the upward vertical and the wave number vector, where $|\underline{k}| = 2\pi/\lambda$, with λ = wavelength. The apparent emergence angle is computed from the observed horizontal displacement amplitude, A_H , and the vertical displacement, A_Z , as: $\bar{e} = \tan^{-1} [A_Z/A_H]$. The true emergence angle, e , is related to \bar{e} and can be computed from it when the elastic properties of the surface material at the receiver point are known. The amplitudes A_H and A_Z are the appropriate group spectral values, $A_g(f_j)$.

Deterministic "Noise" Correction, δA_N : Correction applied to a particular signal group spectral amplitude $A_g(f_j)$, computed from other nearby group arrivals, which can be noise or other (interfering) signal arrivals. The correction is computed analytically using the first order theoretical response of a narrow band Gaussian filter to pulse like signal input. The corrected group spectral value is $A_g^* = A_g + \delta A_N$, where δA_N is algebraic and complex.

Statistical Noise correction, ΔA_N : Noise related uncertainty estimate applied to the signal amplitude spectrum, i.e., $A_g^{**} = A_g^* \pm \Delta A_N$. This uncertainty estimate, at a particular frequency, is taken to be equal to the mean noise level, $A_N(f)$, times the probability, P_N , of occurrence of an unresolved noise pulse. For an NBF time series P_N is taken to be equal to the number of noise pulses occurring per unit time, times twice the resolution time, Δt , of the narrow band filter. Thus, $\Delta A_N = \bar{A}_N(f) \cdot P_N = 2\Delta t \left[\frac{N}{T_0} \right] \cdot \bar{A}_N$ where N are the total number of noise arrivals in a sample time segment T_0 .

Signal Arrival Time ("Time of First Motion"), t^* : The time of onset of a signal pulse. Corresponds to the travel time associated with a "Signal velocity" or, equivalently, with the ray theoretic arrival time.

Appendix

**P Wave Amplitude Variations at WWSSN
Stations in the U. S. and Canada**

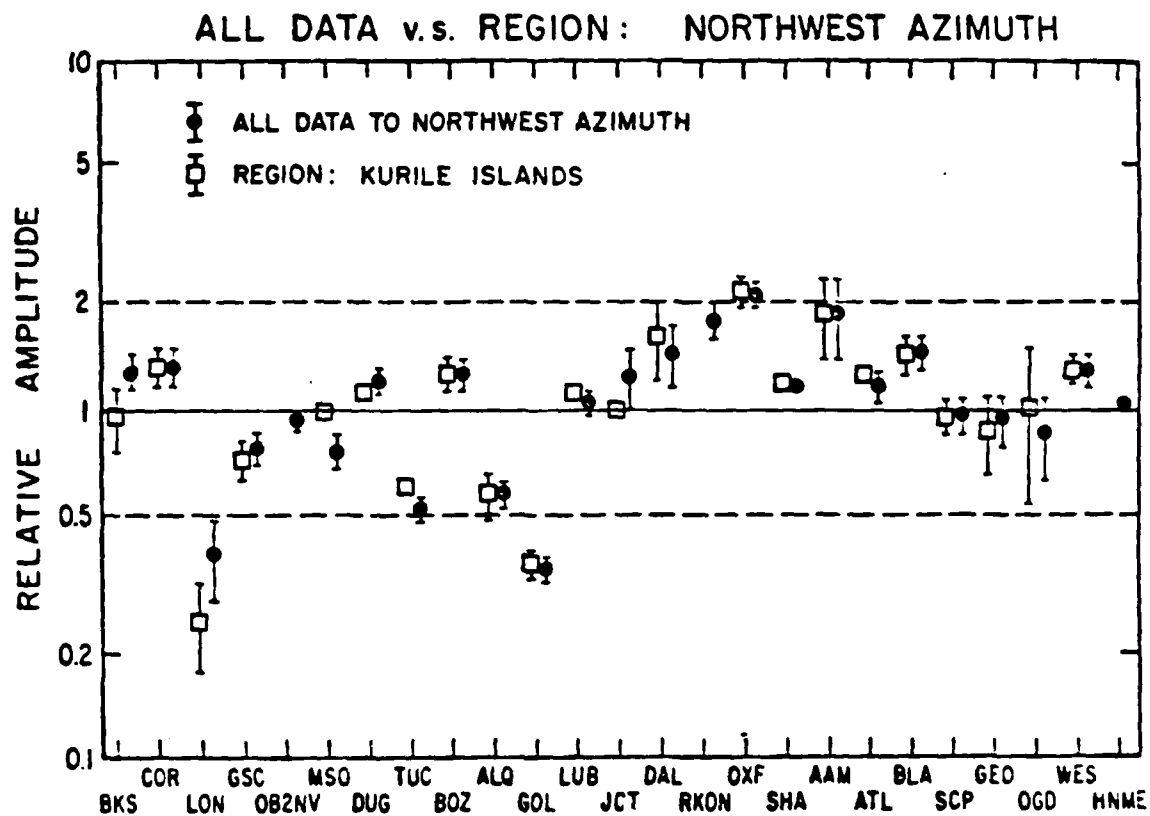


Figure A1. Mean relative amplitudes from earthquakes in the Kurile Islands are compared with all data to a northwest azimuth from the United States.

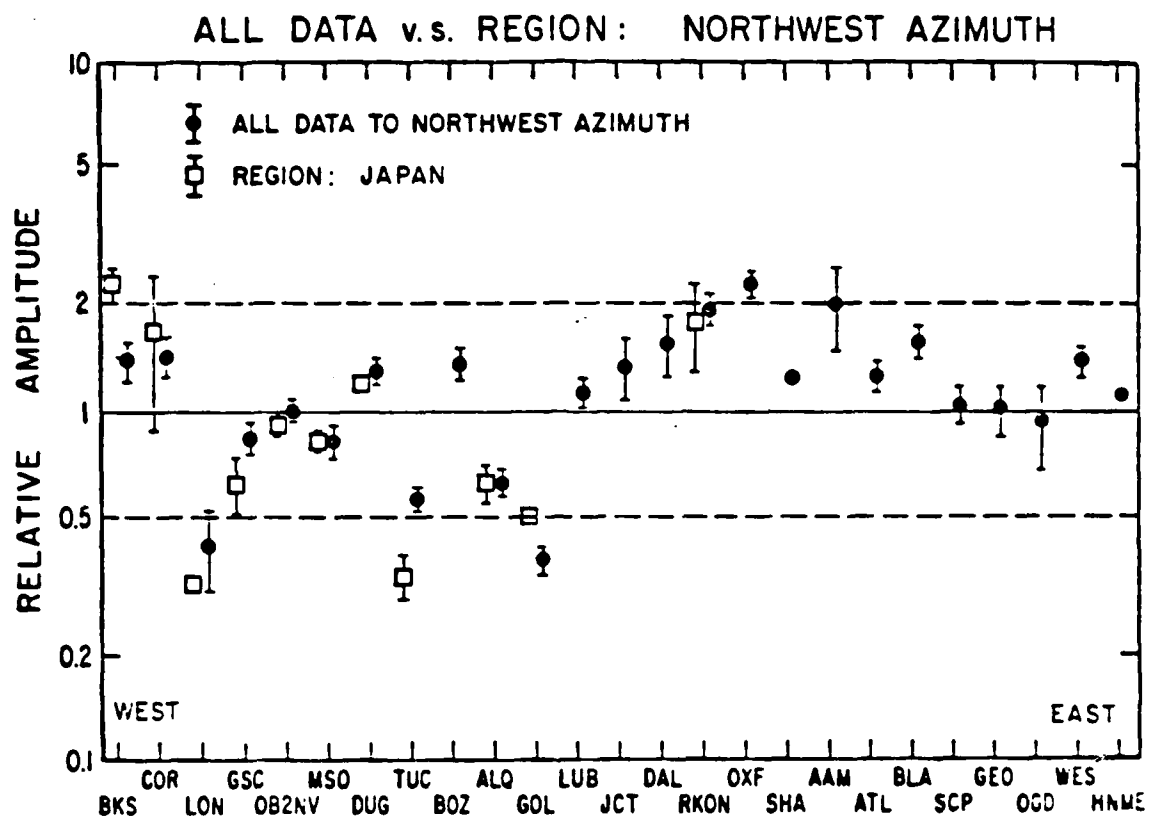


Figure A2. Mean relative amplitudes from earthquakes in Japan are compared with all data to a northwest azimuth from the United States.

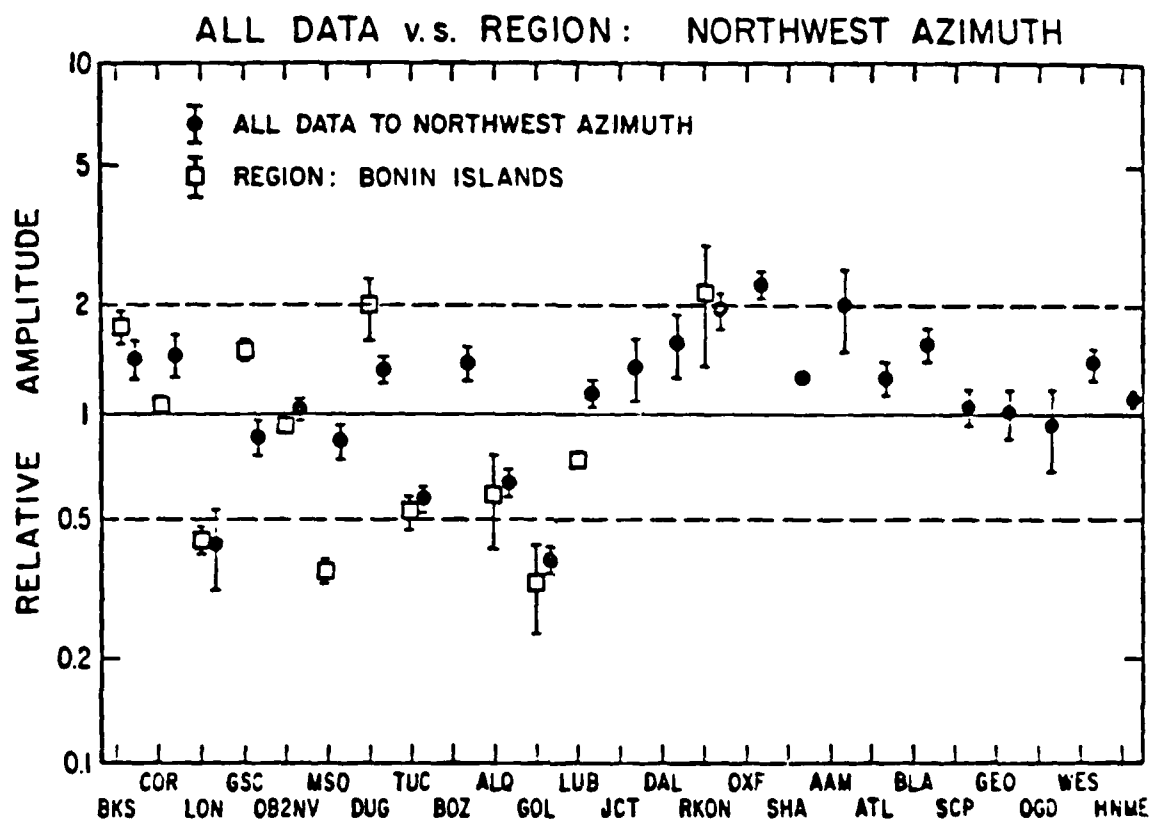


Figure A3. Mean relative amplitudes from earthquakes in the Bonin Islands are compared with all data to a northwest azimuth from the United States.

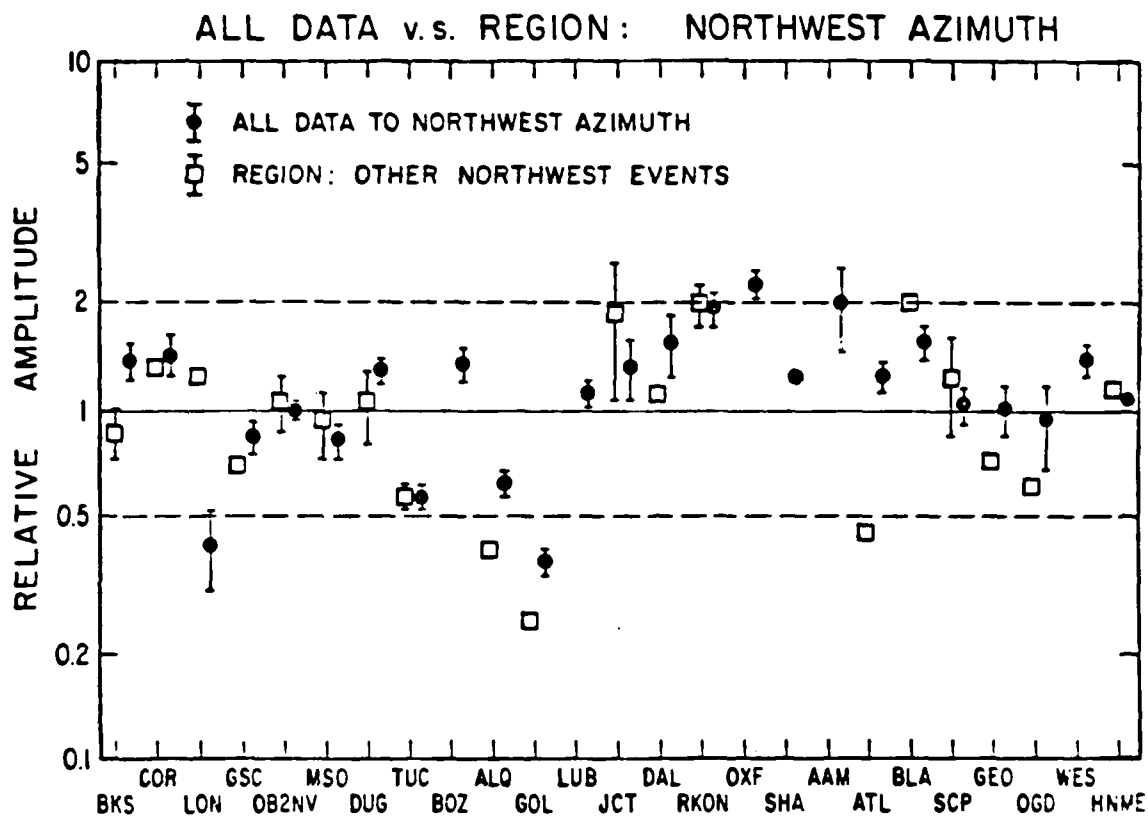


Figure A4. Mean relative amplitudes from other northwest earthquakes not located in the Kuriles, Japan, or Bonin Islands are compared with all data to a northwest azimuth from the United States.

Table A22

Estimated Sediment Amplification Corrections
for WWSSN and SDCS Stations

Station	Amplitude Correction*	Station	Amplitude Correction*
AAM	1.4	JCT	**
ALQ	**	LON	**
ATL	**	LUB	1.9
BEC	1.8	MDS	**
BKS	1.3	MSO	**
BLA	**	OB2NV	**
BOZ	**	OGD	**
COR	**	OXF	1.9
DAL	1.6	RCD	1.6
DUG	**	RKON	**
FLO	1.5	SCP	**
GEO	**	SHA	1.8
GOL	**	TUC	**
GSC	**	WES	**
HNME	**		

*Station amplitude to be divided by correction.

**No sediment correction necessary; in the case of a limestone site of unknown hardness, no correction assumed.

Table A23

Estimated Sediment Amplification Corrections
for Cleary (1967) LRSM Stations

Station	Log Amplitude Correction ^a	Station	Log Amplitude Correction ^a
ARWS	**	KGAZ	**
ATNV	**	KNUT	(-0.20)
AYSD	(-0.26)	LCNM	**
BDPA	(-0.11)	MMTN	(-0.15)
BFCL	**	MNNV	**
BLWV	(-0.15)	MPAR	(-0.11)
BUQB	**	MVCL	**
CKCB	(-0.15)	MZAR	(-0.11)
CPCL	**	NDCL	**
CTOK	(-0.26)	NGWS	**
CVTN	(-0.15)	NPNT	(-0.26)
DENY	(-0.11)	PFMI	**
DRCO	**	PMWY	**
EYNV	(-0.15)	PTOR	**
FMUT	**	RKON	**
FRMA	(-0.26)	RTNM	(-0.20)
FSAZ	**	RYND	(-0.26)
GDVA	(-0.15)	SEMN	**
GIMA	(-0.26)	SJTX	(-0.26)
GONB	(-0.26)	SSTX	**
GVTX	(-0.20)	STNV	(-0.04)
HBOK	(-0.15)	TFCL	(-0.20)
HHND	(-0.26)	TKWA	**
HKWY	(-0.26)	TUPA	(-0.11)
HLID	**	WINV	(-0.18)
HMBC	**	WNSD	(-0.26)
HNME	**	WTTN	(-0.15)
HTMN	**	WWUT	**

^aLog amplitude correction to be added to station log amplitude.

^bNo sediment correction necessary; in the case of a limestone site of unknown hardness, no correction assumed.

Table A24

Inferred Q_a for LRSM Stations from Evernden and Clark (1970)
Which Were Not Covered in Cleary (1967)

Station	Log Amplitude [*]	Estimated Sediment Correction	Bedrock Log Amplitude	Q_a (Inferred)
AZTX	(-0.06)	(-0.15)	(-0.21)	89
BRPA	(0.09)	(-0.11)	(-0.02)	133
BXUT	(-0.15)	(-0.20)	(-0.35)	72
CUNV	(-0.21)	**	(-0.22)	87
DUOK	(-0.32)	(-0.20)	(-0.52)	58
EBMT	(0.15)	**	(0.15)	243
EKNV	(-0.13)	(-0.15)	(-0.28)	79
LSNH	(0.032)	**	(0.032)	154
SKTX	(0.033)	(-0.15)	(-0.057)	119

*Includes (-0.02) correction from least-squares fit to common data in Cleary (1967) plus (+0.01) correction to WISSN-SDCS baseline

**No sediment correction necessary; in the case of a limestone site of unknown hardness, no correction assumed.

Table A25

Inferred Q_s for LRSM Stations from Booth et al. (1974)
Which Were Not Covered in Cleary (1967)

Station	Log Amplitude*	Estimated Sediment Correction	Bedrock Log Amplitude	Q_s (Inferred)
AXAL	(0.10)	(-0.26)	(-0.16)	97
BEFL	(0.33)	**	(0.33)	2500
BRPA	(0.02)	(-0.11)	(-0.09)	112
FKCO	(0.19)	(-0.26)	(-0.07)	117
HYMA	(-0.32)	(-0.26)	(-0.58)	55
JELA	(0.28)	(-0.26)	(0.02)	148
JRAZ	(-0.16)	**	(-0.16)	97
KCMO	(0.12)	**	(0.12)	212
LVLA	(0.19)	(-0.26)	(-0.07)	117
MOID	(0.41)	(-0.20)	(0.21)	337
SWMA	(0.04)	(-0.15)	(-0.11)	107

*Includes (-0.01) correction from least-squares fit to common data in Cleary (1967) plus (+0.01) correction to WSSN-SDCS baseline, therefore no correction.

**No sediment correction necessary; in the case of a limestone site of unknown hardness, no correction assumed.

Table A1
Northern Novaya Zemlya Explosions

P Wave Amplitude

Nanometers

STATION	10/27/66	10/21/67	11/07/68	10/14/69	10/14/70
(west)					
BKS	506	110	176	275	2113
COR	374	132	220	264	
LON			165	247	
GSC		57	159		
MSO					
DUG	385	66	118	166	1100
TUC		134	195	235	
BOZ					
ALQ	187	57	82	121	721
GOL	228	57	79	128	
RCD	1145				
LUB		209	242	418	
JCT		166	233		
DAL			638		
FLO					2267
OXF	990	203	308	451	2873
SHA	1321	308	396	616	3699
AAM	1453	330	418	506	2654
ATL	682	137			2058
BLA		269	412		
SCP		192	308	440	
GEO		132	286	419	2267
OGD		159	214	291	
WES		132	192	275	1541
BEC	308		110		
(east)					

Table A1
Northern Novaya Zemlya Explosions (continued)

P Wave Amplitude

Nanometers

STATION	9/27/71	8/28/72	9/12/73	8/29/74	8/23/75	10/21/75
(west)						
BKS	803		2752	616	605	990
COR		418		572	528	890
LON		412		638	682	781
GSC				605		
MSO					561	737
DUG				379	338	
TUC	726	407				
BOZ						
ALQ		203		242	291	
GOL						
RCD		990				
LUB			2763			
JCT						
DAL	2466	1365				
FLO						
OXF	1425		3313	1001	1012	1420
SHA		836	5064	1189	1497	1717
AAM	2069	1100				
ATL	946	550				
BLA						
SCP						
GEO					770	1348
OGD	913			693	605	748
WES	990	572				
BEC	517	319		385	319	
(east)						

Table A2
Southern Novaya Zemlya Explosions

P Wave Amplitude

Nanometers

STATION	10/27/73	11/02/74	10/19/75
(west)			
BKS	220	2730	968
COR	176		1078
LON	267		
GSC	203		
MSO			
DUG	119		
TUC	121		
BOZ			
ALQ	81		
GOL	44	481	
ROD			
LUB	242		
JCT			754
DAL			
FLO			
OXF	258	3071	1315
SHA		3434	1233
AAM	242	4051	
ATL		1387	
BLA	123	2036	
SCP	214		
GEO			
OGD	88		561
WES		759	
BEC			
(east)			

Table A3
Semipalitinsk East Explosions
P Wave Amplitude
Nanometers

STATION	1/15/65	11/30/69	11/02/72	7/23/73	12/14/73
(west)					
BKS	86	55	126	142	55
COR		142		276	315
LON		71		146	63
GSC	52		80		
MSO					39
DUG					
TUC	11	7	15	17	4½
BOZ	86				
ALQ	19	15		38	10
GOL	55	42	80		31
RCD	86				
LUB		31	63	63	
JCT		4	6	10	
DAL	78			118	
FLO	35	31			
OXF		39	102	150	
SHA					
AAM	118	63	165	244	110
ATL	31	23	59		
BLA	23	19	55	74	
SCP		55		102	
GEO	71	67			
OGD			98	130	39
WES			43	55	
BEC				63	
(east)					

Table 3
Semipalitinsk East Explosions (continued)

P Wave Amplitude

Nanometers

STATION	5/31/74	7/04/76
(west)		
BKS		39
COR	78	86
LON	52	55
GSC	26	23
MSO	22	
DUG		100
TUC		5
BOZ		
ALQ		11
GOL	34	
RCD		
LUB		
JCT	7	
DAL		
FLO		
OXF		
SHA		
AAM	47	
ATL	23	
BLA	17	19
SCP		
GEO	47	67
OGD	39	27
WES	23	15
BEC		
(east)		

Table A4
Additional Semipalitinsk East Explosions

P Wave Amplitude

Nanometers

STATION	11/23/76	12/07/76	5/29/77
(west)			
BKS	61	55	
COR	178	111	132
LON			
GSC	38	38	33
OB2NV			63
MSO	50	44	35
DUG		147	123
TUC	8		7
BOZ			
ALQ	13	16	15
GOL	44	45	
LUB			
JCT			
DAL			
RKON	281	326	273
OXF			
SHA			
AAM			
ATL	33		33
BLA	44	41	22
SCP	77	50	50
GEO			110
OGD	44	50	49
WES			
HNME	132		112
(east)			

Table A5
Semipalitinsk West Explosions
P Wave Amplitude
Nanometers

STATION	10/19/66	4/20/67	10/17/67	9/29/69	6/23/70
(west)					
BKS	31	27	15	39	47
COR	78			110	86
LON	53	31	37	65	51
CSC	14	14	5		
MSO					
DUG			83		
TUC	3½		1	4	6
BOZ		39	42		
ALQ	8	6	7	13	13
GOL	22	16	15	37	34
RCD	31				
LUB	15	11			
JCT	4½		3		3½
DAL				31	
FLO					
OXF	29		17	35	
SHA					
AAM	31	23		39	47
ATL	13		4	21	21
BLA				20	
SCP	11	11	6	19	27
GEO					
OCD				11	
WES					
REC					
(east)					

Table A5

Semipalitinsk West Explosions (continued)

P Wave Amplitude

Nanometers

STATION	3/22/71	4/25/71	12/30/71	2/20/75
(west)				
BKS	31	63	43	
COR			110	
LON	43	78	65	
GSC				17
MSO				23
DUG				
TUC	3½	8		3½
BOZ				
ALQ	8			8
GOL	24	53	27	25
RCD				
LUB	15	39		18
JCT	5	13	4	3
DAL		55	31	
FLO		35		
OXF	31		35	21
SHA				
AAM	39	47	31	51
ATL		27	15	
BLA		19	13	8
SCP	19	43		
GLO				
OGD				
WES				
BEC				11
(east)				

Table A6
Western Kazakh Explosions
P Wave Amplitude
Nanometers

STATION	12/06/69	12/12/70	12/23/70
(west)			
BKS	17	28	21
COR	63	70	71
LON	35	60	55
GSC	3½		
MSO			
DUG	19	30	25
TUC	1½	5	6
BOZ			
ALQ	10	17	15
GOL	21	32	39
RCD			
LUB		33	25
JCT		7	11
DAL		40	
FLO	33		
OXF	83	150	123
SHA			
AAM	77	78	78
ATL	24	35	39
BLA	30	36	78
SCP	110	175	213
GEO	70	150	157
OGD	22	60	88
WES		48	
BEC			58
(east)			

Table A7
Kurile Earthquakes
P Wave Amplitudes
Corrected for Geometric Spreading to $\Delta = 60^\circ$
Nanometers

STATION	11/22/65	3/20/67	8/10/67	2/10/68	4/28/68
(west)					
BKS		112	101	100	
COR	453			253	
LON	161		24		
GSC	417		68	67	
OB2NV					
MSO					
DUG	513	79	125	148	
TUC	340	36	59	71	
BOZ	508	64	143	238	
ALQ	298	25	65	52	
GOL	202	18	46	53	15
LUB	450			120	45
JCT	440	60			
DAL	744				95
RKON					
OXF	973	161	184	319	
SHA	496				
AAM	475		197	305	38
ATL	462	76	154	182	58
BLA	407	83	174	262	65
SCP	351	44	111	138	57
GEO	271				
OGD	222				
WES	435	104	181	191	
HNME					
(east)					

Table A7

Kurile Earthquakes (continued)

P Wave Amplitude

Corrected for Geometric Spreading to $\Delta = 60^\circ$

Nanometers

STATION	7/25/68	10/26/76	3/19/77
(west)			
BKS	139		912
COR	242		1388
LON			195
GSC		710	924
OB2NV			
MSO		842	1278
DUG	185	1178	1187
TUC	122	505	724
BOZ			
ALQ	149		
GOL		233	
LUB	251		1545
JCT			
DAL			1048
RKON			
OXF			
SHA			
AAM			4634
ATL		765	2174
BLA	146		2715
SCP			
GEO			1404
OGD	273		
WES	182		
HNME			
(east)			

Table A8
Japanese Earthquakes
P Wave Amplitude
Corrected for Geometric Spreading to $\Delta = 60^\circ$
Nanometers

STATION	12/31/76	1/01/77	2/18/77	6/12/77
(west)				
BKS		196	734	
COR		186	323	
LON			118	
GSC	7	56	325	19
OB2NV	16			39
MSO	18	53	310	30
DUG	19	93	483	51
TUC	8	18		15
BOZ				
ALQ	12	37		30
GOL	9			
LUB				
JCT				
DAL				
RKON	44			50
OXF				
SHA				
AAM				
ATL				
BLA				
SCP				
GEO				
OGD				
WES				
HNME				
(east)				

Table A9

Bonin Islands Earthquakes

P Wave Amplitude

Corrected for Geometric Spreading to $\Delta = 60^\circ$

Nanometers

STATION	9/22/76	12/05/76	12/22/76	1/05/77
(west)				
BKS	212	99	339	
COR	106			
LON	48			37
GSC	148	79		157
OB2NV			210	
MSO	33		87	
DUG	277	115		124
TUC	51	22	132	60
BOZ				
ALQ	26	50	149	
GOL	52	12	62	
LUB			170	
JCT				
DAL				
RKON		179	315	
OXF				
SEA				
AAM				
ATL				
BLA				
SCP				
GEO				
OGD				
WES				
HNME				
(east)				

Table A10

Other Earthquakes to a Northwest Azimuth from the United States

P Wave Amplitude

Corrected for Geometric Spreading to $\Delta = 80^\circ$

Nanometers

STATION	10/22/76	4/22/77	4/23/77	7/20/77	8/07/77
(west)					
BKS	44	53			85
COR					112
Lon			21		
GSC				44	
OB2NV		52	26	68	54
MSO		65	14	26	105
DUG	45	70	21		
TUC	55	22	7	44	47
BOZ					
ALQ	31				
GOL	20	13			
LUB					
JCT		56	45		
DAL					97
RKON			30	146	
OXF					
SEA					
AAM					
ATL	35				
RLA				130	
SCP			14	105	
GEO	55				
OGD	49			37	
WES					
EXME				74	
(east)					

Table A11

South American Earthquakes

P Wave Amplitude

Corrected for Geometric Spreading to $\Delta = 60^\circ$

Nanometers

STATION	4/25/67	11/15/67	2/06/68	4/21/68	4/30/68
(west)					
BKS	106	314	143		
COR		678	277		
LON	24	176	73		
GSC		255	113		142
OB2NV					
MSO					
DUG	69		233		146
TUC	50	166	75	53	96
BOZ		147			
ALQ	106	216	84	56	143
GCL	69	203	78		140
LUB	255		339	115	
JCT	238				
DAL	211				
RKON					
OXF	456	583	151		402
SEA					
AAM		401			142
ATL	227		56	53	367
BLA			47		
SCP	77	323	73	63	187
GFO	100	312			
OGD			61		270
WES			74		169
HNME					
(east)					

Table A11
 South American Earthquakes (continued)
 P Wave Amplitude
 Corrected for Geometric Spreading to $\Delta = 60^\circ$
 Nanometers

STATION	9/30/76	12/03/76	12/04/76	3/08/77	3/13/77
(west)					
BKS	120	86	107		
COR	214	186	143		
LON	59				
GSC	185	95	126	29	59
OB2NV					
MSO	100	49	75	62	
DUG	150	48	121	55	53
TUC	127	61	70		20
BOZ					
ALQ		54	42		
GOL		41	48		
LUB					103
JCT				27	
DAL					257
RKON			96		
OXF					
SHA					
AAM					
ATL	58	37		65	54
BLA		60		76	
SCP					
GEO				96	
OGD				34	19
WES					37
HNME					
(east)					

Table A11
 South American Earthquakes (continued)
 P Wave Amplitude
 Corrected for Geometric Spreading to $\Delta = 60^\circ$
 Nanometers

STATION	4/15/77	6/02/77	6/05/77	6/08/77	6/18/77
(west)					
BKS	177		82	151	203
COR			119	177	
LON	32	11	26		363
GSC		28	66	161	215
OB2NV	131	56	74	156	
MSO	93	13	99	116	
DUG		33	88	176	225
TUC	116	17	63	149	130
BOZ					
ALQ					
GOL					
LUB					
JCT					
DAL			67		
RKON	221	60	171		
OXF					
SHA					
AAM					
ATL	72		75	96	
BLA	83		89	264	
SCP					
CEO	72		69	77	
OGD			40	34	
WES					
ENME	125		85		
(east)					

Table A12
Northern Novaya Zemlya

STATION	MEAN	S.E.M.	N
(west)			
BKS	0.89	0.04	10
COR	0.82	0.04	8
LON	0.82	0.04	6
GSC	0.65	0.13	3
MSO	0.77	0.03	2
DUG	0.53	0.02	7
TUC	0.81	0.04	5
BOZ			
ALQ	0.37	0.01	8
GOL	0.38	0.01	4
RCD	1.84	0.00	2
LUB	1.23	0.10	4
JCT	1.10	0.06	2
DAL	2.63	0.11	3
FLO	1.18		1
ONF	1.43	0.03	10
SHA	1.89	0.07	10
AAN	1.95	0.13	7
ATL	1.02	0.03	5
BLA	1.86	0.02	2
SCP	1.37	0.01	3
GEO	1.19	0.07	6
OGD	0.92	0.04	7
WES	0.92	0.04	6
BEC	0.51	0.02	6
(east)			

Table A13

Southern Novaya Zemlya

STATION	MEAN	S.E.M.	N
(west)			
BKS	1.39	0.08	3
COR	1.31	0.09	2
LON	1.94		1
GSC	1.41		1
MSO			
DUG	0.83		1
TUC	0.94		1
BOZ			
ALQ	0.56		1
GOL	0.27	0.03	2
RCD			
LUB	1.67		1
JCT	0.98		1
DAL			
FLO			
OXF	1.67	0.07	3
SEA	1.66	0.06	2
AAM	1.95	0.19	2
ATL	0.69		1
BLA	0.94	0.09	2
SCP	1.48		1
GEO			
OGD	0.67	0.06	2
WES	0.33		1
BEC			
(east)			

Table A14
Semipalatinsk East

STATION	MEAN	S.E.M.	N
(west)			
BKS	1.52	0.05	6
COR	4.18	1.09	5
LON	1.75	0.07	5
GSC	0.93	0.05	4
MSO	0.91	0.15	2
DUG	3.51		1
TUC	0.19	0.01	6
BOZ	1.72		1
ALQ	0.39	0.02	5
GOL	1.04	0.06	5
RCD	1.72		1
LUB	0.76	0.05	3
JCT	0.13	0.04	4
DAL	1.40	0.16	2
FLO	0.77	0.07	2
ONF	1.30	0.15	3
SHA			
AAM	2.20	0.22	6
ATL	0.69	0.04	4
BLA	0.62	0.05	6
SCP	1.27	0.20	2
GEO	1.78	0.20	4
OGD	1.19	0.08	5
WES	0.61	0.03	4
BEC	0.66		1
(east)			

Table A15

Semipalatinsk East Including Additional Events

STATION	MEAN	S.E.M.	N
(west)			
BKS	1.26	0.05	8
COR	3.26	0.58	8
LON	1.52	0.06	5
GSC	0.77	0.03	7
OB2NV	1.34		1
MSO	0.82	0.05	5
DUG	2.83	0.12	3
TUC	0.15	0.01	8
BOZ	1.47		1
ALQ	0.32	0.02	8
GOL	0.89	0.04	7
LUB	0.67	0.05	3
JCT	0.12	0.03	4
DAL	1.21	0.13	2
RKON	5.75	0.37	3
OXF	1.14	0.13	3
SHA			
AAM	1.90	0.18	6
ATL	0.62	0.03	6
BLA	0.59	0.05	9
SCP	1.16	0.09	5
GEO	1.69	0.21	5
OGD	0.99	0.05	8
WES	0.53	0.05	4
HNME	2.38	0.02	2
(east)			

Table A16

Semipalitinsk West

STATION	MEAN	S.E.M.	N
(west)			
BKS	1.55	0.06	8
COR	3.74	0.25	4
LON	2.33	0.22	8
GSC	0.76	0.10	4
MSO	1.15		1
DUG	8.29		1
TUC	0.16	0.01	7
BOZ	3.39	0.92	2
ALQ	0.47	0.04	7
GOL	1.20	0.05	9
RCD	1.51		1
LUB	0.91	0.04	5
JCT	0.22	0.03	7
DAL	1.19	0.05	3
FLO	0.90		1
ONF	1.39	0.10	6
SHA			
AAM	1.58	0.16	8
ATL	0.63	0.05	6
BLA	0.52	0.07	4
SCP	0.79	0.07	7
GEO			
OGD	0.40		1
WES			
BEC	0.57		1
(east)			

Table A17

Western Kazakh

STATION	MEAN	S.E.M.	N
(west)			
BKS	0.65	0.07	3
COR	2.05	0.34	3
LON	1.44	0.06	3
GSC	0.15		1
MSO			
DUG	0.73	0.07	3
TUC	0.11	0.02	3
BOZ			
ALQ	0.41	0.02	3
GOL	0.88	0.05	3
RCD			
LUB	0.71	0.11	2
JCT	0.22	0.04	2
DAL	0.99		1
FLO	1.44		1
OXF	3.42	0.24	3
SHA			
AAM	2.38	0.47	3
ATL	0.95	0.05	3
BLA	1.62	0.16	3
SCP	4.72	0.23	3
GEO	3.50	0.23	3
OGD	1.52	0.33	3
WES	1.18		1
BEC	1.40		1
(east)			

Table A18

Kurile Islands

STATION	MEAN	SEM	N
(west)			
BKS	0.97	0.20	5
COR	1.34	0.17	4
LON	0.25	0.07	3
GSC	0.73	0.10	5
OB2NV			
MSO	1.00	0.01	2
DUG	1.14	0.05	7
TUC	0.61	0.04	7
BOZ	1.30	0.14	4
ALQ	0.58	0.09	5
GOL	0.37	0.03	6
LUB	1.13	0.09	5
JCT	1.01	0.07	2
DAL	1.64	0.43	3
RKON			
OXF	2.20	0.21	4
SHA	1.21		1
AAM	1.92	0.49	5
ATL	1.28	0.10	7
BLA	1.46	0.18	7
SCP	0.97	0.11	5
GEO	0.89	0.22	2
OGD	1.04	0.49	2
WES	1.33	0.13	5
ENME			
(east)			

Table A19

Japan

STATION	MEAN	S.E.M.	N
(west)			
BKS	2.74	0.33	2
COR	1.99	0.93	2
LON	0.39		1
GSC	0.74	0.14	4
OB2NV	1.11	0.09	2
MSO	0.99	0.07	4
DUG	1.45	0.08	4
TUC	0.41	0.06	3
BOZ			
ALQ	0.75	0.10	3
GOL	0.61		1
LUB			
JCT			
DAL			
RKON	2.16	0.62	2
OXF			
SHA			
AAM			
ATL			
BLA			
SCP			
GEO			
OGD			
WES			
HNME			
(east)			

Table A20

Bonin Islands

STATION	MEAN	S.E.M.	N
(west)			
BKS	2.07	0.21	3
COR	1.24		1
LON	0.51	0.05	2
GSC	1.77	0.11	3
OB2NV	1.09		1
MSO	0.42	0.03	2
DUG	2.37	0.48	3
TUC	0.62	0.07	4
BOZ			
ALQ	0.70	0.20	3
GOL	0.39	0.11	3
LUB	0.88		1
JCT			
DAL			
RKON	2.63	0.99	2
OXF			
SHA			
AAM			
ATL			
BLA			
SCP			
GEO			
OGD			
WES			
HNME			
(east)			

Table A21

Other Northwest Data

STATION	MEAN	S.E.M.	N
(west)			
BKS	0.95	0.16	3
COR	1.44		1
LON	1.39		1
GSC	0.77		1
OB2NV	1.18	0.21	4
MSO	1.04	0.22	4
DUG	1.17	0.27	3
TUC	0.62	0.07	5
BOZ			
ALQ	0.44		1
GOL	0.28	0.00	2
LUB			
JCT	2.07	0.87	2
DAL	1.24		1
RKON	2.23	0.28	2
OXF			
SHA			
AAM			
ATL	0.50		1
BLA	2.25		1
SCP	1.38	0.44	2
GEO	0.80		1
OGD	0.68	0.03	2
WES			
HNME	1.28		1
(east)			